Alma Mater Studiorum · Università di Bologna

Scuola di Scienze
Corso di Laurea Magistrale in Fisica

Fabrication of High-k Dielectric Thin Films for Spintronics

Relatore:
Prof.ssa Beatrice Fraboni

Correlatore:
Dott. Patrizio Graziosi

Presentata da:
Fabio Galassi

Sessione III
Anno Accademico 2014/2015

Contents

Introduction

The aim of this thesis is the fabrication of complex oxides thin films with the perovskite structure and general formula ABO_3, using the *Channel Spark Ablation* tecnique (CSA), which is a kind of pulsed electron deposition method. Such a method is based on the ablation of a stoichiometric target by means of pulsed electron beams ($\sim 100\,\mathrm{ns}$) with high energy density ($\sim 10\,\mathrm{J/cm^2}$) and it is suitable to produce high quality stoichiometric films of simple oxides, complex oxides and manganites.
Because of the broad diversity of properties that its compounds exhibit, the perovskite structure has a prominent role in many research field and technological sectors, and spintronics is no exception. One of the most important aspects is the possibility to epitaxially grow multilayer devices, where each layer performs a different function.
The main object of the present work consists in the growth of high-κ dielectric thin films, such as $SrTiO_3$ (STO) and $NdGaO_3$ (NGO). Strontium titanate is very attractive for spintronics and, more generally, for electronic applications, owing to its insulating and dielectric properties. In particular STO is used as tunnel barrier in spin valve devices, it is a promising candidate as gate insulator in MOSFET and as dielectric layer in memory capacitors. The main contribution to the dielectric constant of titanates arising from the displacement of the Ti ions into TiO_6 octahedra, in response to an applied electric field. Than, since the polarization is related to ionic dipoles, these materials are suitable for applications in the microwave frequency range and the infrared range ($\sim 10^{12}\,\mathrm{Hz}$) can be considered as an upper limit for the operative frequency of this class of dielectrics.
Another material of great interest in spintronics, which also has the perowskite structure, is the ferromagnetic manganite $La_{0.7}Sr_{0.3}MnO_3$ (LSMO). Owing to its *half-metallicity*, i.e. its electronic band structure at the Fermi level is completely spin-polarized, LSMO is used as electrode in tunnel magnetoresistance-based devices, such as LSMO/STO/Co magnetic tunnel junctions.
The first of four chapters forming this thesis consists of an overview on the main concepts and most recent developments concerning spintronics.
In the second chapter we discuss the structural an dielectric properties of the perovskite oxides, with particular attention to titanates. Also, we describe the (La,Sr)MnO_3 manganites, their electronic structure and the main properties that follows, such as the half-metallicity and the colossal magnetoresistance.

In the third chapter the experimental tecniques are discussed. The channel spark ablation method, which is used do fabricate all the devices of this work, is carefully described. Finally, the fourth chapter is devoted to describe the deposition procedure and parameters for the device fabrication and to the experimental results and their analysis. This chapter is composed of three main sections. The first of them describes the work on LSMO/STO/Co junctions, which are memristors with ferromagnetic electrodes and, in a few words, they combines electric and magnetic memory. In particular, the LSMO deposition procedure and characterization and the STO on LSMO growth parameters are reported. Moreover, the device characterization is summarized.
The other two sections of the fourth chapter deals with the fabrication and characterization of high-κ dielectric thin films whith the perovskite structure: STO and NGO. Several sets of capacitors in the Metal/Insulator/Semiconductor configuration were built, in order to investigate the dependence of the dielectric and insulating properties on the growth parameters. To be precise we focused on the growth temperature and, in the case of the STO films, also on the thickness dependence of the dielectric constant. As expected, the dielectric constant of STO ($\epsilon_r = 65$ for 40 nm-thick film and $\epsilon_r = 175$ for 170 nm-thick film) appars larger than that of the NGO films we deposited (we achieved $\epsilon_r \sim 20$, as the bulk value). In spite of the high capacitance density achievable by STO capacitor, the dielectric constant of this material results strongly dependent on the film thickness. Another critical aspects concerning STO is represented by the oxidation level of the film: oxygen vacancies can reduce the STO high nominal resistivity and increase its leakage current. By contrast NGO is less sensitive to technological processes and, at the same time, it has higher dielectric constant value than typical dielectric as silicon oxide.

Introduzione

Lo scopo di questa tesi è la fabbricazione di ossidi complessi aventi struttura perovskitica e formula generale ABO_3, per mezzo della tecnica *Channel Spark Ablation* (CSA), un metodo appartenente alla famiglia *pulsed electron deposition*. Tale metodo è basato sulla ablazione di un target stechiometrico da parte di un fascio pulsato di elettroni ($\sim 100\,\mathrm{ns}$) ad alta densità di energia ($\sim 10\,\mathrm{J/cm^2}$) ed è indicato per la produzione di film stechiometrici di alta qualità di ossidi semplici, ossidi composti e manganiti.
Per via della grande varietà nelle proprietà dei suoi composti, la struttura a perovskite svolge un ruolo preminente in molti campi di ricerca ed in molti settori tecnologici e quello della spintronica non fa eccezione. Uno degli aspetti di maggior importanza consiste nella possibilità di crescere in modo epitassiale dispositivi multilayer, in cui ciascun layer svolge una funzione differente.
L'oggetto principale di questo lavoro consiste nella crescita di film sottili di materiali con alta costante dielettrica, quali $SrTiO_3$ (STO) e $NdGaO_3$ (NGO). Il titanato di stronzio è molto importante in spintronica e, più in generale, per applicazioni di elettronica, per via delle sue proprietà isolanti e dielettriche. In particolare l'STO è impiegato come barriera tunnel in dispositivi di tipo spin valve, è un candidato promettente come isolante di gate nei dispositivi MOSFET e come dielettrico in condensatori per memorie. Il contributo principale alla costante dielettrica dei titanati è dovuta allo spostamento degli ioni Ti all'interno degli ottaedri TiO_6, in seguito all'applicazione di un campo elettrico esterno. Dal momento che la polarizzazione è legata a momenti di dipolo ionici, questi materiali possono essere sfruttati in applicazioni nel range di frequenza delle microonde ed il range infrarosso ($\sim 10^{12}\,\mathrm{Hz}$) può essere considerato il limite superiore per la frequenza di lavoro di questa classe di dielettrici.
Un altro materiale di grande interesse in spintronica, anch'esso dotato di struttura perovskitica, è la manganite $La_{0.7}Sr_{0.3}MnO_3$ (LSMO). Grazie alle sue proprietà di *half-metallicity*, i.e. la sua struttura elettronica a bande risulta completamente spin-polarizzata al livello di Fermi, LSMO è impiegata come elettrodo in dispositivi basati sulla magnetoresistenza tunnel, come ad esempio le giunzioni tunnel magnetiche LSMO/STO/Co.
Il primo dei quattro capitoli che compongono questa tesi consiste in una panoramica dei concetti principali e dei recenti sviluppi inerenti la spintronica.
Nel secondo capitolo vengono discusse le proprietà strutturali e dielettriche degli ossidi

di perovskite, riservando un'attenzione particolare ai titanati. Inoltre sono descritte la manganiti (La,Sr)MnO_3, la loro struttura elettronica e le principali proprietà che ne conseguono, come la half-metallicity e la magnetoresistenza colossale.
Nel terzo capitolo vengono discusse le tecniche sperimentali usate. Il metodo della channel spark ablation, usato per produrre tutti i dispositivi del presente lavoro, viene descritto in dettaglio.
Infine, il quarto capitolo è dedicato alla descrizione delle procedure e dei parametri di deposizione per la fabbricazione dei dispositivi, e all'esposizione dei risultati sperimentali e relativa analisi. Questo capitolo è formato da tre sezioni principali. La prima di esse descrive il lavoro relativo alle giunzioni LSMO/STO/Co. Questi dispositivi sono dei memristor con elettrodi ferromagnetici e, in breve, combinano memoria elettrica e magnetica. In particolare vengono riportati la procedura di deposizione e la caratterizzazione dell'LSMO, nonché i parametri di crescita dell'STO sull'LSMO. Inoltre viene riportata brevemente la caratterizzazione del dispositivo.
Le altre due sezioni del capitolo quarto trattano la fabbricazione e caratterizzazione di film sottili con alta costante dieletrica aventi la struttura della perovskite: STO e NGO. Sono stati costruiti diversi set di condensatori nella configurazione Metallo/Isolante/-Semiconduttore (MIS), allo scopo di indagare la dipendenza delle proprietà dielettriche ed isolanti dai parametri di crescita. In particolare ci si è concentrati sulla temperatura di deposizione e, nel caso dei film di STO, anche sulla dipendenza della costante dielettrica dallo spessore del film. Come ci si aspettava, la costante dielettrica dei film di STO ($\epsilon_r = 65$ per un film spesso 40 nm ed $\epsilon_r = 175$ per uno spessore di 170 nm) si è rivelata maggiore di quella dei film di NGO depositati (abbiamo ottenuto $\epsilon \sim 20$, che coincide con il valore di bulk). Nonostante l'elevata capacità per unità di area ottenibile con l'STO, la costante dielettrica di questo materiale risulta fortemente dipendente dallo spessore del film. Un ulteriore aspetto critico relativo all'STO è dato dal livello di ossidazione del film: le vacanze di ossigeno, infatti, possono ridurre la resistività dell'STO (nominalmente molto elevata), ed aumentarne la corrente di perdita. Al contrario l'NGO è meno sensibile ai processi tecnologici e, allo stesso tempo, ha un valore di costante dielettrica più alto rispetto ad un tipico dielettrico come l'ossido di silicio.

Chapter 1

A Brief Introduction to Spintronics

The term *spintronics* (spin transport electronics, or spin-based electronics [1]) is used to indicate a field of research and a technology, in which the information is carried not only by the electron charge, but also by the electron spin. The function of a spintronic device is the manipulation of some quantity related to electrons, typically an electrical current, in a way that dependends on the spin of the electrons. Such a device musts necessary operate exploiting some spin-dependent effects, originated from the interaction between the spin of the electrons and the magnetic properties of the material. The developement of these new devices would lead to many advantages, such as nonvolatility, decreased electric power consumption and increased data processing speed and integration density, compared with conventional semiconductor devices [1].
The influence of the spin on the mobility of the electrons in ferromagnetic metals was first suggested by Mott in 1936 [2], which proposed a spin-dependent conduction model, known as the Mott's two current model [3], based on the existence of two separate conduction channels for spin up and spin down electrons. The schematic density of state (DOS) of a ferromagnetic metal is shown in figure 1.1. In a metal, the electric current

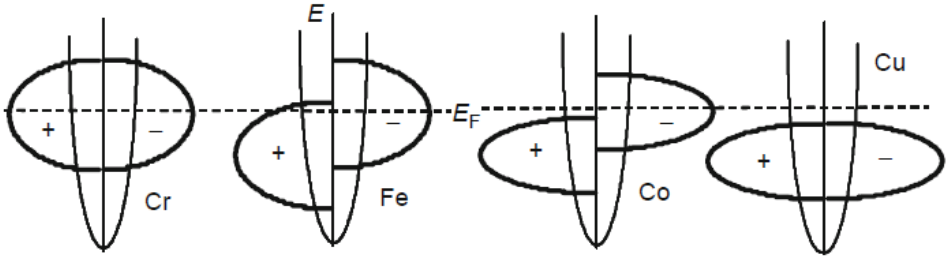

Figure 1.1: Schematic density of states for some metals. Of them, only Fe and Ni are ferroelectric.

is carried by the electrons at the Fermi level; because of the splitting in the energy of the two half-band , the majority and minority carriers of a ferromagnetic metal are in different states at the Fermi level, so they exibit different conductive properties. If the mean free path l results much shorter than the spin diffusion lenght λ_s, we can consider the spin up and spin down electrons as independent. Such a request is typically satisfied in ferromagnetic metals, and both spin up and spin down carriers will contribute to the transport with their own conductivity σ_s. Then, $\sigma = \sum_s \sigma_s$, with $s = \uparrow, \downarrow$ [3]. The ratio $\sigma_\uparrow/\sigma_\downarrow$ is usually referred to as the α-parameter.
The spin dependence of electrons in ferromegnetic metals was experimentally demonstrated and theoretically discussed by Fert and Campbell only in 1968 [4]. Moreover, they introduced a two current model that takes into account the momentum exchange between the two channel (spin mixing) [5, 6].

1.1 The Giant Magnetoresistance - GMR

The emergence of spintronics is generally associated with the discovery of the giant magnetoresistance (GMR) in 1988. Magnetoresistance (MR) consists in a change of the electrical resistivity of a conductor when an external magnetic field is applied. GMR was discovered independently by two research groups, which observed a very large magnetoresistive effect in magnetic multilayers (materials composed of alternate ferromagnetic and nonmagnetic layers of few nanometers thick). The group lead by Peter Grünberg used a Fe/Cr/Fe trilayer [7], wherease the group lead by Albert Fert used a $(\mathrm{Fe/Cr})_n$ multilayers where n could be as high as 60 [8]. For this discovery, Albert Fert and Peter Grünberg has been awarded the Nobel Prize in Physics 2007 [9].
The resistance of such multilayer devices appears lower when the magnetizations of the ferromagnetic layers are aligned, and higher when they are antialigned, so it is possible to switch between a low and an high resistivity states by changing the relative orientation of the magnetizations. The magnetoresistance ratio is defined as

$$\mathrm{MR} = \frac{\rho_{AP} - \rho_P}{\rho_P}, \tag{1.1}$$

where ρ_{AP} and ρ_P are the device resistivities in the antiparallel and parallel alignment, respectively. The value of MR = 0.85 for the (Fe 3 nm/ Co 0.9 nm) multilayer obtained in [8] by Fert *et al.* has been calculated with this formula. The alternative definition $\mathrm{MR} = (\rho_{AP} - \rho_P)/\rho_{AP}$ returns a value of about 0.45.
The interaction between the ferromagnetic layers can be controlled throught setting the thickness of the antiferromagnetic interlayer. In the Grünberg and Fert experiments an antiferromagnetic coupling between Fe layers was obtained using Cr interlayer. The switch from antiparallel to parallel magnetization, i.e. from high to low resistivity, was

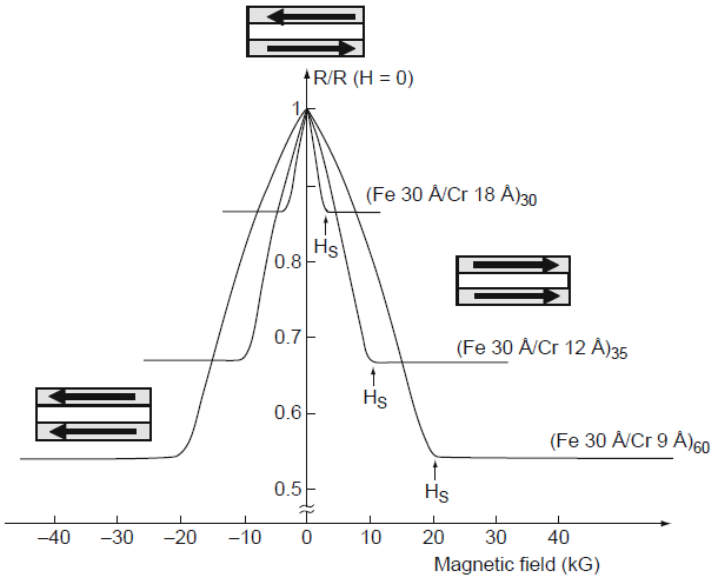

Figure 1.2: First observation of giant magnetoresistance. The samples consisted in $(\mathrm{Fe}(001)/\mathrm{Cr}(001))_n$ multilayers prepared by molecular beam epitaxy. The measurement were performed at 4.2 K. The current and the applied field were along the same [110] axes in the plane of the layers [8].

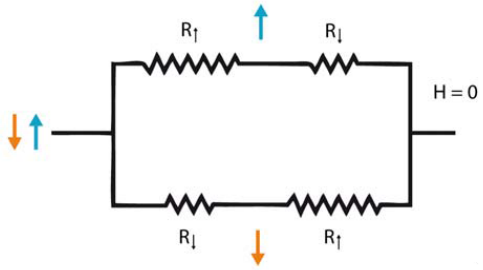

Figure 1.3: Circuital representation for the antiparallel alignment ($H = 0$) of magnetizations from the point of view of resistivity [9].

done throught the application of an appropriate external magnetic field. However, antiferromagnetic interlayer is not essential. GMR can be obtained also in devices with magnetic layers of different coercitivities.
Two main configuration exist, where we can observe GMR effect: the current can be perpendicular to the layers interfaces (current perpendicular to plane CPP) or parallel to them (current in plane CIP). In general, GMR effect is much larger in the CPP geometry than that in CIP.
The GMR behaviour of magnetic multilayers can be explained in terms of the Mott's two current model. Indeed, the thickness of each layer ($\sim 1\,\text{nm}$), which represent the typical lenght scale of the process, is shorter than the mean free path and much shorter than the spin diffusion lenght [3]. This model assumes that the current is composed of two types, and the resistance of this types is not the same in ferromagnetic materials, but depends on the relative orientation between spin and layer magnetization. However, this difference in resistivity is due not only to the spin dependent scattering in the ferromagnetic layer, but also to the scattering process at the ferromagnetic/non-magnetic interfaces. Since majority and minoriy carriers have different DOS at the Fermi level, also this additional resistance will be spin dependent. Moreover, we will neglect the resistance of the non-magnetic layer [9].
We consider, for simplicity, the CPP-GMR effects on a ferromagnetic/non-magnetic/ferromagnetic (FM/NM/FM) trilayer. Let ρ_+ and ρ_- be the resistivity experienced by, respectively, the majority and the minority spins in the ferromagnetic layers. When the magnetic layers have antiparallel magnetization ($H = 0$), both the channels result formed by the series of an high and a low resistance layer (see figure 1.3), giving a total resistivity of $\rho_{AP} = (\rho_+ + \rho_-)/2$.

When the alignment is parallel ($H \neq 0$), one kind of carriers, as an example majority, experiences an high resistance flowing through both the magnetic layers. In the same way, the other kind of carriers experiences a low resistance in both layers. So, the total resistance will be formed by the parallel of an high resistance channel and a low resistance channel (figure 1.4). We obtain $\rho_P = 2\rho_+\rho_-/(\rho_+ + \rho_-)$.

Using the definition (1.1) and the α parameter $\alpha = \rho_-/\rho_+$, we have the following

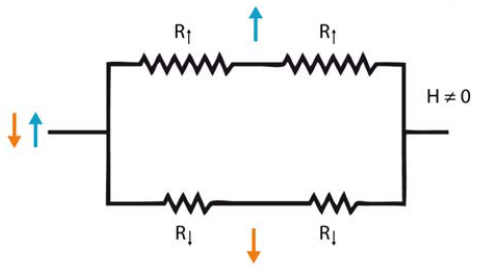

Figure 1.4: Distribution of the electrical resistivities for the parallel alignment ($H \neq 0$) [9].

magnetoresistance ratio:

$$MR = \frac{(1-\alpha)^2}{4\alpha}. \tag{1.2}$$

More sophisticated models, that takes into account the interlayer resistivity and spin-flip scattering, and also microscopic theory of GMR has been developed [3].
The simplest and most common GMR-based devices are spin valves. A spin valve consists on a trilayered structures, in which one of the two magnetic layers is pinned by exchange bias with an antiferromagnetic layer, so it results insensitive to moderate magnetic fields. By contrast, the magnetization of the "free" layer can be reversed by very small magnetic fields. An example of GMR in spin valve is show in figure 1.5.
Important developments has been achieved in the past years by the research on GMR based devices [11]. One of the greatest technological advance is represented by the replacement, in 1997, of the anisotropic magnetoresistance (AMR) sensors, with the GMR spin valve-based sensors in the read head of the hard disk drives (HDDs). Such a substitution has led to an increase of the areal recording density (see figure 1.6) by more than two order of magnitude in ten years, from about 1 Gbit/in.^{2} in 1997 to about 600 Gbit/in.^{2} in 2007 [12].

1.1.1 Spin Accumulation at the Ferromagnetic/Non-magnetic Interface

As said before, CPP geometry ensures larger GMR than the CIP. Moreover, in the CPP configuration the spin diffusion length λ_s, results the unique scale length for the spin transport [13]. In the usual conditions the spin diffusion length is much longer[1] than the mean free path, which governs the transport in the CIP geometry. Among other thing, this fact allow us to neglect spin mixing for layer thickness much shorter than the spin diffusion length [13].
The above-cited transport properties of CPP-GMR are related to the *spin accumulation*

[1] In the low temperature limit the spin diffusion length is governed by spin-orbit and exchange scattering. In some multilayers it can exceed 10^3 Å [13].

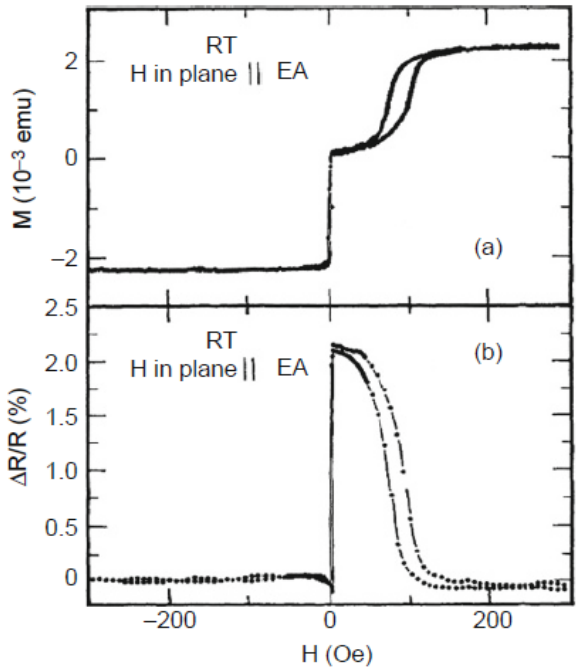

Figure 1.5: GMR effect in a NiFe/Cu/NiFe/FeMn spin valve [10].

effect, appearing when an electron flux crossing a FM/NM interface. The spin accumulation mechanism is shown in figure 1.7. Far from the interface, in the magnetic side, the current is larger in one of the spin channel (for instance spin up). In the NM side, far from the interface, the two channels partecipate to the conduction with an identical contribution. This leads to an accumulation of spin up electrons, which will correspond a spin down depletion, at the FM/NM interface. Such an accumulation diffuses from the interface in both layers with a scale length corresponding to the spin diffusion length [9]. So, the main consequence of spin accumulation is the formation of a spin-polarized current at a disance much longer than the mean free path. What is also important is that such mechanism can be applied to multilayers, i.e. multi-interface systems, resulting in the overlap of the spin accumulations.

1.2 The Tunneling Magnetoresistance (TMR)

Tunneling magnetoresistance TMR is observed in magnetic tunnel junctions (MTJs) (the term "ferromagnetic tunnel junction" [FTJ] is also used). MTJs are formed by two ferromagnetic electrodes, separated by a thin ($\sim$ 1 nm) non-magnetic insulator. Typically, the electrodes are made of Fe, Co or their alloys. The electrical resistance of

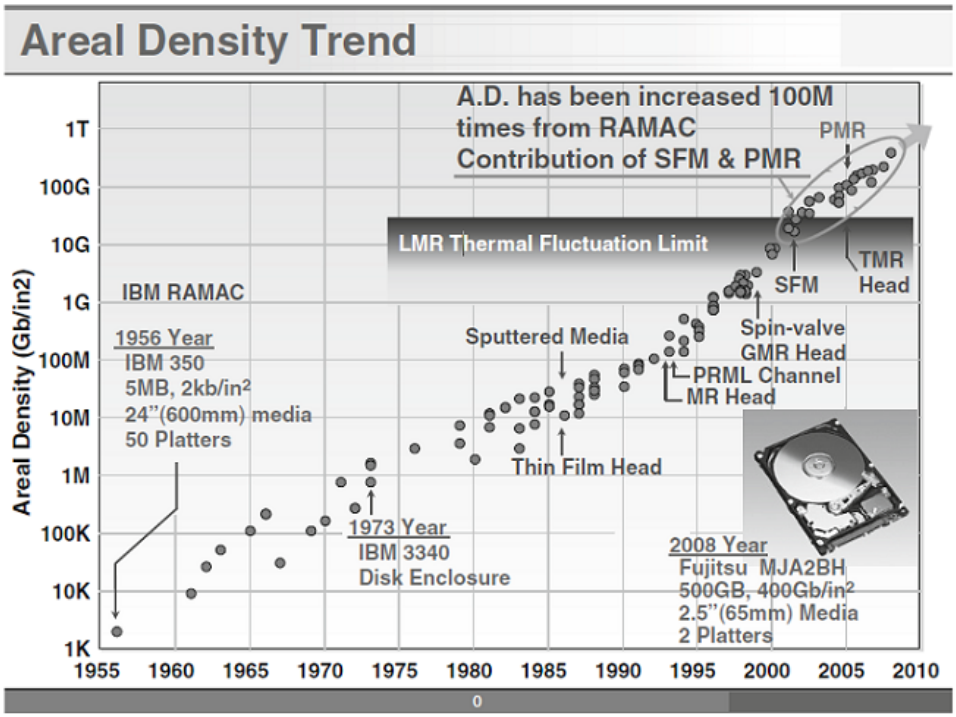

Figure 1.6: Areal density trend of magnetic recording systems from 1956 to nowdays. SFM and PMR stands for synthetich antiferromagnetism and perpendicular magnetic recording, respectively. [3].

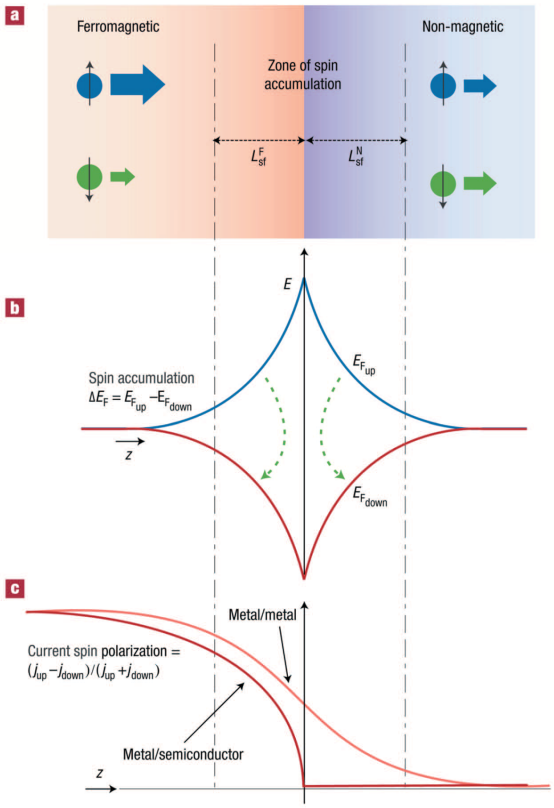

Figure 1.7: Schematic representation of the spin accumulation at the FM/NM interface. (a) Spin up and spin down current far from the interface. Electrons going from the magnetic to the non-magnetic conductor. L_{sf} stands for "spin diffusion length". (b) Splitting of the Fermi energies for spin up and spin down electrons. (c) Variation of the current spin polarization for metal/metal and metal/semiconductor interface. [11].

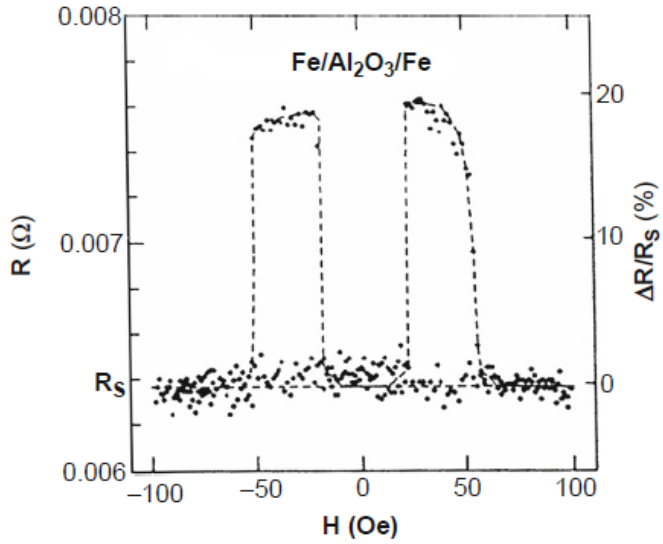

Figure 1.8: Resistance as a function of external magnetic field for an $Fe/Al_2O_3/Fe$ junction observed in [16].

such devices depends on the relative magnetization of the two electrodes. For the MR ratio we adopt the same definition (1.1) used for the GMR.
First observation of TMR effects dates back to 1975 (Jullierè), but the results were difficult to reproduce and the MR ratio was rather small. It is only in 1995 that large and reproducible TMR effects were obtained, at room temperature, in a MTJ with a tunnel barrier of amorfous allumina Al_2O_3 and Fe electrodes (Moodera et al. [15], Miyazaki et al. [16, 17]). The experimental results obtained in [16] are shown in figure 1.8; the resistance is high for antiparallel magnetization and it is low when the magnetizatios are parallel. When this appens, the tunnel magnetoresistance is called "normal" TMR. In the opposite case, when the resistance in the AP alignment is lower than that in the P alignment, we talking about "inverse" TMR. Inverse TMR is verified, as an example, in some $Co/SrTiO_3/La_{1-x}Sr_xMnO_3$ systems [18].
As a result of the presence of the insulating barrier, in MTJ there is almost no coupling between the ferromagnetic layers. So, the external magnetic field required to switch between the high and the low resistance states is quite low. The AP and P alignments are realized through small difference in the electrodes coercitivities.
The Jullierè model of TMR assumes, again, the existance of two conductive channels, associated to the two spin polarization. The tunnel conductance of each channel is proportional to the product of the densities of states of the left and right electrodes.

Than, for the total conductance G we have:

$$G \propto \sum_s D_{Ls} D_{Rs}, \tag{1.3}$$

where D_{Ls} and D_{Rs} are the densities of states of, respectively, the left and right electrodes at the Fermi energy E_F, and the sum is extended on the two possible spin values s. The conductance for the parallel P and antiparallel AP magnetizatios alignments will be given by

$$G_P \propto D_{L+} D_{R+} + D_{L-} D_{R-}, \tag{1.4}$$

$$G_{AP} \propto D_{L+} D_{R-} + D_{L-} D_{R+}. \tag{1.5}$$

This model neglects the dependence of the tunnel precess on the wave vectors of the involved electrons and it assumes the same transmission coefficient for each process. The definition (1.1) for the magnetoresistance ratio can be written in terms of the conductance as $MR = (G_{AP}^{-1} - G_P^{-1})/G_P^{-1}$. Defining the spin polarization of an electrode as

$$P = \frac{D_+ - D_-}{D_+ + D_-}, \tag{1.6}$$

the MR ratio becomes

$$MR = \frac{2 P_L P_R}{1 - P_L P_R}. \tag{1.7}$$

The tunnel process that leads to TMR is schematically shown in figure 1.9. We note that the magnitude of the magnetoresistive effect depends only on the spin polarization of the electrodes.

The polarization P of an electrode can be determined by measurement on FM/Al_2O_3/S junctions, where S is a superconductor. However, the behavious of ferromagnet/insulator (FM/I) interfaces results strongly dependent on the choice of the insulator. So, the spin polarization of an electrode can't be considered as an intrinsic propertie of the used material, and the knowledge of the *effective polarization* of each FM/I interface is required. It is known that interfacial effects can even reverse the spin polarization of the electrodes, as happens at the Co/$SrTiO_3$ interface [18]. When the sign of spin polarization for the two electrodes is opposite to each other we have $P_L P_R < 0$, i.e. the parallel configuration becomes more resistive than the antiparallel, and inverse TMR appears. In [18] it has been shown that half-metallic electrodes, i.e. material which are metallic for one of the spin direction an insulating for the other one, can be used as spin analyzer to determine the effective polarization of FM transition metal/I junctions. In particular, a Co/$SrTiO_3$/$La_{0.7}Sr_{0.3}MnO_3$ tunnel junction[2] was used (inverse TMR of -50% has been observed) to probe the Co/STO interface.

[2]The properties of the manganite $La_{0.7}Sr_{0.3}MnO_3$ will be discussed in 2.2.

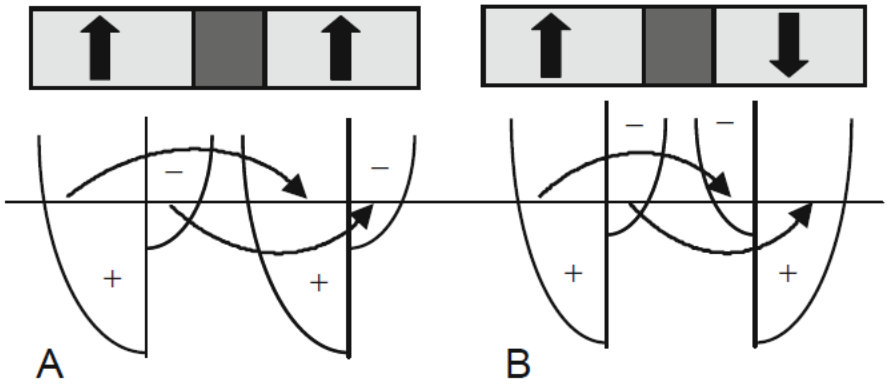

Figure 1.9: Schematic representation of the tunnel process in the parallel (left) and antiparallel (right) magnetization [3].

The dependence of the effective polarization on the insulating material exhibited by epitaxial MTJs, results from the fact that single crystal berriers filters the symmetry of the wave functions of the tunneling electrons. Than, the TMR is no longer depending on the whole spin polarization of the electrodes, but only on the spin polarization of the selected symmetry.
In figure 1.10 it is shown the DOS of evanescent waves functions of different symmetries in a MgO(001) single crystal barrier with Co electrodes [19]. Tipically, the Bloch state of the barrier with highest symmetry is also the most slowly decaying state. Spin filtering can occur if the ferromagnetic electrode has a state with this symmetry at the Fermi energy for one spin channel, but not for the other [20]. As shown in figure 1.10, the MgO barrier selects the Δ_1 symmetry. Since at the Fermi energy of Co this symmetry is well represented by the majority electrons, i.e. they have a larger DOS, the low resistance configuration is obtained for parallel magnetization of the electrodes. By contrast, a $SrTiO_3$ barrier tends to select evanescent wave functions of Δ_5 symmetry. In Co this symmetry is much more represented by minority spin states then by majority, resulting in a large negative tunneling polarization of the $Co/SrTiO_3$ interface. This eplains the inverse TMR observed in $SrTiO_3$-based MTJs.
The spin-filter effect described above is at the origin of giant TMR observed in MgO-based MTJ by Parkin *et al.* [21] and Yuasa *et al.* [22] in 2004. This fact has represented an important step in the development of MRAMs.

1.2.1 The Magnetic Random Access Memories - MRAM

The MTJs are at the basis of the magnetic random access memories (MRAMs), which are expected to combine the nonvolatility of the magnetic systems and the short

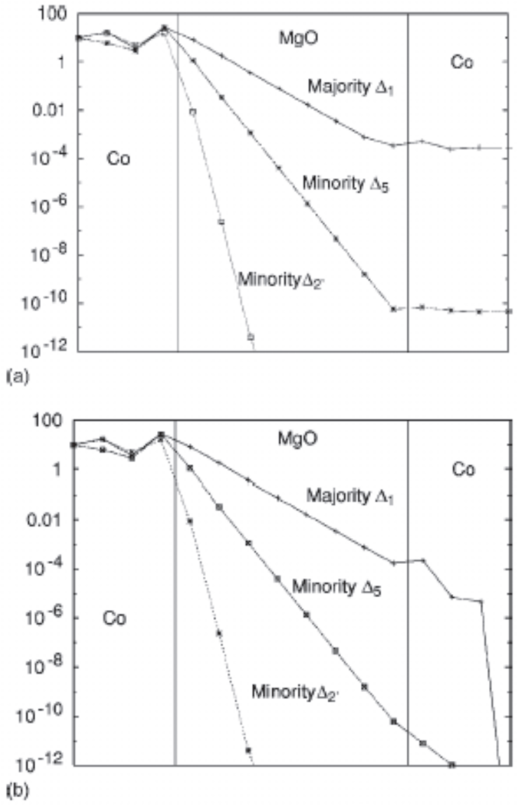

Figure 1.10: Decay of evanescent electronic waves of different symmetries in a Co/MgO(001)/Co MTJ in the parallel (above) and antiparallel (below) configuration. [19].

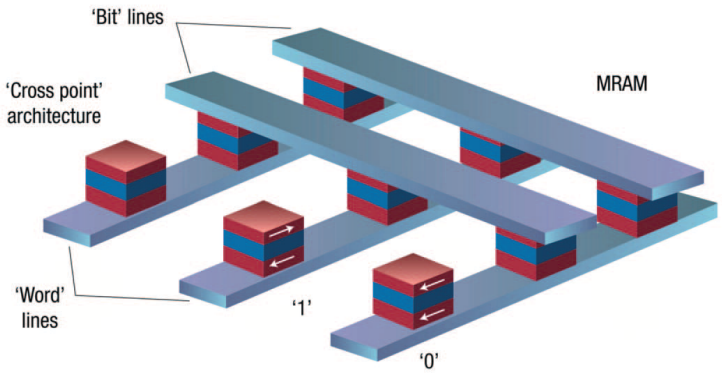

Figure 1.11: Schematic representation of a magnetic random access memory (MRAM) in the *cross point* architecture [12].

access time of the semiconductor-based memories (RAMs) [12]. The typical "cross point" structure of an MRAM is shown in figure 1.11. The "1" and "0" binary informations are recorded exploiting the parallel and antiparallel alignment of the ferromagnetic layers of a MTJ. An MRAM device is composed of several MTJs connected to the crossing point of two perpendicular arrays of parallel conducting lines. The writing process is done sending current pulses through the appropriate conductive lines (one for each array); only at the cross point of these lines the magnetic field will be high enough to orient the free layer magnetization. For reading it is sufficient to measure the resistance between the lines.
However, in spite of the expected achievement of high recording density, the MR ratio remains to low for fast and reliable reading. Then, an additional transistor per cell has been proved necessary to remove the unwonted current paths [11]. The requirement of one transistor per cell, resulting in a more complex 1T/1MTJ architecture (figure 1.12), represents one of the most serious limitations to the development of ultra-high-density MRAM.

The problem of the writing process is characteristic of magnetic memories. If the information is represented by the magnetization of a single domain body of volume V, than the energy needed to reorient the magnetization will be given by KV, where K is the anisotropy constant per unit volume. For very small V, thermal fluctuation can be high enough to overcome the energy barrier. To ensure a maximum error rate of, as an example, 10^{-9} on a 10-year period we must require that $KV > 50 - 60k_BT$, where k_B is the Boltzmann constant and T the temperature. So, a reduction in the dimension should be accompanied by an increase in K. Unfortunately, higher anisotropy requires higher writing fields and, ultimately, higher currents. This problem is particularly grave

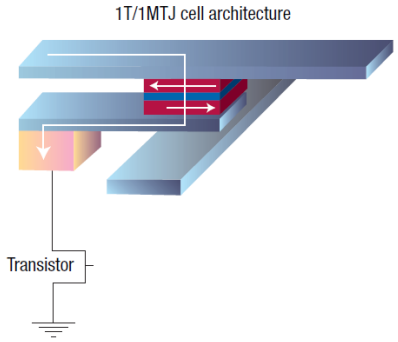

Figure 1.12: Schematic representation of an MRAM cell in the 1T/1MTJ architecture. To remove the unwonted currents one transistor is added [11].

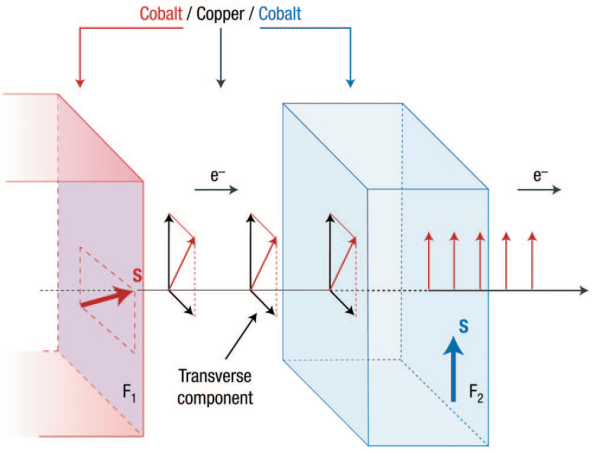

Figure 1.13: Illustration of the spin transfer torque mechanism [12].

in MRAM because of the small dimensions of the conductive lines [11].

1.2.2 Magnetic Switching by Spin Transfer Torque

Spin transfer consists in the manipulation of a magnetic dipole moment by the application of a spin-polarized current. The relative orientation between the current spin polarization and the magnetization axis of a magnetic layer, results in a torque on the latter. Such a torque can produce an irreversible reorientation of the magnetization or, in the apposite conditions, it can generate precession of the moment in the microwave frquency. In practice, a transverse spin polarized current is prepared using a first magnetic layer F_1 (see figure 1.13). As this current goes throgh a second magnetic layer F_2 with a different orientation of magnetization, a spin conserving exchange interaction occours. The spin polarization lost by the current is transferred to the total spin of F_2. The spin transfer torque STT was predicted independently by Slonczewski [23] and

Berger [24] in 1996, and was observed in 2000 by Katine *et al.* [25] using pillar-shaped metallic trilayers. The spin transfer mechanism has been considered, from the first moment, very attractive for the switching of MRAM. For this type of memory the term STT-MRAM is used. Commercial development of STT-MRAM started in 2002 at Grandis Inc. and actually several companies are working on STT-MRAM. The challenge of this research field is related with the achievement, in the same device, of the high storage density of DRAM and the speed of SRAM, combined with non-volatility [26].
Another important consequence of the spin-transfer fenomena in trilayers, consists in the formation of voltage oscillation in the microwave frequency range, when a large magnetic field is applied. If the magnetic field is high enough, instead of the switch of the free layer magnetization, a transverse spin-polarized current can induce a precession of the layer magnetic moment. The periodic variation of the angle between the magnetizations of the layers is accompanied by an oscillation in the resistance of the trilayer. As a consequence, a voltage oscillations in the microwave frequencies range is generated [12]. So, the spin transfer mechanism provides the possibility to develop a new generation of oscillator devices, spin transfer oscillators (STOs), in which the frequency can be controlled by changing a dc current.

1.3 Spintronics with Semiconductors and Molecular Spintronics

A very active research field is spintronics with semiconductors, which has introduced new concepts, such as spin field-effect transistors (spin FETs), combining the features of semiconductors and that of magnetic materials. A spin FET is a device in which spin transport between spin polarized source and drain is controlled by a field-effect gate.
The two main approaches to spintronics with semiconductors concern hybrid structures, in which ferromagnetic metals and nonmagnetic semiconductors are combined, and ferromagnetic semiconductors, such as $Ga_{1-x}Mn_xAs$ with x of a few percent [12]. However, both this approaches present some difficulties. As concerning ferromagnetic semiconductors, the main problem is represented by the low Curie temperature of most interestig materials, such as $Ga_{1-x}Mn_xAs$ ($T_C \sim 170\,K$) [12]. On the other hand, the difficulties with hybrid structures concern the spin injection in semiconductors and arise from the impedance mismach between ferromagnetic metals and semiconductors.
It is known that spin-polarized current in semiconductors can be obtained by electrical transfer of spin from a ferromagnetic metal across a spin-dependent interface resistance [12]. An important step forward in this way has been taken in 2009, when room temperature injection of spin polarization has been achieved into both n and p-type silicon from a ferromagnetic tunnel junction [27].
A further way for spintronics with semiconductors is related to the spin Hall (or Rashba,

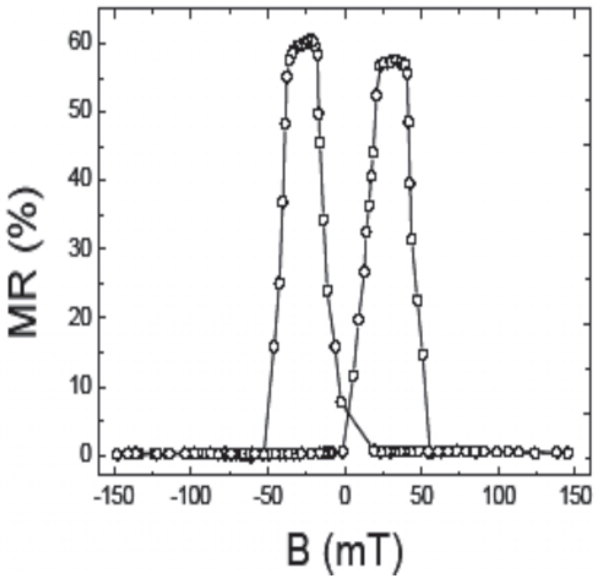

Figure 1.14: Magnetoresistance obtained in [27] for an LSMO-CNT-LSMO device at 5 K with a bias voltage of 25 mV. The magnetoresistance ratio was calculated with the formula $MR = (R_{AP} - R_P)/R_P$.

or Dresselhaus) effect. In practice, spin-orbit interaction deflects the electrons of the spin up and spin down channels in opposite transverse directions, thus producing spin polarized currents even in nonmagnetic conductors.
Another promising road is molecular spintronics, which purpose is the creation of devices based on one or a few organic molecules. A notable advantage of organic molecules is represented by a very long spin lifetime, combined to an high Fermi velocity. Such a combination allows to preserve spin coherence over distance much longer than that in semiconductors (and also in metals). Consequently, very high value of magnetoresistance can be obtained. In figure 1.14 is shown an example of high magnetoresistance obtained with carbon nanotubes (CNT) between two electrodes made of manganite ($La_{0.7}Sr_{0.3}MnO_3$) [12].

1.4 Magnetically Enhanced Memristors - MEM

The term *memristor*, a contraction for the expression *memory resistor*, indicates a non-linear, passive circuit component. Introduced in 1971 by Chua [29], it is considered the fourth fundamental circuit element, beside the capacitor, the resistor and the inductor. Memristance is often defined as the relationship between electric charge and magnetic flux, in the same way as the resistance represents a link between the applied voltage and the current that flow trough a device. However, the definition of memristance is more general and doesn't require the magnetic interaction [30].
A memristor is a bipolar element whose resistance is not a constant, but depends on

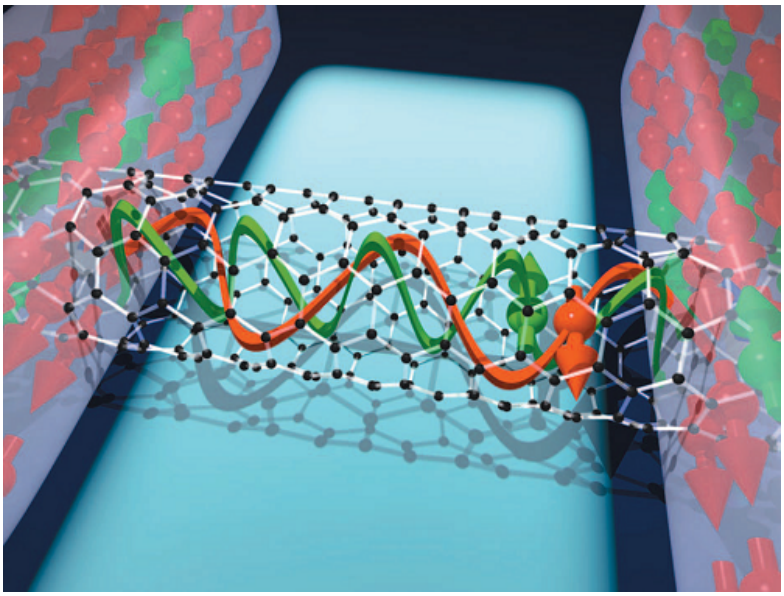

Figure 1.15: Graphic representation of spin transport trough a CNT channel between two LSMO electrodes [12].

the history of voltage or current experienced by the device. The non-volatility aspect of such devices, make memristors very attractive for computer memory, the so called resistive-random access memory (RRAM). A further reason of interest on memristors follows from the possibility to fabricate multifunctional devices able to perform both storage and processing operation.
A promising approach coming from spintronics combines the magnetic bistability offered by spin valves, whith non-volatile electrical memory effects.

Spin Transport in Memristive Device [31] Memristive behaviour with on/off resistance ratio of 10^5 has been observed in magnetoresistive metal-oxide devices with ferromagnetic electrodes [31]. The I-V characteristic of a Co/TaO_x/Cu/Py device, with 16 nm TaO_x-thick is shown in figure 1.16. In these devices the resistance switching mechanism is related to the formation of continuous metallic conduction paths.
The MR effect is observed in the low resistance state, that is obtained for a bias voltage between $-1\,\mathrm{V}$ and $-1.5\,\mathrm{V}$. In the high resistance state, reached for less than $1\,\mathrm{V}$, the MR effect disappears. The MR measurements performed on the low ($\sim 300\,\Omega$) and high ($\sim 130\,\mathrm{M}\Omega$) resistance states are shown in figure 1.17. The memristive behaviour of TaO_x-based devices is attribuited to the creation/annihilation of Cu filaments in TaO_x. The authors of [31] demonstrate that the creation and annihilation of a spin channel by an external voltage, can be used to switch the magnetoresistive effect in TaO_x-based

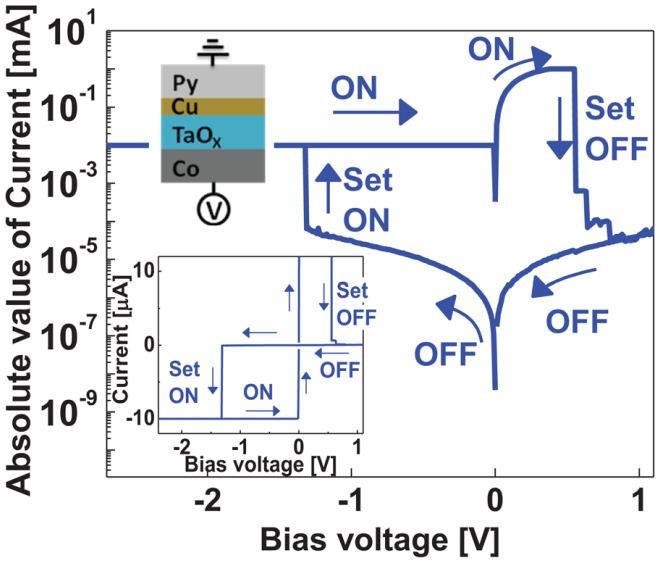

Figure 1.16: I-V characteristic of Co/-TaO_x/Cu/Py sample at room temperature in log-scale and in linear scale [31].

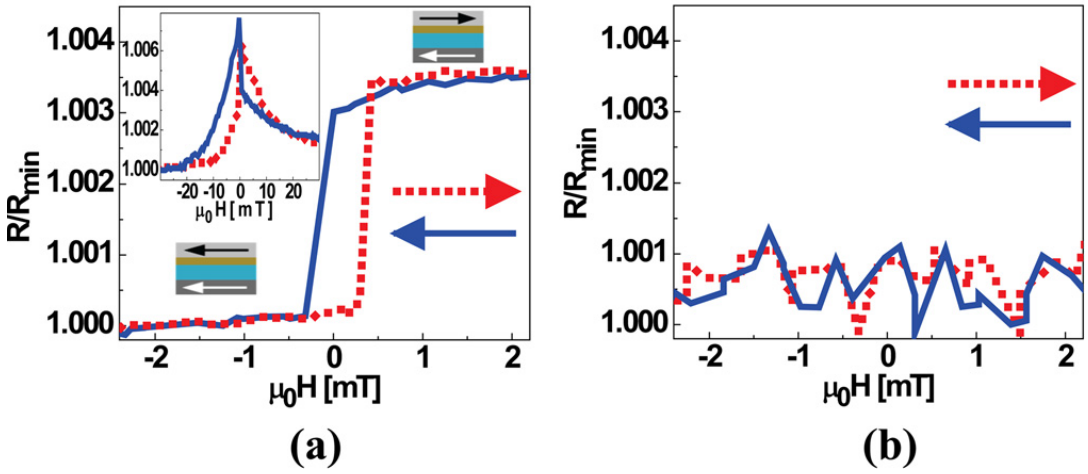

Figure 1.17: Magnetoresistance measurements on the same Co/TaO_x/Cu/Py device in the (a) low resistive state and in the (b) high resistive state at 77 K [31].

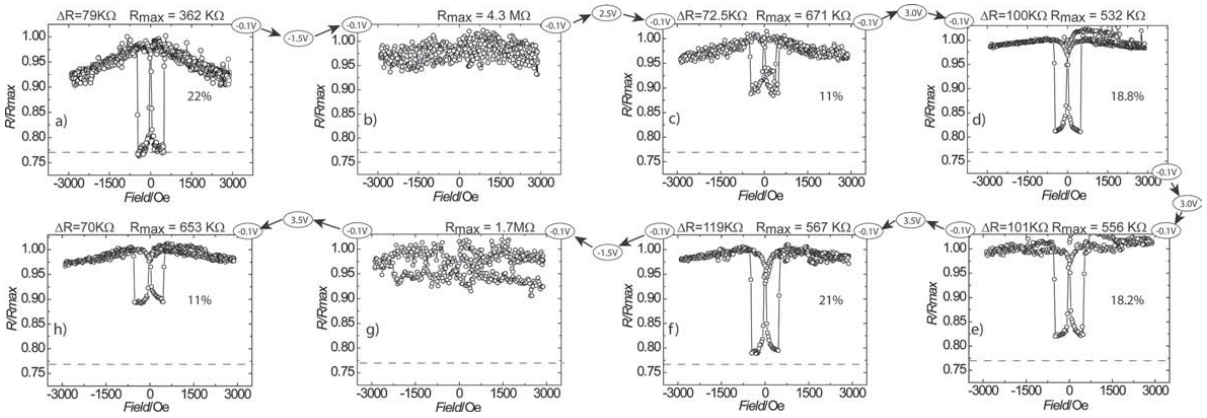

Figure 1.18: Electrical tuning of MR effects in a LSMO/Alq_3/AlO_x/Co device, with an Alq_3 thickness of 250 nm and LSMO bottom electrode of 20 nm-thick. The MR measurements were performed at -0.1 V, at 100 K [32].

devices in an ON/OFF manner.

Electrically Programmable MR in Organic Devices In [32] the electrically controlled magnetoresistance effect has been achieved using organic Alq_3-based spin valves. In practice, it is demonstrated that the magnetoresistance can be reversibly modified in a non-volatile manner by applying an electric field. The overall structure of the devices used in [32] is $La_{0.7}Sr_{0.3}MnO_3$/Alq_3/AlO_x/Co. In such devices the coexistence of magnetoresistance and electrical switching has been observed. At zero bias voltage the samples show a magnetoresistance effect of about 22%, that represents a remarkable value for organic devices. Meanwhile, the same samples exhibit electric bistability. Appliyng a positive threshold voltage V_{th+} the device switches to a low resistance state; such state is preserved until the bias is reversed to a negative threshold V_{th-} (the voltage is negative when the electrons are injected from the LSMO electrode).
In figure 1.18 the measurement of mangetoresistance at different resistance mode are shown. In this experiment the device was moved from one resistive state to another resistive state appliyng positive or negative threshold voltage. Than, a MR measurement were performed at -0.1 V. As shown At -1.5 V the spin valve effect is completely erease. The spin valve effect is partially recovered appliyng positive bias of 2.5 V ($MR = 11\%$) and 3.5 V ($MR = 18\%$), and it is completely recovered after the application of 3.5 V ($MR = 22\%$).
Also in this case the transport behaviour is explained assuming the creation/annihilation of conductive path between the two electrodes.

Chapter 2

The Perovskite Oxides

Perovskite is a structural family with the general formula ABX_3 and with crystal structure related to the mineral perovskite $CaTiO_3$. Among the numerous compounds that crystallize in this structure, the most relevant are oxides, with general formula ABO_3. The wide variety of properties that these compounds exhibit, such as ferroelectricity, ferromagnetism and superconductivity, is derived from the fact that about 90% of metallic natural elements of the Periodic Table are stable in a perovskite-tipe oxide structure [33]. By changing composition, this compounds can perform several different functionalities: high k capacitors ($BaTiO_3$), piezoelectrics ($Pb(ZrTi)O_3$), insulators ($SrTiO_3$), metallic conductors ($LaCrO_3$), high T_c superconductors ($YBaCuO_3$), catalysts ($La(Co,Mn)O_3$) and magnetoresistance devices ($LaMnO_3$).
The ideal perovskite has cubic structure with space group Pm3m-O_h^1, but deviation from cubic symmetry, such as tetragonal, orthorhombic or rhombohedral symmetry, are frequent [33, 34]. A and B cations have significantly different sizes and we denote by A the cation of major radius. The arrangement of the ions is shown in figure 2.1(a); the A cations occupy the center of the cube, the B cations are located at the corner, and the oxygen anions are placed at the center of the cube edges. In this way, the A and B cations are, respectively, 12-fold and 6-fold coordinated with oxygen anions, and the B ions result located at the center of BO_6 octahedra. Another way to present the same structure is shown in figure 2.1(b).
Denoting by a the cubic unit cell parameter, the distance between B and O ions is equal to $a/2$, whereas the A-O distance is $a/\sqrt{2}$. Then, we can write the following relation between the ionic radii:

$$r_A + r_O = \sqrt{2}(r_B + r_O). \tag{2.1}$$

However, in the case of real compounds equation (2.1) is not exactly obeyed and the ideal cubic perovskite is quite rare; this fact leads to the important concept of the *tolerance factor*, introduced by Goldschmidt [35] in 1926, as a measure of the deviation from the

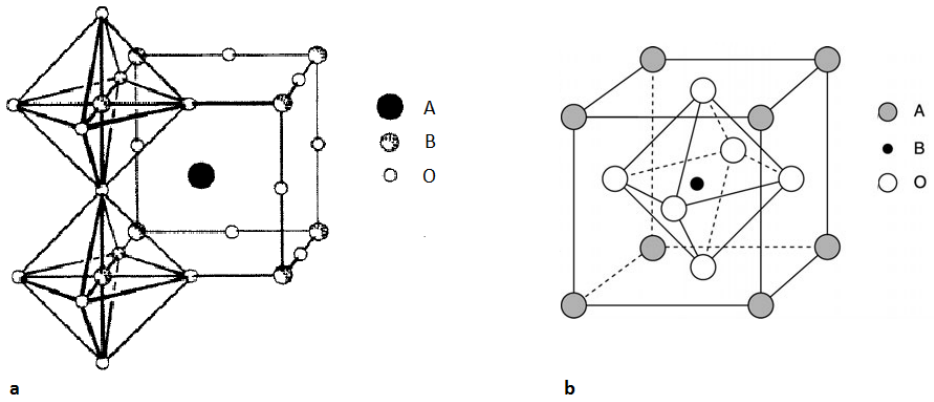

Figure 2.1: (a),(b)Different ways to present the ideal perovskite structure.

ideal ionic sizes:

$$t = \frac{r_A + r_O}{\sqrt{2}(r_B + r_O)}. \tag{2.2}$$

The tolerance factor may be calculated at room temperature and atmospheric pressure using the tabulated ionic radii, but it is important to consider the dependence of t on temperature and pressure. Indeed, the termal expansions and compressibilitis of the A-O and B-O bond are usually different[1].

Although ideal cubic perovskite is obtained in a few cases[2] in which t is very close to unity, the perovskite structure is stable for $0.89 < t < 1.02$ [36]. When the tolerance factor is smaller than 1, i.e. r_A is smaller than the ideal value, the BO_6 octahedra result tilted.

It is well known that several properties, such as piezoelectricity, ferroelectricity and ferromagnetism, are related to the reduced simmetry of crystals, which is due to the structural distortion. As an example, in figure 2.2 is shown the correlation between the dielectric constant and the tolerance factor in some complex compounds.

Since the total charge of the cations must equals the charge of oxygen anions, possibles charge distribution are of the form $A^{1+}B^{5+}O_3^{2-}$, $A^{2+}B^{4+}O_3^{2-}$ and $A^{3+}B^{3+}O_3^{2-}$. Furthermore, partial substitution of A or B ions is allowed, so it is possible to obtain complex compounds with general formula $A'_{1-x}A''_xB'_{1-x}B''_xO_3$. The most frequent substitution involves the ions at the B site, with the B' and B" ions which are present with the same proportions. Then, the general formula of this compounds is $AB'_{1/2}B''_{1/2}O_3$, and we may

[1] For a discussion see [37], page 250.

[2] An example of ideal cubic perovskite is $SrTiO_3$, in which $t = 1.00$, $r_A = 1.44$ Å, $r_B = 0.605$ Å and $r_O = 1.40$ Å.

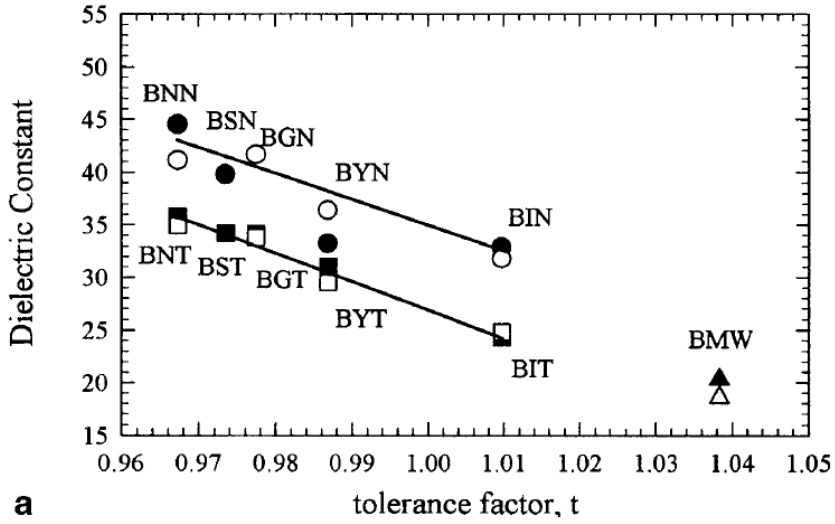

Figure 2.2: Dielectric constant vs tolerance factor in some $Ba(B'_{1/2}B''_{1/2})O_3$ complex compounds. [34, 38, 39]. B′ = Nd, Sm, Gd, Y, In and B″ = Nb, Ta.

define the tolerance factor as

$$t = \frac{r_A + r_O}{\sqrt{2}[(r_{B'} + r_{B''})/2 + r_O]}. \tag{2.3}$$

If B′ and B″ have different charge, the oxigen ion are shifted toward the more charged cation, producing a distortion of the octahedra.
An important cause of distortion is represented by deviations from ideal composition such as nonstoichiometry, the most common of which are oxygen vacancies. Oxygen deficient perovskites are described using the general formula $A_nB_nO_{3n-1}$ of the complex perovskite-releted superstructures. Oxygen excess, by contrast, is observed in few systems. The best characterizedperovskite that show oxidative nonstoichiometry is the manganite $LaMnO_{3+\lambda}$ [33].
Cationic vacancies are less frequent than oxygen vacancies. Some perovskites exhibit A-site vacancy, wherease B-site cation deficiency is not termodynamically favored. Composition with stoichiometry that might results in a perovskite with significant concentration of vacancies in B position, tend to cristallize in a mixture of perovskite and nonperovskite phases [33].
The last factor that we have to consider as a possible reason of distortion is the Jahn-Teller effect. Jahn-Teller theorem states that non linear spatially degenerate molecules cannot be stable and predict that the electronic degeneracy will be removed by the geometrical distortion of the molecule, that causes a symmetry breaking. The reached state will be characterized by lower symmetry and lower energy. In some perovskite, such as

manganites $LnMnO_3$ (with Ln = La, Pr or Nb), Jahn-Teller effect is activated by Mn^{3+} ions located at B positions. The electronic configuration of Mn^{3+} isolated ion is $3d^4$; in the crystal the five d orbitals are split into three t_2g orbitals and two e_g orbitals, but only one of the e_g orbitals is occupied. The odd number of electrons in the e_g orbitals causes an elongation of the MnO_6 octahedron.
The most frequent and characterized distorted structure are orthorhombic and rhombohedral, but also tetragonal, monoclinic and triclinic are known. Generally, the distorted phases may exist at a certain temperature and vanish with increasing temperature: at high temperature, perovskites tend to be cubic.

2.1 High-κ Dielectrics with Perovskite Structure - Titanates

The perovskite structure is usefull in most research fields, expecially in spintronics, owing to the already mentioned variety of properties exhibited by perowskite compounds, and because of the possibility to epitaxially grow multilayer devices. Of course, the composition and the mutual orientation of the different layers need to be compatible as concern the lattice space mismach. As an example, a rather common FM/I/FM tunnel junction consists of an $SrTiO_3$ insulator layer (STO $a = 3.905\,\text{Å}$), and one or both electrodes made of $La_{0.7}Sr_{0.3}MnO_3$ (LSMO $a \sim 3.88\,\text{Å}$). Strontium titanate and many other perovskite oxides are very attractive for spintronics, due to their insulating and dielectric properties, and can be employed as insulator barrier and gate dielectrics.
In this section the dielectric properties of some perovskites, in particular the titanates $BaTiO_3$, $SrTiO_3$ and $(Ba,Sr)TiO_3$, will be discussed. In this compounds, the main contribution to the dielectric constant is due to ionic dipoles; in a few words, the Ti ions displacement, in response to an applied electric field, can produce a very large polarization of the materials.
In figure 2.3 are shown the various contributions (electronic dipoles, ionic dipoles, etc.) to the permittivity at different frequency ranges. Ions respond slowly than electrons to an applied field, so the ionic contribution tends to diappear at very high frequencies. Then, the infrared range, at about $10^{12}\,\text{Hz}$, can be considered as an upper limit for the perovskite-based dielectrics. The relative permittivity for some materials is reported in table 2.1.

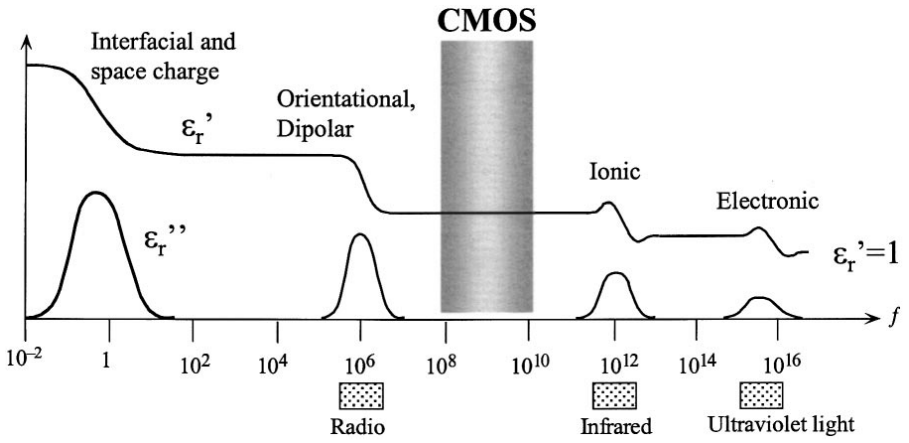

Figure 2.3: Frequency dependence of the real (ϵ'_r) and imaginary (ϵ''_r) parts of the permittivity. It is also highlighted the CMOS operation frequency range, in which ionic and electronic contributions are present [40].

Material	Dielectric constant
Silicon dioxide (SiO_2)	3.9
Silicon nitride	7-8
Alluminum oxide (Al_2O_3)	8-10
Neodymium gallate (NGO)	20[42]
Lanthanum aluminate (LAO)	23[42]
Zirconium oxide (ZrO_2)	14-28
Titanium oxide (TiO_2)	30-80
Tantalum pentoxide (Ta_2O_5)	25-50
Barium strontium titanate (BST)	100-800
Strontium titanate (STO)	230+
Lead zirconium titanate (PZT)	400-1500

Table 2.1: Indicative values of dielectric constant for some materials. All data are taken from [41], except that of LAO and NGO [42]. The dielectric constant of perovskite compounds strongly depends on many factors, such as composition, strains, etc.

2.1.1 Displacement Phase Transition in $BaTiO_3$ and Ferroelectricity

Barium titanate, $Ba^{2+}Ti^{4+}O_3^{2-}$ (BTO), is a ferroelectric material with perovskite structure and it represents the first discovered piezoelectric ceramic. The ionic sizes are $r_A(\text{Ba}) = 1.61$ Å and $r_B(\text{Ti}) = 0.605$ Å, which returns a tolerance factor of about 1.06. Starting from the '40s, during the World War II, barium titanate was employed as insulator to substitute mica in most capacitors. So, its high dielectric constant may be considered the first useful property in a perovskite-structure material. Barium titanate and barium titanate based compounds, still represent some very important materials in electronic industry due to their ferroelectric properties with high dielectric constant and low dielectric loss [43].
Depending on temperature, barium titanate can exist in five solid phases: hexagonal, cubic, tetragonal, orthorhombic and rhombohedral. We will restrict our discussion to the cubic and pseudocubic structures, which are the most common and characterized structures.
We may consider barium titanate as a prototype to illustrate the link between a physical property, in this case ferroelectricity, and the reduced simmetry of the crystal. Indeed, in $BaTiO_3$, ferroelectricity is linked with the properties of the TiO_6 octahedron: as the temperature is lowered, the octahedra are distorted and the Ti-O bonds become unequal.
Above the Curie temperature $T_C \simeq 133$°C, that is dependent on the impurity content, barium titanate presents cubic structure ($Pm3m$ symmetry) with lattice constant $a = 4.009$ Å. In this state, the equilibrium position of the Ti^{4+} ion is located at the center of the TiO_6 octahedra, so the unit cell does not contain permanent dipole moment and $BaTiO_3$ is paraelectric. At the curie temperature, the crystal undergoes a phase transition and the tetragonal structure ($P4mm$ symmetry) with $a = 3.992$ Å and $c = 4.035$ Å is formed. This phase is stable between 130°C and 0°C, with the c/a ratio that increases as the temperature drops (see figures 2.5 and 2.6). The TiO_6 octahedron results distorted: as shown in figure 2.4 the oxygen ions are shifted in the negative c direction, while the Ti ion is shifted in the positive c direction. As a consequence, the unit cell turns out to be permanently polarized and the lattice exhibit spontaneous polarization along the c-axis. The dipole moment can arise along any one of the six equivalent <100> axes wich are present in the cubic structure. As it is well known, the spontaneous polarization can be manipulated and a particular direction can be choosen by appliyng an external electric field.
Below 0°C, $BaTiO_3$ undergoes another phase transition and the unit cell becomes orthorhombic (Amm2). This phase is stable from approximately 0°C to −90°C. The cubic structure has 12 equvalent <110> directions, so there exist 12 possible directions of spontaneous polarization.
The last phase transition take place at about −90°C. The unit cell distorts from or-

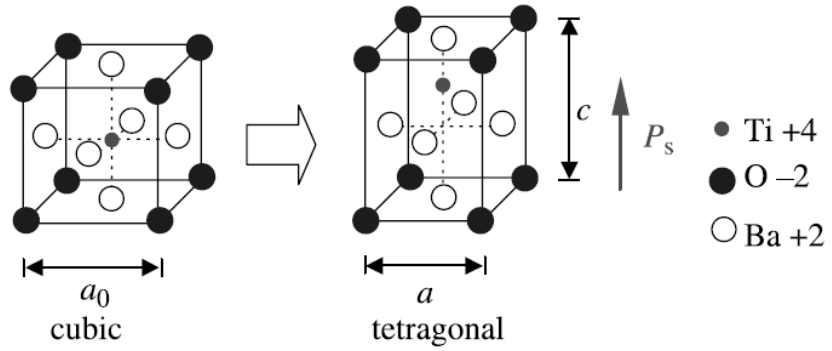

Figure 2.4: Distortion of the unit cell from cubic to tetragonal structure [44].

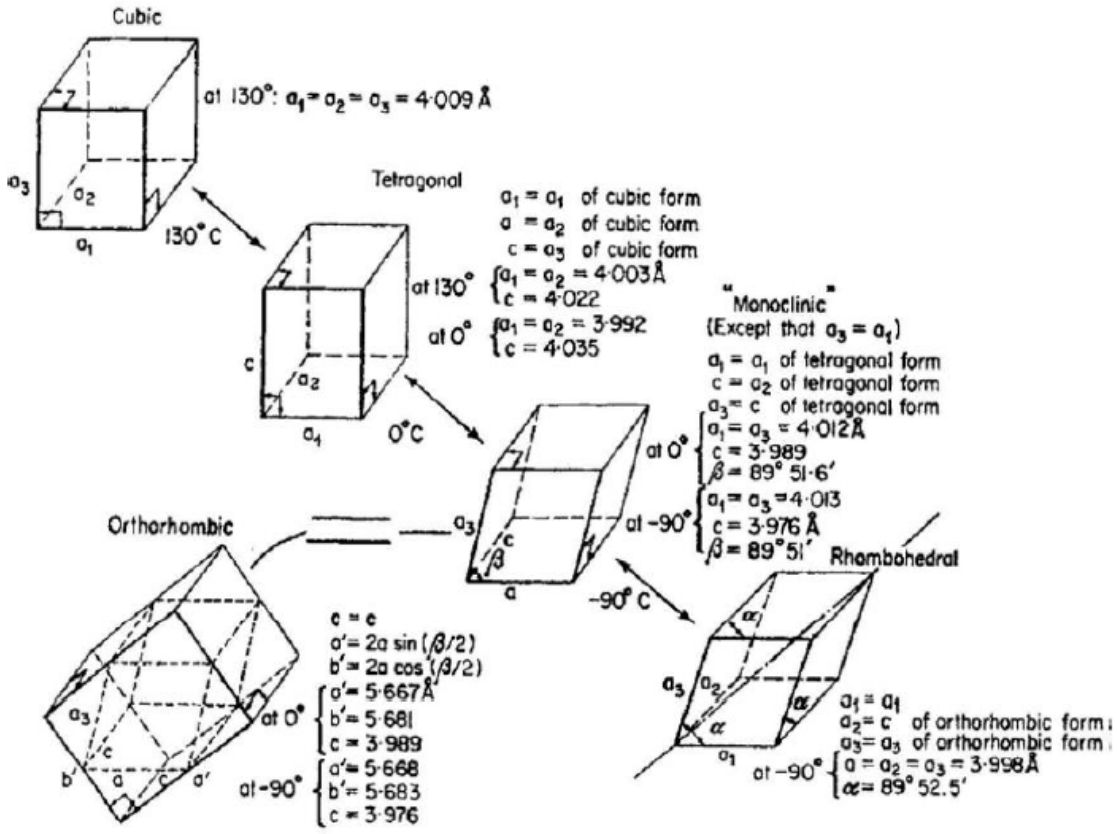

Figure 2.5: Temperature dependence of distortion of $BaTiO_3$ unit cell.

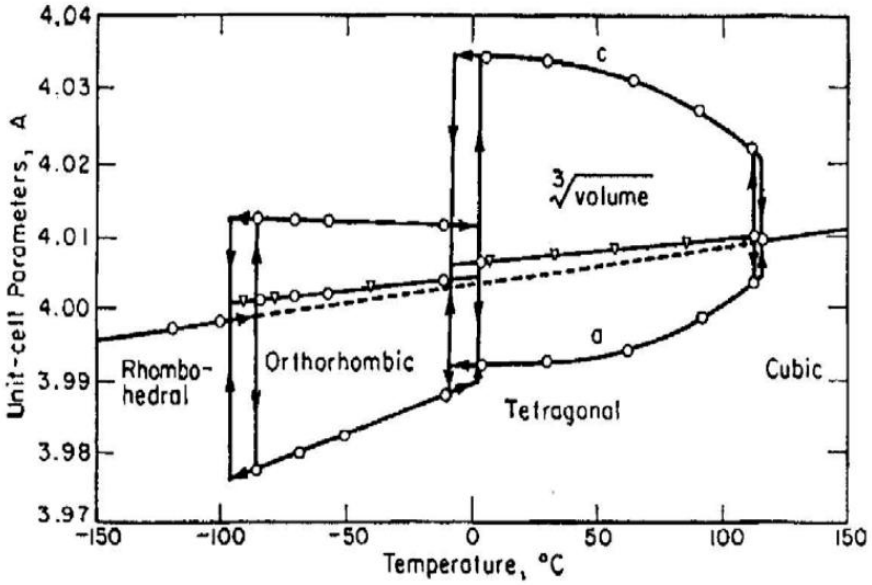

Figure 2.6: Lattice constants of $BaTiO_3$ as a function of temperature.

thorhombic to rhombohedral (R3m) and the polar axis is aligned along one of the 8 equivalent <111> directions of the original cubic phase.
We conclude that pseudocubic BTO exibits one paraelectric phase and three ferroelectric phases, one fo which, the tetragonal one, does exist also at room temperature. Partially substituted BTO single crystal and BTO thin films have been widely investigated because of the large tunability of their physical properties. Among the numerous effect due to partial substitution of the A site or B site ions, there is the possibility to shift the phase transitions temperature and, consequently, we can manipulate the dielectric and ferroelectric properties of this material by slightly changing the composition.
In figure 2.7 it is shown the dielectric constant of barium titanate single crystal as a function of the temperature. The sharp changes in the dielectric response are positioned at the phase transitions. In most applications, such as piezoelectrics, the main problem is just represented by the temperature instability around room temperature, wich is due to the tetragonal-orthorhombic transition at about 0°C, and by the lower Curie point at $T_C \sim 400$ K.
It is known [45] that the temperature stability can be improved by partial substitution of Ca for Ba ions. Indeed, in $(Ba_{1-x}Ca_x)TiO_3$ systems (BCT) the tetragonal-orthorhombic and also the orthorhombic-rhombohedral phase transitions are shifted toward lower temperatures as the Ca concentration increase; for $x > 0.23$, both this transitions completely disappear and the tetragonal phase remains the only stable ferroelectric phase. As shown in fig. 2.8, above the concentration of $x = 0.23$ the dielectric permittivity is nearly un-

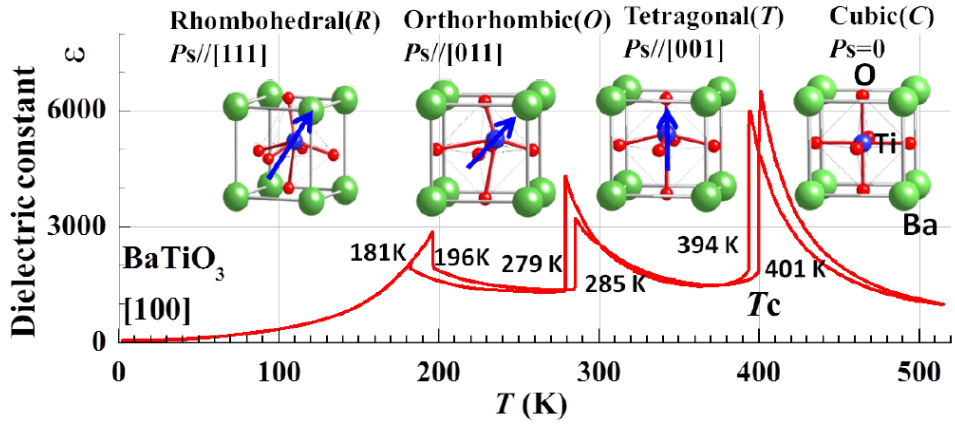

Figure 2.7: Change with temperature of $BaTiO_3$ dielectric constant (single crystal). It is also shown the Ti displacement in the various phases [45].

changed for temperatures lower than T_C. At the same time, the Curie point results almost independent of the Ca concentration.
The reasons of the ferroelctric behaviour of $(Ba_{1-x}Ca_x)TiO_3$ systems may be understand by considering the small size of the Ca ion, $r(Ca) = 1.34$ Å, compared to the largest size of barium, $r(Ba) = 1.61$ Å. The substitution of Ca for Ba causes the reduction of the unit cell volume, so it is natural to expect that the chemical pressure induced will affect the ferroelectricity and decrease the transition temperature. Nevertheless, the Curie point results independent of the Ca concentration[3]. As explained in [45, 46], the Ca ion, because of its small size, may has an off-centering displacement in the bulky A site[4], thereby providing an additional contribution to the ferroelectricity. Such contribution can compensate the chemical pressure and tends to stabilize the tetragonal ferroelectric phase.
In $(Ba_{1-x}Ca_x)(Ti_{1-y}Zr_y)O_3$ systems, Ca off-centering effect also allows to increase the Curie point. It is known that Ba(Ti, Zr)O_3 (BTZ), with Ti^{4+} partially substituted by Zr^{4+}, exhibits very large piezoelectric response and high tunability. Most relevant, is the possibility to shift the orthorhombic or rhombohedral phase to room temperature through setting Zr concentration. The phase diagram of $Ba(Ti_{1-x}Zr_x)O_3$ is shown in figure 2.9. Unfortunately, as Zr concentration increase, the Curie point is shifted toward lower temperature. For compositions of $x > 0.2$ the Curie temperature become lower

[3]For BCT composition of $x = 0.34$ the volume of the unit cell is about 3.6% smaller than that of pure BTO. The same unit cell reduction, if obtained by hidrostatic pressure, would reduce the Curie Point to ~ 180 K. At 5% of reduction of the unit cell volume, ferroelectricity completely disappeared.

[4]First-principles calculations [46] predict a Ca off-centering shift of 0.1 Å, which is larger than the Ti shift of 0.05 Å in pure BTO.

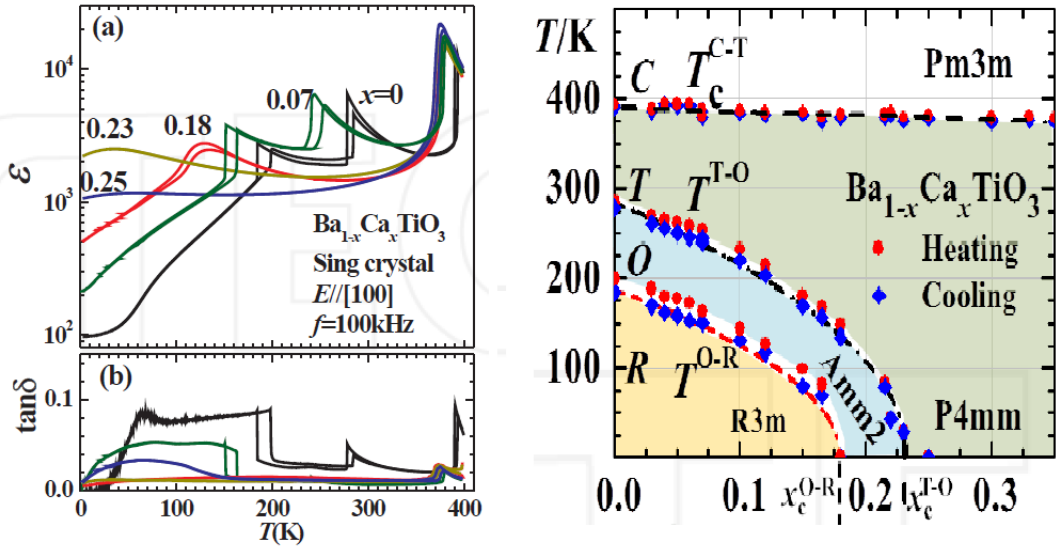

Figure 2.8: Left side: change with temperature of $(Ba_{1-x}Ca_x)TiO_3$ (single crystals) dielectric costant for various concentration of Ca ($0 < x < 0.25$) in the temperature range from 2 K to 400 K. Right side: phase diagram of BCT in the composition range of $x < 0.34$ [45].

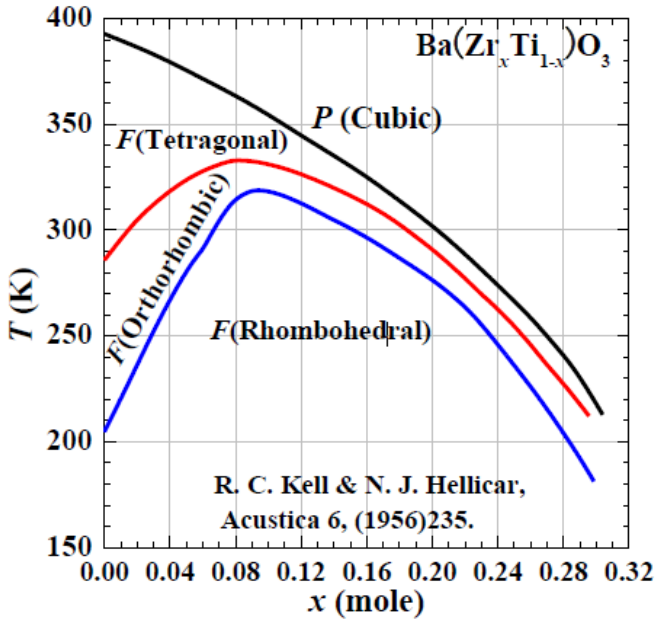

Figure 2.9: Phase diagram of $Ba(Ti_{1-x}Zr_x)O_3$ proposed by Kell and Hellicar [48].

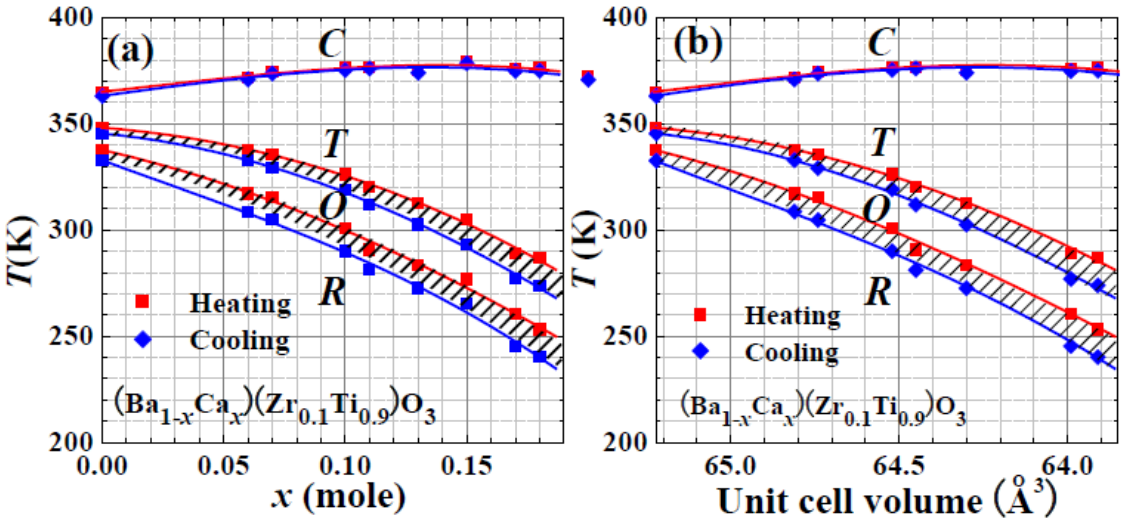

Figure 2.10: Phase diagrams of BCTZ obtained in [47] as a function of (a) Ca concentration and (b) unit cell volume, keeping the Zr concentration constant (y=0.1). The phase transitions exhibit thermal hysteresis. In the cubic-tetragonal transition the thermal hysteresis is less than 2 K.

than room temperature.
In [45] end [47], the effect of partial substitution of Ba by Ca in compositions with Zr concentration of 10 mol%, i.e. in $(Ba_{1-x}Ca_x)(Ti_{0.9}Zr_{0.1})O_3$ systems, is studied. The authors demonstrate, among other things, that the Ca-off centering effect can be used also to increase the Curie temperature of Ba(Zr, Ti)O_3 (see figure 2.10).
Tipically, the Curie temperature is adjusted by partial substitution of Ba with Sr ions. Throught such a substitution the Curie point results shifted (almost linearly) with Sr concentration) towards lower temperature. Then, by setting the Sr concentration, the $Ba_{1-x}Sr_xTiO_3$ ferroelectric transition temperature can be shifted to a temperature that is lower than room temperature [49]. This property is important for application requiring low dielectric loss, which is related whith the paraelectric phase (ferroelectrics tend to has large dielectric loss because of domain wall movement). However, BST properties will be discussed more extensive in the devoted section (2.1.3).

2.1.2 Strontium Titanate - $SrTiO_3$

Strontium Titanate, $Sr^{4+}Ti^{2+}O_3^{2-}$ (abbreviated STO) is an extensively studied material with perovskite structure wich exhibits very interesting properties from both theoretical and applicative point of view. Because of its dielectric properties (if crystalline, STO can reach a relative dielectric constant $k > 300$ at room temperature [40]) STO

is employed in tunable microwave devices [34] and it is a promising candidate as gate insulator in MOSFET and as high-k dielectric for memory capacitors applications [40]. In addition, strontium titanate is used as substrate for different materials, such as high-Tc superconductors and colossal magnetic resistance manganites [50]. Furthermore, if doped with Nb, $SrTiO_3$ exhibits low temperature superconductivity [51].
At room temperature $SrTiO_3$ crystallizes in the cubic perovskite structure with lattice parameter $a = 3.905\,\text{Å}$. The ionic sizes of the atoms, $r(Sr) = 1.44\,\text{Å}$, $r(Ti) = 0.605\,\text{Å}$ and $r(O) = 1.40\,\text{Å}$, return a tolerance factor $t = 1.00$, which is the exact value to form the ideal cubic structure [43].
At about 105 K, STO undergoes a displacement phase transition from cubic to tetragonal symmetry. However, pure STO is not ferroelectric at any temperature: it was shown in 1979 by Müller and Burkard [52] that ferroelectric phase transition is prevented by quantum effects, which are activated at low temperature. This effect is exhibited also by $KTaO_3$ and $CaTiO_3$. The same authors introduced the expression *quantum paraelectric* to indicate such a stabilization of the paraelectric phase. However, since a low concentration of impurities is sufficient to induce ordinary ferroelectric behaviour, we often refer to this compounds with the term *incipient ferroelectrics* [34].
Upon cooling, STO dielectric constant increases according to a Curie-Weiss law $\epsilon = B + C/(T - T_C)$; as the temperature approaching the Curie point of 36 K, ϵ stabilizes at an enormous value exceeding 10^4. Between 4 K and 0.035 K the dielectric constant is independent on temperature (see figure 2.11) [52, 53]. Quantum suppression of the ferroelectric phase appears when the classically calculated ferroelectric displacement Δz of the Ti ion, becomes smaller than the mean value of the quantum fluctuation amplitude $\bar{\Delta} z = \langle \Delta \hat{z}^2 \rangle^{1/2}$. Δz is related to T_C via the formula

$$k_B T_C = \frac{1}{2} \kappa (\Delta z)^2, \tag{2.4}$$

where k_B is the Boltzmann's constant and $\kappa \simeq 5.5 \cdot 10^4$ dyn/cm is a force constant [52, 53]. However, quantum suppression of ferroelectricity is very sensitive to perturbations, such as impurity and strains. In 1971 it was shown [54] that ferroelectric phase transition can be induced in $SrTiO_3$ at the temperature of 4.2 K with the application of $\langle 100 \rangle$ or $\langle 110 \rangle$ uniaxial stress. The sample used in [54] was a $3 \times 3 \times 7$ mm block of pure STO with Al electrodes. The threshold stress for the $\langle 100 \rangle$ and $\langle 110 \rangle$ directions was determined to be 10.1 Kg/mm^2 and 53 Kg/mm^2, respectively.
To establish the occurrence of the phase transition, both dielectric constant anomalies and the hysteresis effect in the polarization curve were observed along a $\langle 100 \rangle$ axis perpendicular to [010], and along a $\langle 110 \rangle$ axis perpendicular to $[0\bar{1}1]$, where [010] and $[0\bar{1}1]$ are the directions of applied stress. Indeed, below the structural transition (~ 105 K), tetragonal domains are formed but they are randomly oriented. As the critical stress is applied, those domains with c-axis parallel to the stress reorient into the plane perpendicular to the stress.

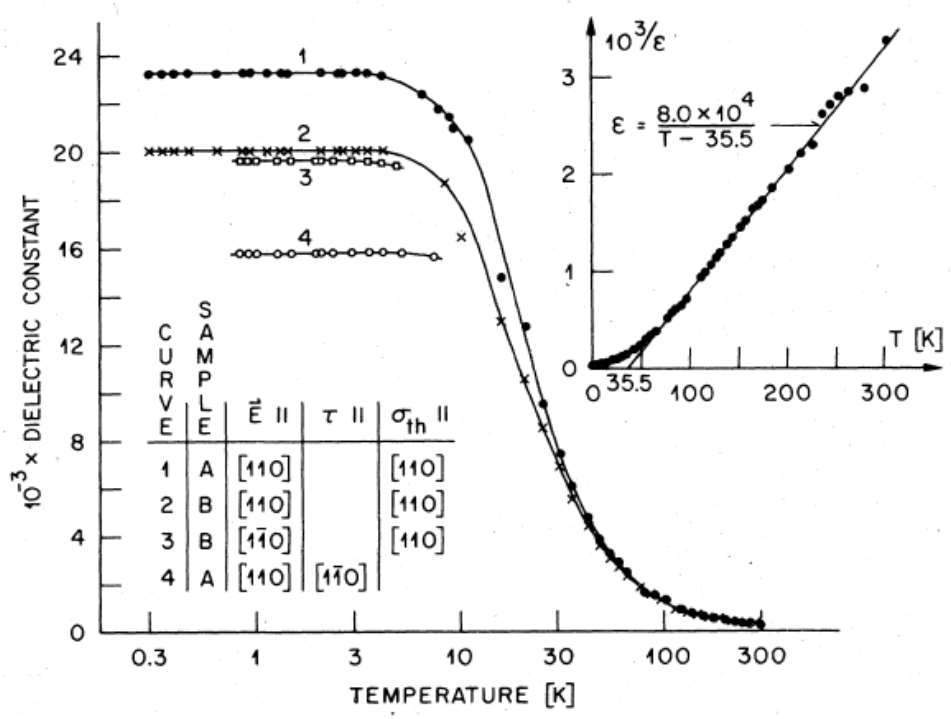

Figure 2.11: Dielectric constants ϵ_{110} and $\epsilon_{1\bar{1}0}$ of two monodomain $SrTiO_3$ samples (A and B) in the temperature range from 0.035 K to 300 K. σ_{th} is the stress applied by thermal treatment and τ is the externally applied stress [52].

The observed behaviour can be looked as a consequence of a general property of perovskites: hydrostatic stress, by reducing the Ti-O spacing, tends to decrease the the transition temperature. By contrast, in the direction perpendicular to a uniaxial stress the Ti-O spacing results increased; the consequent reduction in the restoring force for the Ti ion produces an increase in the transition temperature [54].
The strain dependence of STO properties suggets the possibility of controlling ferroelectricity in epitaxial thin films throught the stress due to the lattice mismach. Different strain states can be produced in strontium titanate, using substrate with a lattice constant that is slighty larger or slighty smaller than that of STO ($a = 3.905$ Å), such as $SrRuO_3$ ($a = 3.93$ Å) or $CaRuO_3$ ($a = 3.85$ Å) [55]. In the past years the effect of stress/strain on ferroelectricity and on the permittivity of $SrTiO_3$ [55] and (Ba,Sr)TiO_3 [56] thin films has been widely investigated. Also theoretical models [57] and first principle calculations [58] were proposed. The expected shift in T_C of (100) $SrTiO_3$ is shown in figure 2.12.

A remarkable result has been reached in [59], where room-temperature ferroelectric-

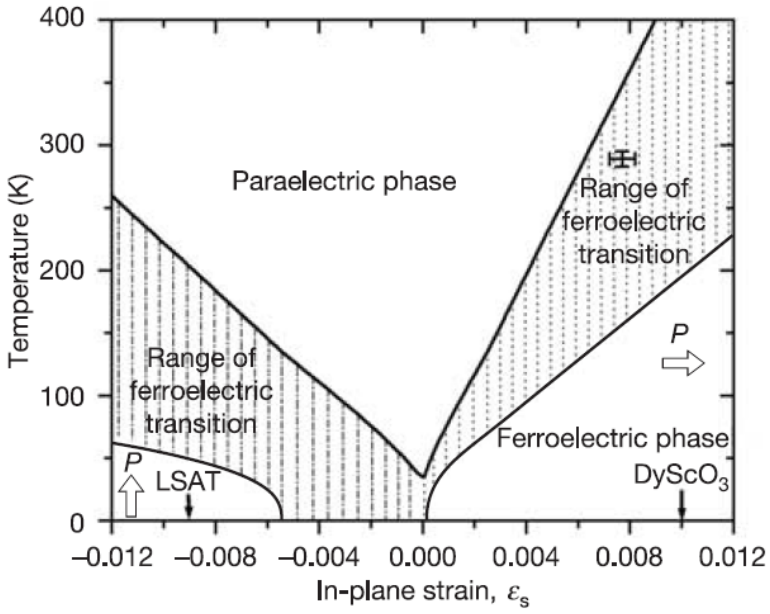

Figure 2.12: Expected shift in T_C of (100) $SrTiO_3$ due to biaxial in-plane strain based on thermodynamic analysis [59]. The strain is defined as $\epsilon_s = (a_{\|} - a)/a$, where a is the lattice parameter of free-standing STO and $a_{\|}$ is the in-plane lattice parameter of the strained STO. The arrows indicate the direction of polarization: tensile biaxial strain causes in-plane polarization, wherease biaxial compressive strain produces out-of-plane polarization. The cross indicate the T_C of a 50 nm $SrTiO_3$ film epitaxially grown on (110) $DyScO_3$ observed in [59].

ity was obtained in $SrTiO_3$ thin film (500 Å-thick) using $DyScO_3$ substrate. Such enhancement in T_C is accompanied by an extraordinary high value of dielectric constant (ϵ_r is nearly 7000 at 10 GHz, room temperature). $DyScO_3$ is orthorhombic with lattice consant $a = 5.440$ Å, $b = 5.713$ Å and $c = 7.887$ Å. (100) $SrTiO_3$ can be grown on the (110) $DyScO_3$, that has an in-plane lattice spacing of 3.944 Å. The tensile lattice mismach of +1.0% at 25°C produces a compression in the out-of-plane lattice constant, $a_\perp = 3.8785 \pm 0.0005$ Å, and an elongation in the in-plane lattice constant, $a_\parallel = 3.935 \pm 0.002$ Å. The lattice constants $a_\parallel$ and $a_\perp$ were determined in [59] with high-resolution X-ray diffraction measurements. The in-plane relative dielectric constant as a function of temperature for the 500 Å $SrTiO_3/DyScO_3$ film is shown in figure 2.13. The simultaneous peaks in ϵ_r and $\tan\delta$ indicate that the Curie temperature is about 293 K. The achievement of such remarkable dielectric properties is related to the ability to obtain uniformly biaxial strained films, so avoiding dislocations that causes undesiderable relaxations. Because of its low mismach with $SrTiO_3$, $DyScO_3$ has been proved to be a suitable substrate material for this purpose.

2.1.3 Barium Strontium Titanate - (Ba,Sr)TiO_3

Another well characterized BTO based material is barium strontium titanate $Ba_{1-x}Sr_xTiO_3$ (BST). The high dielectric constant and low leakage current of this material make BST thin films very attractive as capacitors for dynamic random access memory (DRAM). Because of its high electric field dielectric tunability and relatively low loss tangent at microwave frequencies, BST is also a potential candidate for tunable microwave devices, such as tunable filters and phase shifters [43, 60].
Partial substitution of Ba ions by Sr ions causes the shift of the curie point throught lower temperature. The decrease of T_c is almost linear with Sr concentration, from about 400 K for pure $BaTiO_3$ ($x = 0$) to 40 K for $x = 0.95$ [49]. So, at room temperature the system is in the ferroelectric phase when Sr content is in a range from 0 to 0.3, and in a paraelectric phase when Sr content is in a range from 0.3 to 1. Strontium titanate $SrTiO_3$ may be considered as the $x = 1$ limit case, with a Curie point very close to 0 K [61].
In general, ferroelectric materials exhibit high dielectric loss because of domain wall movement. So, for microwave applications, it can be very helpful to have a material whith high dielectric constant which is paraelectric at room temperature: (Ba,Sr)TiO_3 has dielectric loss $\delta < 0.001$ at microwave frequencies, but maintains large permittivity. Anyway, it is important to take into account the main differences between the bulk and the thin films properties: in thin films the dielectric constant and the tunability are lower than that of the bulk, while the dielectric loss tend to be higher [62].
Contrary to what appens in (Ba,Ca)TiO_3, the reduction of the lattice constant accompanying the lowering of T_c is nearly the same if the lowering was obtained by hidrostatic pressure [61].

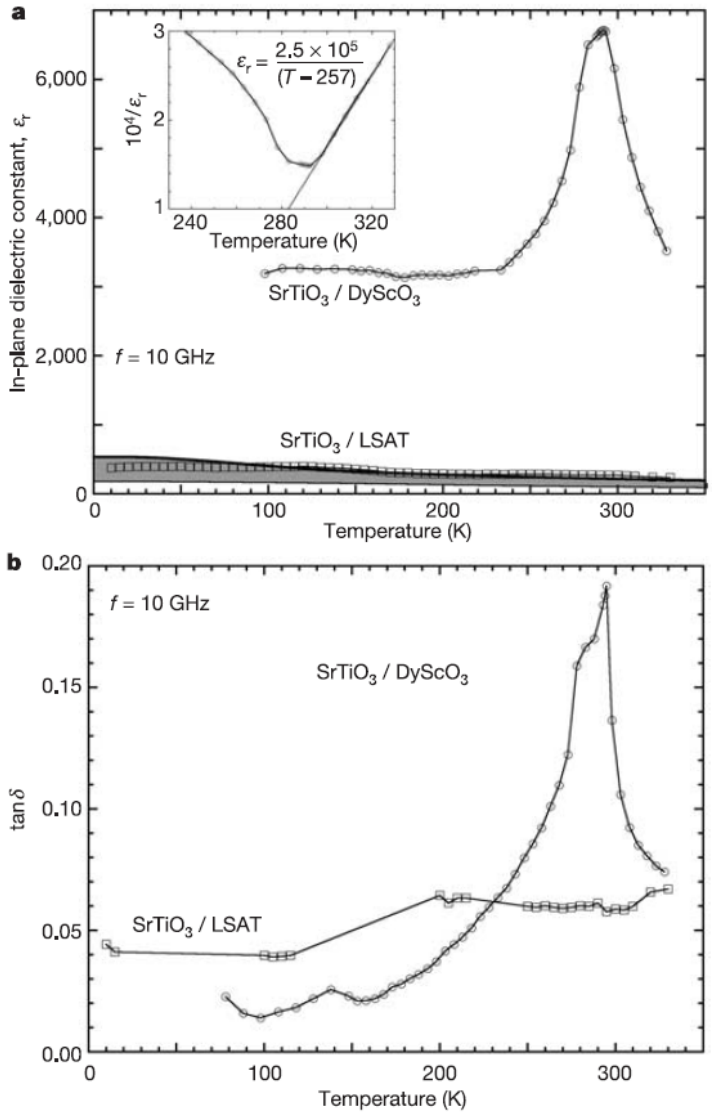

Figure 2.13: (a) In-plane relative dielectric constant and (b) dielectric loss (tanδ) for 500 Å-thick $SrTiO_3$/(110)$DtScO_3$ epitaxial film as a function of temperature, measured at 10 GHz. For comparison, the behaviour of 500 Å-thick $SrTiO_3$/(100)LSAT epitaxial film is shown [59].

As said before, one of the best features of barium strontium titanate is represented by the strong electric field depedence of its dielectric permittivity. In general, the dielectric constant has its maximum value at zero bias voltage and it decreases as the field increases. Tunability is commonly define as follows:

$$\text{Tunability} = \frac{\epsilon_{r(0)} - \epsilon_{r(bias)}}{\epsilon_{r(0)}} \tag{2.5}$$

where $\epsilon_{r(0)}$ is the dielectric constant at zero bias and $\epsilon_{r(bias)}$ is the dielectric constant at a defined field. However, other definitions are frequently used; since in most applications and experiments BST films constitutes the dielectric component of capacitors, and since the capacitance is the measured physical quantity, the definition $(C_{(0)} - C_{(bias)})/C_{(0)}$ is often adopted.
In [63] the dielectric properties and the permittivity field dependence of $Ba_{0.24}Sr_{0.76}TiO_3$ thin film were investigated. In this study, BST thin film (229 nm) was epitaxially grown on a Pt/MgO (100) substrate by rf magnetron sputtering. The top electrode was made of Ni. The authors found that the thin film had a dielectric constant of 1400 at zero bias voltage, which rapidly decrease when bias field is applied.
The dielectric constant as a function of bias electric field is shown in figure 2.14. It is also shown, for comparison, the dielectric constant behaviour of an STO thin film produced in the same study [5]. In both cases the maximum value of dielectric constant is reached at zero bias voltage, but BST sample exhibits a maximum value (1400) that is about 4 times larger than that of STO (360). However, it is sufficient to apply an electric field of 20 MV/m to obtain a value smaller than that of STO sample. The decrease in the dielectric constant under bias field dielectric application may be explained by the polarization saturation of the BST film (see figure 2.15).
Figure 2.15 shows the bias dependence of ϵ_r for some BST thin films of various compositions and its hysteresis curves, obtained in [64] by the same authors of [63]. The film with Ba content of 0.24 had the highest dielectric constant, the largest tunability and it doesn't exhibit hysteresis.
Hysteresis appears at Ba content $1 - x = 0.44$ (then, with Sr concentration of 0.56), although it is known that for this composition bulk BST crystals are in the paraelectric phase at room temperature. In thin films the Curie point is shifted towards higher temperature than that of the bulk and films with Ba content $1 - x > 0.44$ are in the ferroelectric phase at room temperature. The induced ferroelectricity is explained by the authors as a result of the elongation of the lattice constant in the thickness direction

[5] The dielectric constant ϵ_r was calculated from the measured capacitance C using the formula

$$\epsilon_r = \frac{Ct}{\epsilon_0 A}$$

where ϵ_0 is the vacuum permittivity, t is the film thickness ($\sim$ 230 nm) and A the area of the top electrode (0.1×0.1 mm). The bias field E_b was assumed uniform: $E_b = V_b/t$.

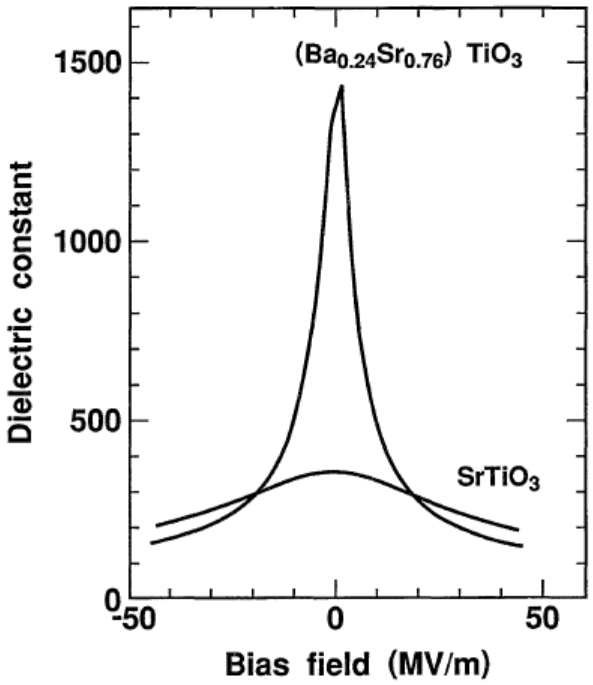

Figure 2.14: Dielectric constant as a function of bias electric field for $Ba_{0.24}Sr_{0.76}TiO_3$ (229 nm) and STO (224 nm) thin films. The measurements were performed at 100 kHz with an amplitude of 0.1 V, at room temperature [63].

[64].
As said before, the dielectric constant of BST thin films is lower than that of the bulk, which is known to be more than 5000 [64]. Such a reduction is intensified in polycrystalline films, in which a central role is played not only by particle sizes, but also by interfacial effects.
In [65] some $Ba_{0.7}Sr_{0.3}TiO_3$ polycrystalline thin films of different thickness (in the range from 24 to 160 nm) were deposited on Pt coated wafers by a chemical vapor deposition tecnique. Also the top electrode was made of Pt. For a bulk crystal of this composition it would be expected a Curie point of about 300 K. The BST films turned out to be strongly 100 textured with a minor 110-oriented component.
The capacitance per unit area (capacitance density) as a function of DC bias voltage of the samples is shown in figure 2.16. Once again, the dielectric constan reaches its maximum value near zero bias field and it decreases as the field increases. Moreover, the permittivity decreases with thickness near zero bias field and becomes almost thickness independent at higher fields.
Particularly interesting is the temperature dependence of the inverse maximum capacitance density (at zero bias) as a function of the thickness. As we can see in figure 2.17, the data for each temperature (25, 100, 150 and 200°C) lie on a straight line; the slope of the line results strongly dependent on the temperature, whereas the intercept is almost independent on temperature. Such a behaviour is attributed to the series capacitance formed by a constant-valued capacitance (represented by the nonzero intercept)

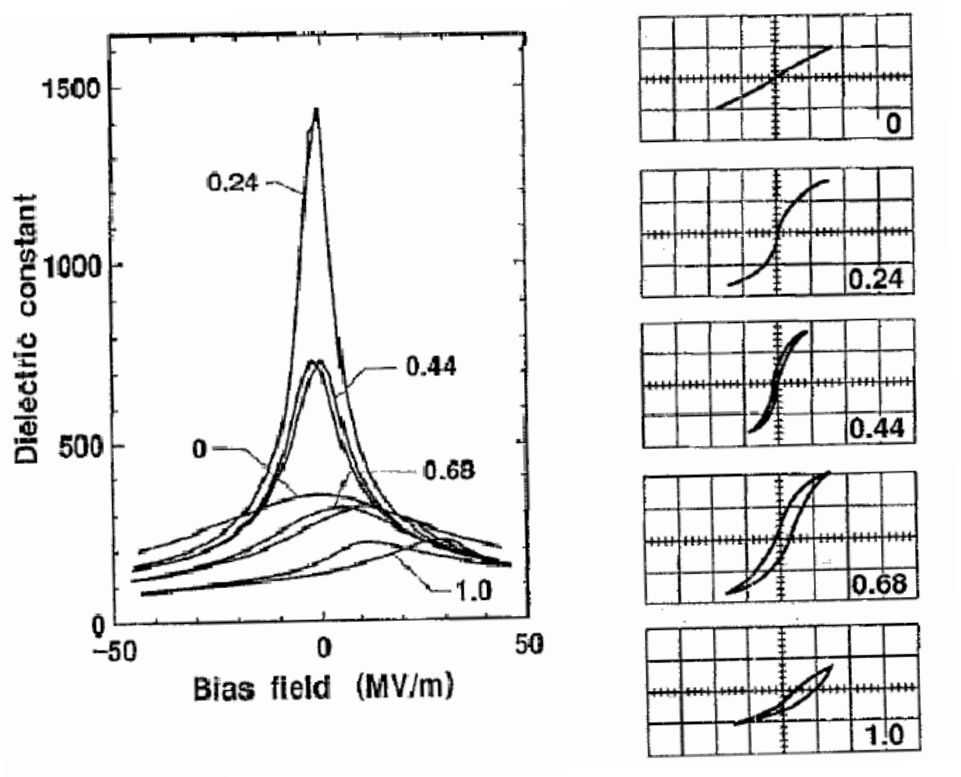

Figure 2.15: Left: Dielectric constant of BST films as a function of bias electric field for various concentration of Ba ions. The measurements were performed at 100 kHz with an amplitude of 0.1 V, at room temperature. Right: D-E hysteresis curves of BST thin films measured at 5 kHz, room temperature. x:22 MV/m, y:0.11 C/m^2. The thickness of the thin films is from 219 to 232 nm [64].

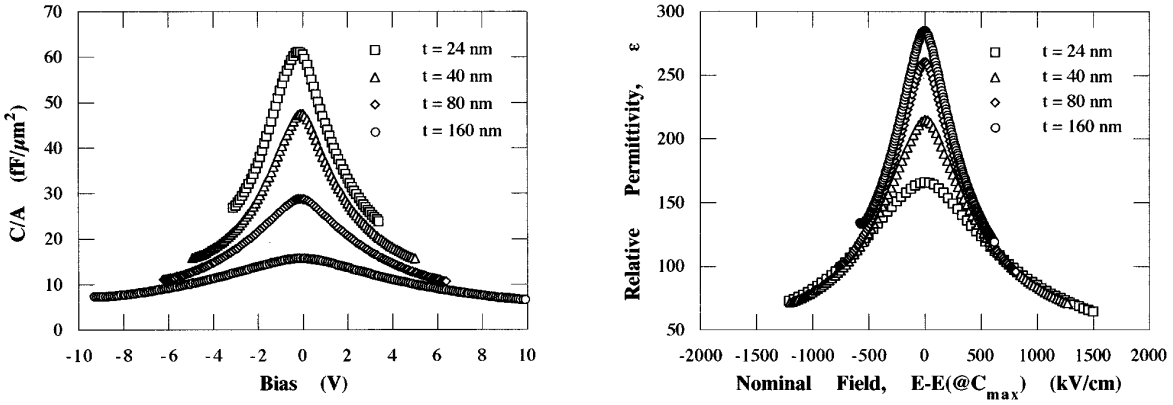

Figure 2.16: Left: capacitance density as a function of applied DC bias voltage for Pt/BST/Pt/SiO_2Si capacitors with BST film thickness of 24, 40, 80 and 160 nm measured in [65]. Right: dielectric constant vs DC electric field of the same samples calculated from the C-V data.

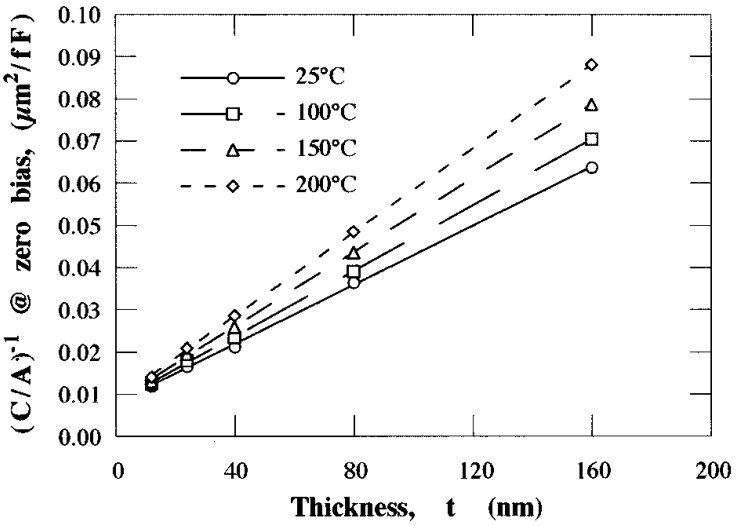

Figure 2.17: Inverse of zero bias capacitance density as a function of BST thickness at temperatures of 25, 100, 150 and 200°C. In addition to the thicknesses of figure 2.16 (24, 40, 80 and 160 nm), a sample of 12 nm thick is included [65].

and a thickness-dependent capacitance. Then, for a BST thin film capacitor, the capacitance dansity is no longer related to the dielectric constant via the well known formula $C/A = \epsilon_0\epsilon_r/t$, but it is needed an interfacial capacitance model described by the equation

$$\frac{A}{C} = \frac{A}{C_i} + \frac{A}{C_B} = \frac{t_i}{\epsilon_0\epsilon_i} + \frac{t - t_i}{\epsilon_0\epsilon_B}, \tag{2.6}$$

where C_i is the interfacial capacitance, C_B is the bulk film capacitance, ϵ_i is the interfacial layer permittivity and t_i is the interfacial layer thickness [65]. The interfacial capacitance may be thought as formed by a low dielectric constant layer at the top (C_{Ti}) and at the bottom (C_{Bi}) interface.
We conclude that interfacial effects can affect the dielectric properties of BST thin films. The ability to reduce the interfacial capacitance represents a fundamental step to achieve high dielectric constant capacitors.

2.2 Manganites and Colossal Magnetoresistance

The manganese oxides, of general formula $RE_{1-x}M_xMnO_3$, where RE is a rare earth and M = Ca, Sr, Ba, Pb, have remarkable interralated structural, magnetic and transport properties. This complexity is related to the mixed valence (3^+ or 4^+) of the Mn ions. Among the various features of manganites, most relevant are the very large negative magnetoresistance, called colossal magnetoresistance (CMR), exhibited in the vicinity of metal-insulator for some compositions and the fully spin-polarized conduction band in the metallic phase [66].
Of particular interest are the mixed-valence perovskites $La_{1-x}M_xMnO_3$, with M = Ca, Sr, Ba, which show ferromagnetic metallic behavour for composition of about $x = 1/3$, as a result of the double-exchange (DE) interaction.

Crystallography and Electronic Structure The $RE_{1-x}M_xMnO_3$ oxides are complex compounds with the perovskite structure. Each A site can be occupied by a trivalet RE ion or by a divalent M ion, so determining the valence state of the Mn ions located at the B sites (see figure 2.18). In stoichiometric oxides, the proportion between Mn^{4+} and Mn^{3+} is x and $1 - x$, respectively. The tolerance factor of manganites is about 1, resulting in a structure close to the cubic perovskite. However, at low temperature, manganites have a lower rhombohedral or orthorhombic symmetry.
The electronic structure of manganites is governed by the 3d orbitals of the Mn ions, located at the center of the MnO_6 octahedra. The electronic configurations of isolated Mn^{4+} and Mn^{3+} ions are $3d^3$ and $3d^4$ respectively. In cubic crystals the five d-orbitals are split into three t_{2g} orbitals and two e_g orbitals (see figure 2.19). The first Hund's rule imposes parallel alignment of the electrons spins, than the Mn^{4+} ions are $t_{2g}^{3\uparrow}$ with

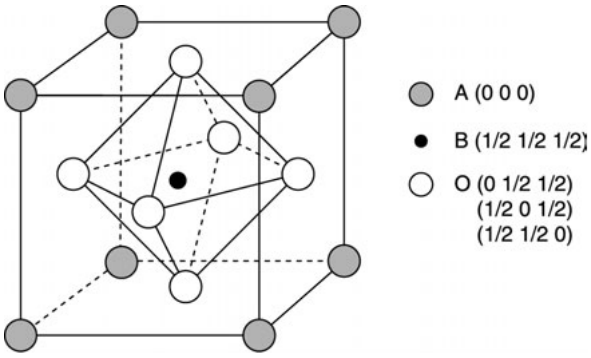

Figure 2.18: Schematic representation of the cubic perovskite structure [66].

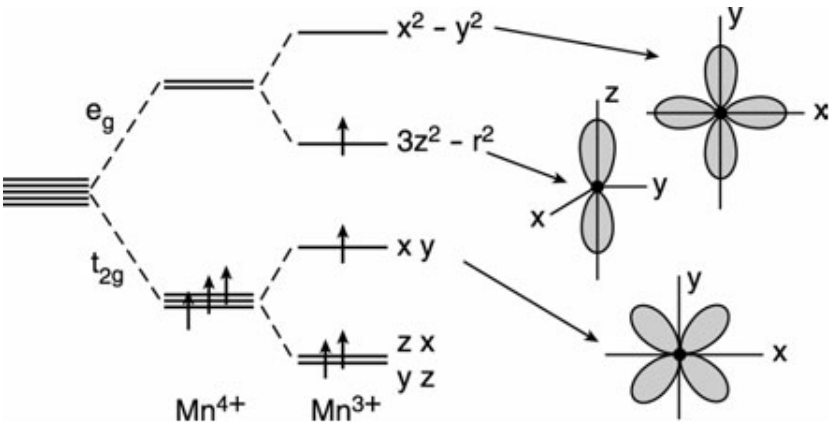

Figure 2.19: Energy levels of Mn^{4+} and Mn^{3+} in a crystal field of octahedral symmetry [66].

$S = 3/2$, and Mn^{3+} are $t_{2g}^{3\uparrow}e_g^{\uparrow}$, with $S = 2$. Their respective magnetic moments are $3\mu_B$ and $4\mu_B$.
As a consequence of the Jahn-Teller effect (previously described in this chapter) activated by the Mn^{3+} ions, the degeneracy of the e_g and t_{2g} level is removed by the distortion (axial elongation) of the MnO_6 octahedra. This distortion is due to the odd number of electrons in the e_g orbitals and lead to a reduction in the energy of the Mn^{3+} ions. Than, Jahn-Teller distortion will mainly affect the lightly doped manganites, with a low concentration x of Mn^{4+} and an high concentrations $1 - x$ of Mn^{3+} ions [66].

Magnetic Properties and Electrical Conductivity The magnetic properties of manganites are governed by the exchange interaction between the Mn ions spins. The spins of Mn ions with the same valence interact each other via superexchange interac-

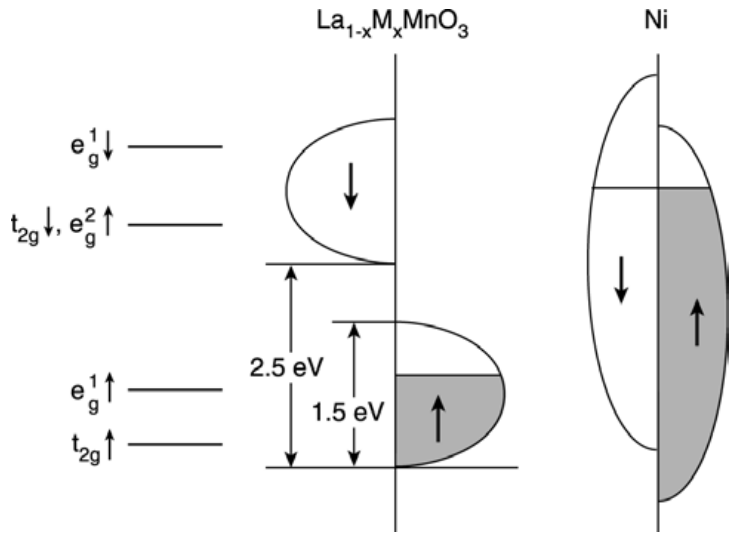

Figure 2.20: Comparison of the band structures (schematic view) of ferromagnetic-doped $LaMnO_3$ and Ni. The value of the energy and the filling of the bands corresponds to $La_{2/3}Sr_{1/3}MnO_3$. On left are represented the energy levels for an isolated Mn ion in an octahedral crystal field [66].

tion; Mn^{4+}-O-Mn^{4+} coupling is antiferromagnetic (AF), whereas the Mn^{3+}-O-Mn^{3+} can be both ferromagnetic (F) or AF.
In the case of Mn^{3+}-O-Mn^{4+} interaction, Mn ions can exchange their valence by a simultaneous jump of the e_g electron of Mn^{3+} on the O p-orbital, and from the O p-orbital to the empty e_g orbital of Mn^{4+}. This *double exchange* (DE) mechanism leads to a ferromagnetic coupling, with a dependence of $\cos(\theta/2)$, where θ is the angle between the Mn spins, instead of the $\cos\theta$ behaviour of the usual exchange interaction.
In first approximation, the ferromagnetism of manganites is a result of the competition between Mn^{4+}-Mn^{4+} AF superexchange and Mn^{3+}-Mn^{4+} F DE interaction. We can neglect Mn^{3+}-Mn^{3+} interaction since both F and AF coupling coexist. The ferromagnetic metallic phase (FM) with the highest Curie temperature T_C is obtained for $x \sim 1/3$.
DE interaction is also at the basis of electric conduction in manganites. Indeed, for a doping concentration of about $x = 1/3$, the e_g electrons become delocalized in the ferromagnetic phase. The most interesting aspect concerning the electronic structure is the full spin-polarization of the conduction band; as shown in figure 2.20 the spin up and spin down bands are separated by 1 eV or more, the upper band is empty and the lower band is only partially filled. This half metallic behaviour is very attractive for spintronics, indeed $La_{1-x}Sr_xMnO_3$ (LSMO) with $x \sim 1/3$ is commonly used as spin analyzer in spin-valve based device (see sections 1.2 and 1.4).

The manganites with $x < 0.5$ have a conduction band more than half-filled, so the

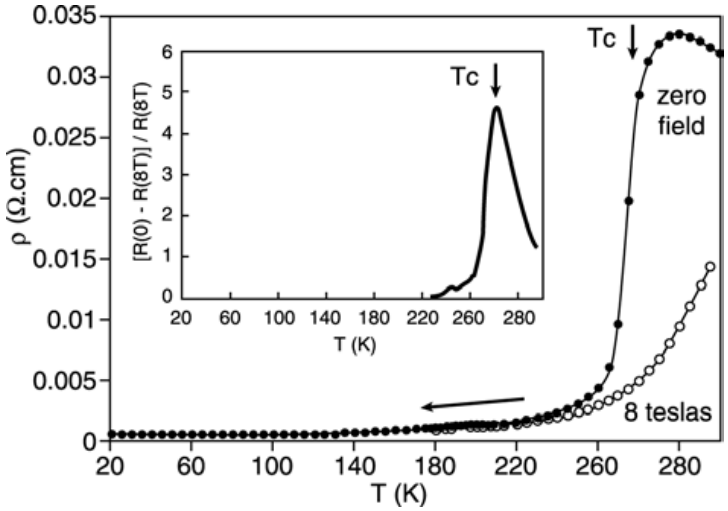

Figure 2.21: Resistivity versus temperature in zero field and in a 8 T applied field for an $La_{0.825}Sr_{0.175}MnO_3$ single crystal. In inset is shown the CMR ratio versus temperature [66].

charge carriers are holes, and we talk about hole-doped manganites. By contrast, manganites with $x > 0.5$ have a conduction band less than half-filled and they are labelled electron-doped manganites.

Metal-Insulator Transition and CMR Above the Curie temperature, manganites are in a paramagnetic insulating phase, in wich the electrical resistivity is strongly dependent on temperature. In this phase many mechanisms contributes simultaneously to the behaviour of $\rho(T)$ [66].
At low T, manganites with strong DE interaction, such as LSMO with $x \sim 1/3$, exhibit a transition to a low resistivity FM phase with $\rho \sim \rho_0 + aT^2$ for $T \ll T_C$. The alignment of the Mn spins, which is typical of the ferromagnetic phase, can be induced also for $T \geq T_C$ (or increased for $T \leq T_C$), by applying an external magnetic field. This inverse magnetoresistance is called *colossal magnetoresistance* (CMR). As shown in figure 2.21 the maximum effect is reached close to T_C. In addition, the CMR is larger and larger as T_C is smaller and smaller.

In general the CMR of mixed-valence manganites requires large applied magnetic fields, typically a few teslas. An exception is represented by polycrystalline samples of $La_{1-x}M_xMnO_3$ with M = Ca, Sr, Ba, Pb, such as $La_{0.7}Ca_{0.3}MnO_3$ [67], which shows a low field negative magnetoresistance (LFMR). This LFMR is related to the strong spin-dependent scattering at the grain boundaries, which leads to a high zero-field resistivity. Since the ferromagnetic domains, which are defined by the grains of the sample, are decoupled, they result randomly oriented when no magnetic field is applied and they

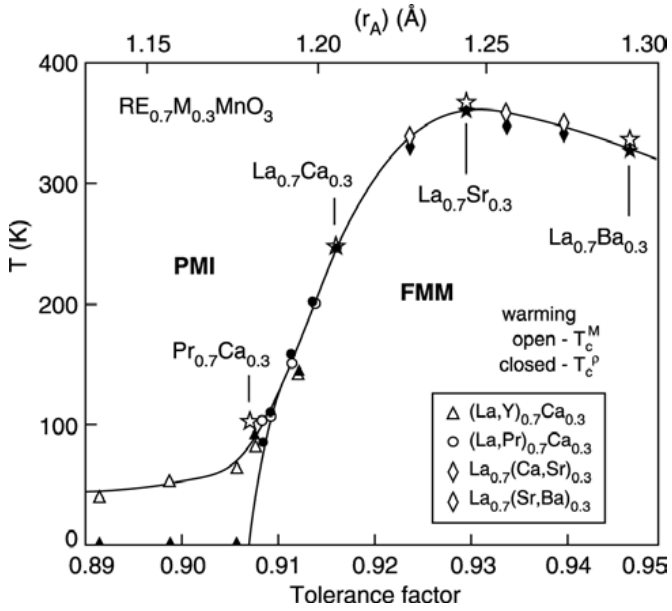

Figure 2.22: Phase diagram of temperature versus tolerance factor and average size of A ions for $RE_{0.7}A_{0.3}MnO_3$ [66].

can be easily aligned in a parallel configuration by a low external magnetic field [68]. LFMR tipically occurs in the range $0-0.1\,\mathrm{T}$, and increases with decreasing temperature and particle size.

$La_{1-x}Sr_xMnO_3$ The main parameters governing the physical properties of manganites are the doping level x and the average size $\langle r_A\rangle$ of the cation in the A site. DE effect is maximum around $x = 1/3$ and $\langle r_A\rangle = 1.24\,\text{Å}$ [66] (see figure 2.22).
The most ferromagnetic manganite is $La_{1-x}Sr_xMnO_3$. For $x \sim 1/3$ it reaches the highest Curie temperature $T_C = 370\,\mathrm{K}$. The phase diagram and the behaviour of resistivity as a function of temperature are shown in figure 2.23. For $x = 0$ we have orthorhombic $LaMnO_3$, which is an AF insulator with a Néel temperature $T_N = 140\,\mathrm{K}$. Ferromagnetic insulating phase can be obtained in LSMO at low doping level, from about $x = 0.1$. This phase becomes metallic (FM) for $x > 0.15$, as shown by the behaviour of $\rho(T)$ (see figure 2.23, right).

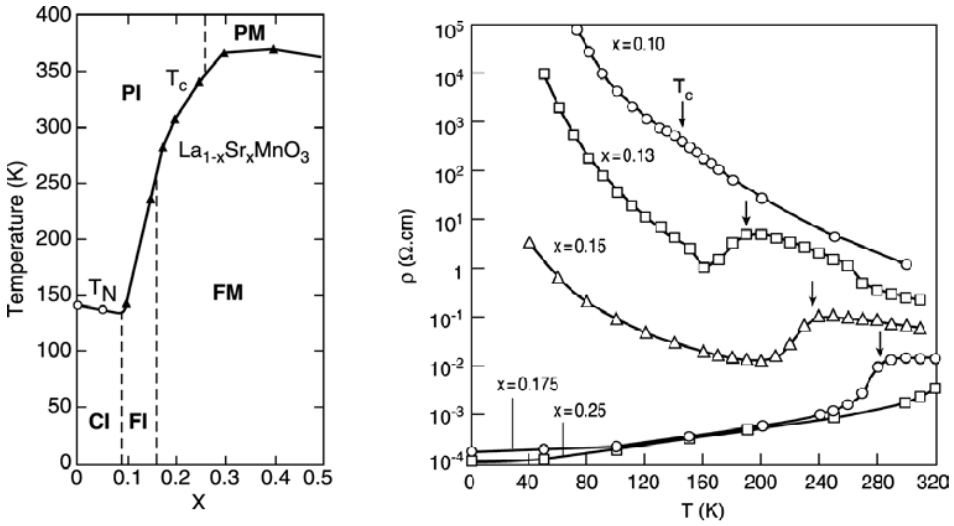

Figure 2.23: Left: transition temperature of $La_{1-x}Sr_xMnO_3$ versus Sr concentration. CI, FI and PI stand for insulating canted, ferromagnetic insulator and paramagnetic insulator respectively. PM and FM means paramagnetic metal and ferromagnetic metal, respectively. T_N is the Néel temperature. Right: Resistivity as a function of temperature for $La_{1-x}Sr_xMnO_3$ single crystals of different composition [66].

Chapter 3

Growth Methods and Experimental Tecniques

All the thin films growed and investigated in this thesis has been deposited by a pulsed electron beam ablation technique, and characterized using various methods. In this chapter we briefly describe the channel spark system and some experimental techniques, such as the X-ray photoelectron spectroscopy (XPS) and the X-ray diffraction (XRD).

3.1 The Channel Spark Ablation (CSA)

This deposition technique belongs to the pulsed electron deposition methods and allows to produce high quality stoichiometric thin films of simple oxides, complex oxides and manganites [69]. This method is based on the ablation of a stoichiometric target by means of pulsed ($\sim 100\,\mathrm{ns}$) electron beams with high energy density ($\sim 10\,\mathrm{J/cm^2}$), which is related to the formation of a plasma in a low pressure ($\sim 10^{-2}\,\mathrm{mbar}$) gas.
A schematic view of the channel spark system is shown in figure 3.1. A negative high voltage ($5-30\,\mathrm{kV}$) power supply is applied to a hollow cathode (-HV) which is separated from the grounded chamber by a dielectric channel that acts as an accelerator for the electrons. The hollow cathode is separated to the grounded chamber floor by the parallel of a capacitor and dielectric channel, which gives the name, and is separated from ground by a charging resistor ($\sim 100\,\mathrm{M\Omega}$) and an air gap having a floating electrode. Between the latter and the charging resistor a triggering anode plate is connected and inserted the glass bulb. At a sufficient high voltage a spark brakes down the air gap. The resulting sharp change in the potential difference between the hollow cathode and the anode plate, ionizes the molecules in the bulb triggering plasma in the cathode cavity, where the electron component of the plasma is amplified thanks to the electrons coming from the capacitors. The electrons are accelerated from the potential difference between the H. C. and the grounded chamber floor towards the target, which is also grounded,

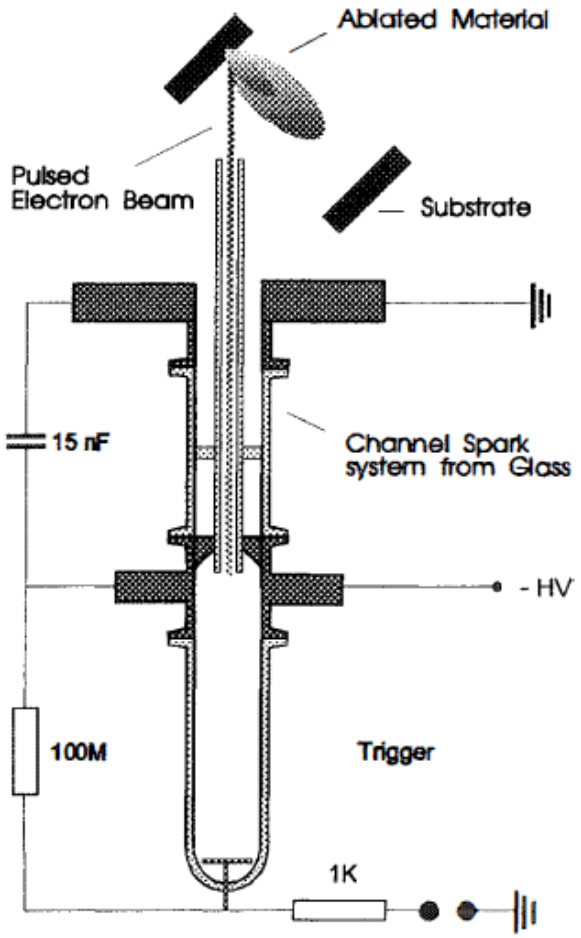

Figure 3.1: Scheme of the channel spark ablation system. [70].

and a self-pinched electron beam is formed. The accelerated electron beam propegates along the dielectric channel, whose inner walls take part to the ionization processes. Because of the high resistance of the charging resistor, the capacitor discharge occours throught the low resistance electron beam in the pyrex channel. Moreover, the beam is further amplified by secondary emission from the channel wall. The pulsed behaviour of the beam is due to the fact that the beam cannot be sustained and the discharge extinguishes up to the new spark in the air gap [69].
The interaction of the pulsed electron beams with the target produces the vaporization of a small amount of material. As a result, a plasma with the shape of a "plume" is formed and propagates towards the substrate surface, where it condenses, so forming a thin film.
The energy distribution of the electrons in the beam and the duration of the pulse depend

on the accelerating voltage and on the gas pressure. For a fixed voltage threshold, the charging time and, hence, the operating frequency, depends on the current supplied to charge the capacitor. Typical frequency values start from 1 to 10 Hz. The beam results stable for a gas pressure of about 10^{-2} mbar. The gas, oxygen in our case, is introduced in the chamber after the achievement of a preliminary vacuum of $10^{-5} - 10^{-6}$ mbar.
Another important parameter for epitaxial growth of thin films is represented by the substrate temperature; the sample holder can be heated up to 1000°C or more using Joule effect.
Some views of the CSA used for the fabrication of the samples described in this thesis are shown in figure 3.2, and 3.3.

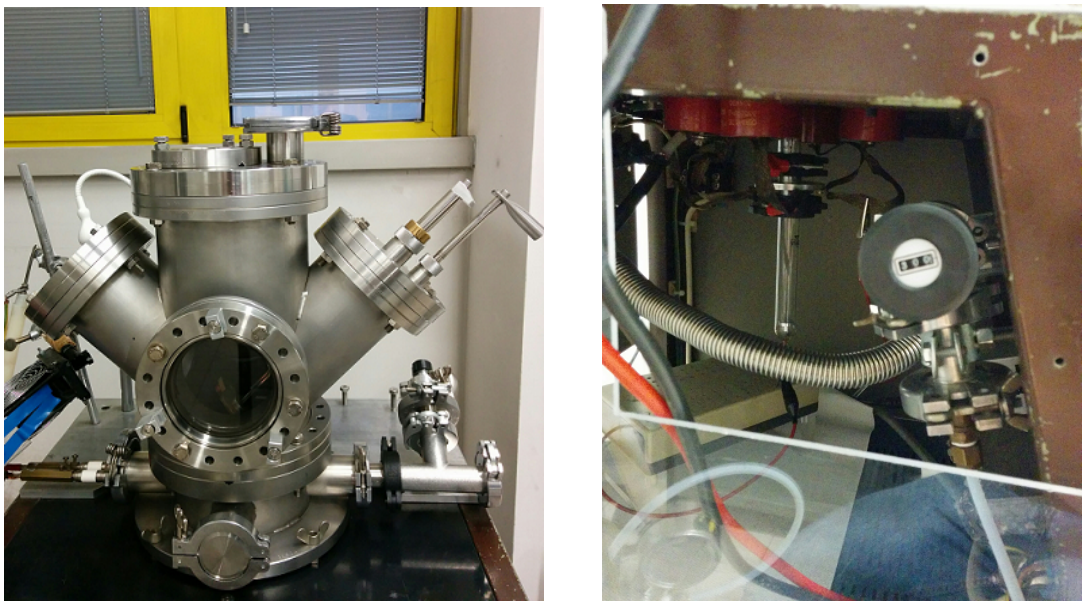

Figure 3.2: Left: upper part of the CSA system. Right: lower part of the CSA systems. From this view we can see the four capacitors (in red), the pyrex bulb and the O_2 needle valve.

3.2 X-Ray Photoemission Spectroscopy - XPS

XPS is a very useful method to investigate a wide range of materials, based on the measure of the photoelectrons ejected as a consequence of the interaction of an X-ray beam with a sample, in order to obtain informations on its chemical composition. Due to a depth of analysis of about 3 nm, XPS is mainly adopted for the characterisation of thin films and the surface regions of materials. The kinetic energy E_k of a photoelectron depends on the energy of the incident photon $h\nu$, on the binding energy E_B and on the

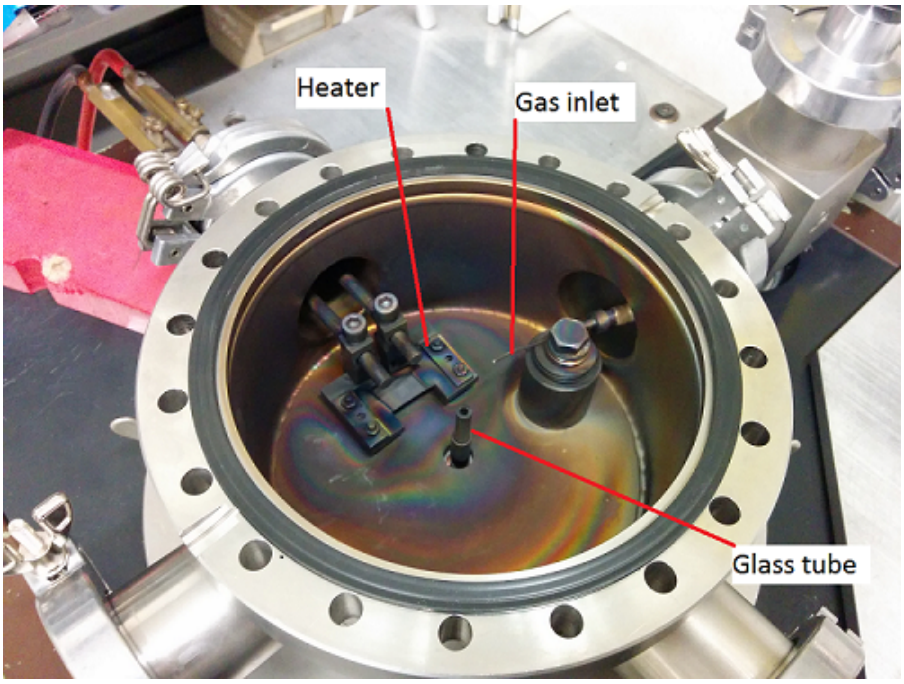

Figure 3.3: Top view of the CSA sytsem (open chamber).

work function of ϕ. Thus

$$E_k = h\nu - E_B - \phi - \delta E, \tag{3.1}$$

where δE is an additional term that takes into account the reduction of the kinetic energy due to electrostatic charging in case of XPS applicated to an insulator. The binding energy is the main quantity determined with XPS, providing informations on theelements present in the sample.
To perform a quantitative analysis of the peaks it is needed to remove the various background contributions and decompose the different spectral structures. The intensity of these structures can be used to estimate the chemical composition of the sample. The concentration of an element in an homogeneus sample can be estimated considering the intensity (peak area) I of all the structures:

$$c_x = \frac{n_x}{\sum_i n_i} = \frac{I_x/S_x}{\sum_i I_i/S_i}, \tag{3.2}$$

where n is the atomic density of an element and S is the *sensitivity factor* which depends both on the considered element and on the apparatus. It includes the cross section σ for the photoelectron production for a certain orbital, the photon flux J, the analyser efficiency K for a certain energy and the electron attenuation length λ.

An XPS spectrum is obtained irradiating a sample with a monocromatic X-ray beam generated by an X-ray lamp. Tipically the K_α line of Mg or Al are used (1253.6 and 1486.6 eV, respectively). Alternatively, synchrotron radiation can be used, given its high monochromaticity, intensity and frequency tunability. An example of XPS spectrum is shown in figure 3.4

The primary structure of an XPS specrum consists of the core level peaks, the valence

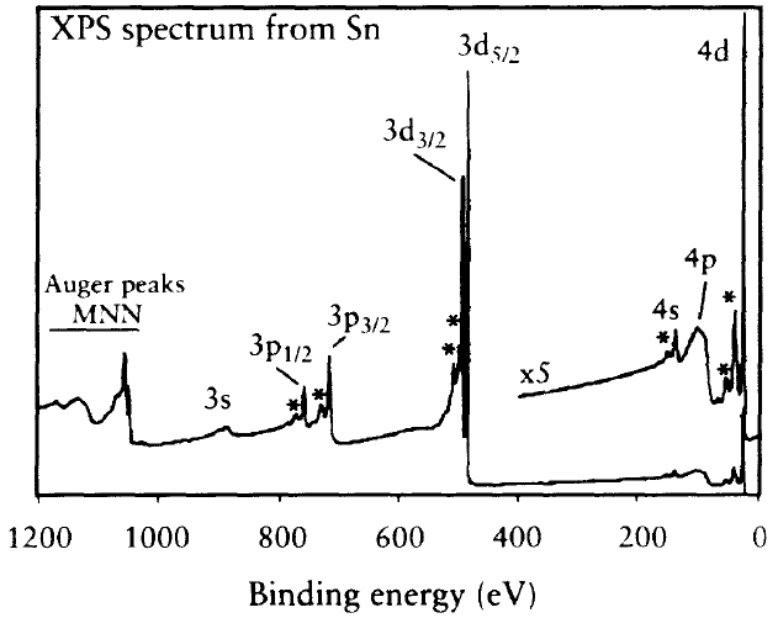

Figure 3.4: Spectrum of Sn obtained using K_α line of Al. The asterisks indicates the electron energy loss features due to plasmon excitation [71].

band spectrum and the Auger electrons peaks. These three contributions are superimposed on a background of inelastically scattered electrons.

The binding energy represents an intrinsic property of an element and can be only slightly modified by the chemical environment of the atom. The core levels provide sharp peaks clearly distinguishable from the background. Many peaks are doublets because of spin-orbit interaction: the splitting ΔE_j, with $j = l + 1/2, l - 1/2$, consists of some eV, increases with the atomic number Z (for given quantum numbers n and l) For a given atom it decrease both with increasing n and with increasing l. The relative intensity of each doublets is given by the ratio of their relative degeneracy $2j + 1$. For instance, if we consider electrons from a d orbital, the $d_{3/2}$ and $d_{5/2}$ peaks intensity will have a fixed ratio of 2/3. In general, the main factor that determines the peaks intensity is the photoionization cross section σ.

The broadness of the observed peaks, i.e. the spectral resolution ΔE, is a convolution

of three factors: the linewidth of the exciting radiation ΔE_X, the analyer resolution ΔE_A, and the intrinsic width of the core level ΔE_{NAT}. The latter term is governed by the lifetime τ of the final state (hole) of about 10^{-15} s ($\Delta E_{NAT} \sim h/\tau$). Assuming a gaussian shape of the peaks, the relationship between these terms is

$$\Delta E = \sqrt{\Delta E_X^2 + \Delta E_A^2 + \Delta E_{NAT}^2} \tag{3.3}$$

However, the spectral resolution ΔE is tipically dominated by the ΔE_X term.
Several factors can produce slight shift in the core levels, such as the oxidation state, the molecular environment or a different position in a crystal lattice. These effects doesn't compromise the identification of a chemical species, but can be exploited to extract informations on the chemical state of an element in the sample.
An apparatus for the measurements of photoemission spectra is quite complex. The main constituents of an electron spectrometry are an X-ray source, a sample holder, an electron analyser and a detector. All these components are positioned into a vacuum chamber, where ultra-high vacuum (from 10^{-8} to 10^{-10} mbar) is obtained using an appropriate vacuum system [71]. An XPS system may consist of a singlechamber, but usually there is an auxiliary chamber, which is connected to the main one through a valve, used for the introduction of the specimen preserving the vacuum.
The energy of the photoemitted electrons is measured using an electron analyser. The two existing types of analyser are the cylindrical mirror analyser (CMA) and the hemispherical sector analyser (HSA). The CMA consists of two concentric cylinders held at a different potential (see figure 3.5). The basic principle is the following: a certain portion of the photoelectrons will pass through the aperture in the inner cylinder and, depending on the potential applied to the outer cylinder electrons of the desired energy will go through the detector aperture. The energy spectrum is built up by scanning the potential on the outer cylinder.
The HSA configuration offers an higer spectral resolution, accompanied by the possibility to collect electrons from a larger sample area. An HSA (see figure 3.6) consists of an hemispherical capacitor composed by two concentric hemispherical electrodes, one or more electrostatic lenses positioned between the sample and the capacitor, and a detector. By appliyng a potential differece ΔV between the electrodes, the only electrons which can pass through the whole capacitor and reach the detector are those with a kinetic energy given by

$$E = e\Delta V \frac{R_1 R_2}{R_2^2 - R_1^2} \tag{3.4}$$

where e is the electron charge and R_1 and R_2 are the radii of the inner and outer electrodes, respectively.
The lenses positioned at the input of the analyser performs a double function: they collect and focus the electrons emitted over a certain angle and, applying an appropriate potential they can also retard them. Indeed, the electron energy is usually too great

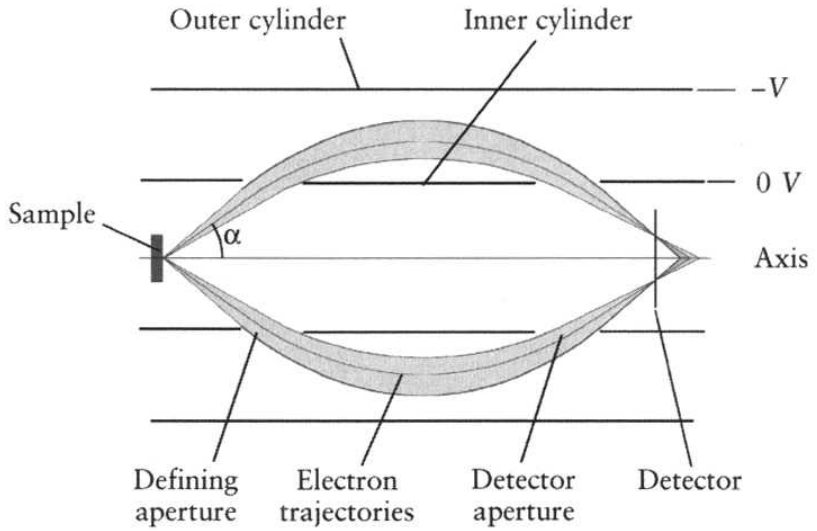

Figure 3.5: Schematic representation of the cylindrical mirror analyser (CMA) [71].

for the analyser to produce sufficiently high resolution. The XPS measurements for this thesis were performed by Dr. Saulius Kaciulis and Dr. Alessio Mezzi at CNR - ISMN in Rome, with an ESCALAB Mk II (VG scientific - UK), Al/Mg double anode source, 5 channeltron detector. Binding energy calibrated with C 1s at 285.0 eV

3.3 The X-Ray Diffraction

The X-ray diffraction (XRD) is an analysis method for the determination of the atomic stucture of a sample, exploiting the elastic scattering between an X-ray beam and the atoms constituting the investigated sample. This tecnique in based on the fact that the X-rays wavelength (~ 1 Å) is comparable to the interplanar distance of crystals. The informations on the stucture of the sample are estracted from the diffraction pattern produced by the scattered beams. Among the numerous tecniques involving XRD, we are mainly interested to the simplest case of single crystal XRD, in which a monocromatic collimated X-ray beam is sent to a single crystal sample. The main advanges concerning crystals arising from the definite orientation of the structure, in contrast to the random orientation of powders or molecules.
The measured quantity in an XRD experiments is the intensity of the diffracted rays, in particular the diffraction peaks due to constructive interference, their angular position, intensity and width. Given a crystal lattice with lattice vectors $\mathbf{R}$ and let $\mathbf{r_j}$ the position of the atoms with respect to any one lattice site, a simple Kinematical treatment [72]

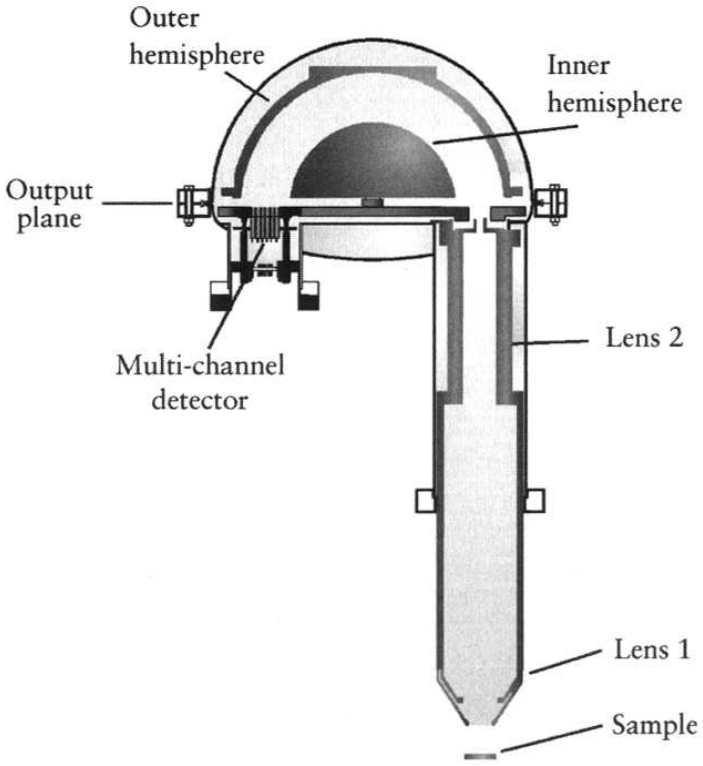

Figure 3.6: Schematic view of the hemispherical sector analyser (HSA) [71].

provides, for a wavevector transfer $\mathbf{Q} = \mathbf{k} - \mathbf{k}'$ with $|\mathbf{k}| = |\mathbf{k}'|$, a scattering amplitude

$$F(\mathbf{Q}) = \sum_j f_j(\mathbf{Q}) e^{i\mathbf{Q}\cdot\mathbf{r_j}} \sum_{\mathbf{R}} e^{i\mathbf{Q}\cdot\mathbf{R}} \tag{3.5}$$

where $f_j\mathbf{Q}$ is the atomic form factor. This leads to the so-called *Laue condition* for the reflection (diffraction peak) expressed by $\mathbf{R}\cdot\mathbf{Q} = 2\pi n$, where n is an integer. In practice each reflection is identified by a tern of numbers that defines $\mathbf{Q}$. Such a request is fulfilled by the reciprocal lattice vectors $\mathbf{G_{h,k,l}}$. It is easy to show that this condition is completely eqivalent to the well known Bragg's law

$$n\lambda = 2d\sin\theta, \tag{3.6}$$

where n is a positive integer, λ is the wave length of the incident beam, d the interplanar distance, and θ the scattering angle. The relation between the interplanar distances and the reciprocal lattice vectors is $d_{h,k,l} = 2\pi/|\mathbf{G}_{h,k,l}|$. Thus, the position of the peaks (θ) allow us to determine the interplanar distances of a crystal.

Another relevant information is provided by the intensity of the peaks; the intensity in each point ($I(\mathbf{Q}) \propto |F(\mathbf{Q})|^2$) is modulated by the absolute square of the unit cell structure factor ($\sum_j f_j(\mathbf{Q}) e^{i\mathbf{Q}\cdot\mathbf{r_j}}$), which depends on the position of the atoms in the unit cell. Than, a measure of a large set of intensities it is possible to deduce the atomic structure into the cell [72]. In this treatment we do not consider other characteristics of the diffraction pattern, such as the shape and the width of the peaks, which provide informations on the crystal defects and on the dimension of crystallites in the case of policrystalline samples.
The XRD measuremets concerning this thesis were done using a Bruker diffractometer with Cu Kα1 radiation. The procedure includes reflectometry and $\theta - 2\theta$ scans. In the $\theta - 2\theta$ geometry the X-ray source is fixed, the sample rotates with angular velocity ω, and the detector rotates with velocity 2ω around the sample. In this way the scattering angle of the collected rays is always equal to the incident angle. In practice the sample is maintained tangent to the focusing circle.

3.4 Capacitance Measurements

The dielectric properties of the capacitors fabricated in this thesis has been investigated by electrical measurements. In particular, two terminal impedance measurements and and I(V) measurements in the temperature range from about 77 K (nitrogen liquefaction temperature) to room temperature has been performed by means of a cryostat.
A schematic view of the cryostat is shown in figure 3.7. The sample is mounted on a sample holder, which is provided of electrical connectors, and is top-loaded through an acces on the top of the cryostat. The nitrogen is delivered to the cryostat by a vacuum-insulated transfer tube inserted in the syphon entry arm. A cooler circuit leads the nitrogen to the heat exchanger which surrounds the sample space. To achieve the needed heat exchange, a nitrogen pressure of about 0.1 bar is maintained in the the sample space through an independent vacuum circuit.
The temperature sensor is a thermocouple fitted to a copper finger below the sample space. Also, two heater blocks are fitted to the same copper finger. The various parts of the cooling system and their connections are depicted in figure 3.8. This system is based on the continuous transfer of coolant to the cryostat, controlled using a gas flow controller. The temperature is controlled by a controller connected to the heaters.
The impedance measurements has been performed in the frequency range from 20 to 2 MHz using an RLC-meter (Agilent E4980A). The I(V) measurements for the determination of the resistance of the samples were done using a source measurement unit (KEITHLEY 236). The collection and processing of the data were performed by means of the software LabVIEW and Origin, respectively.

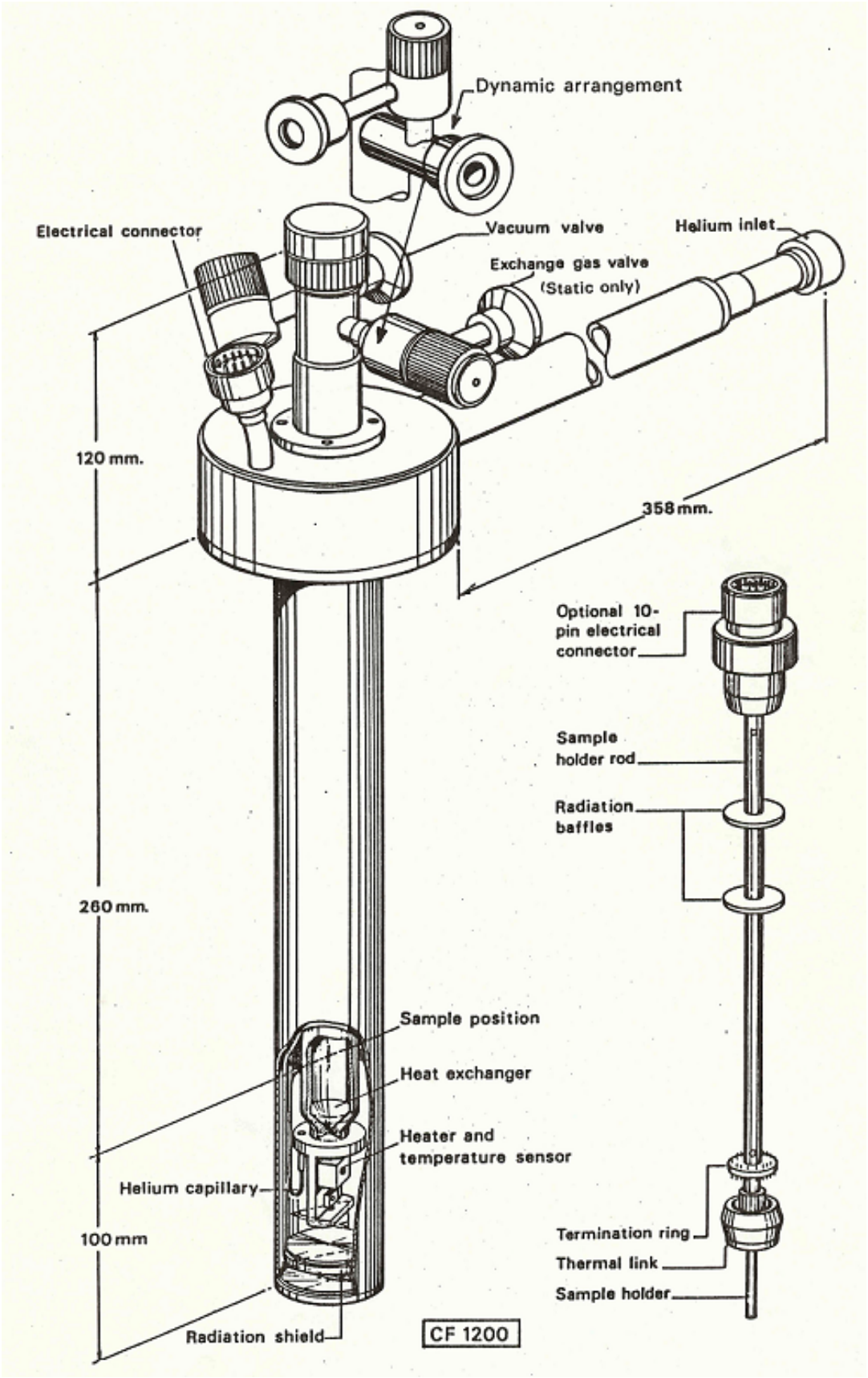

Figure 3.7: Schematic representation of the cryostat and the sample holder for low temperature electric measurements.

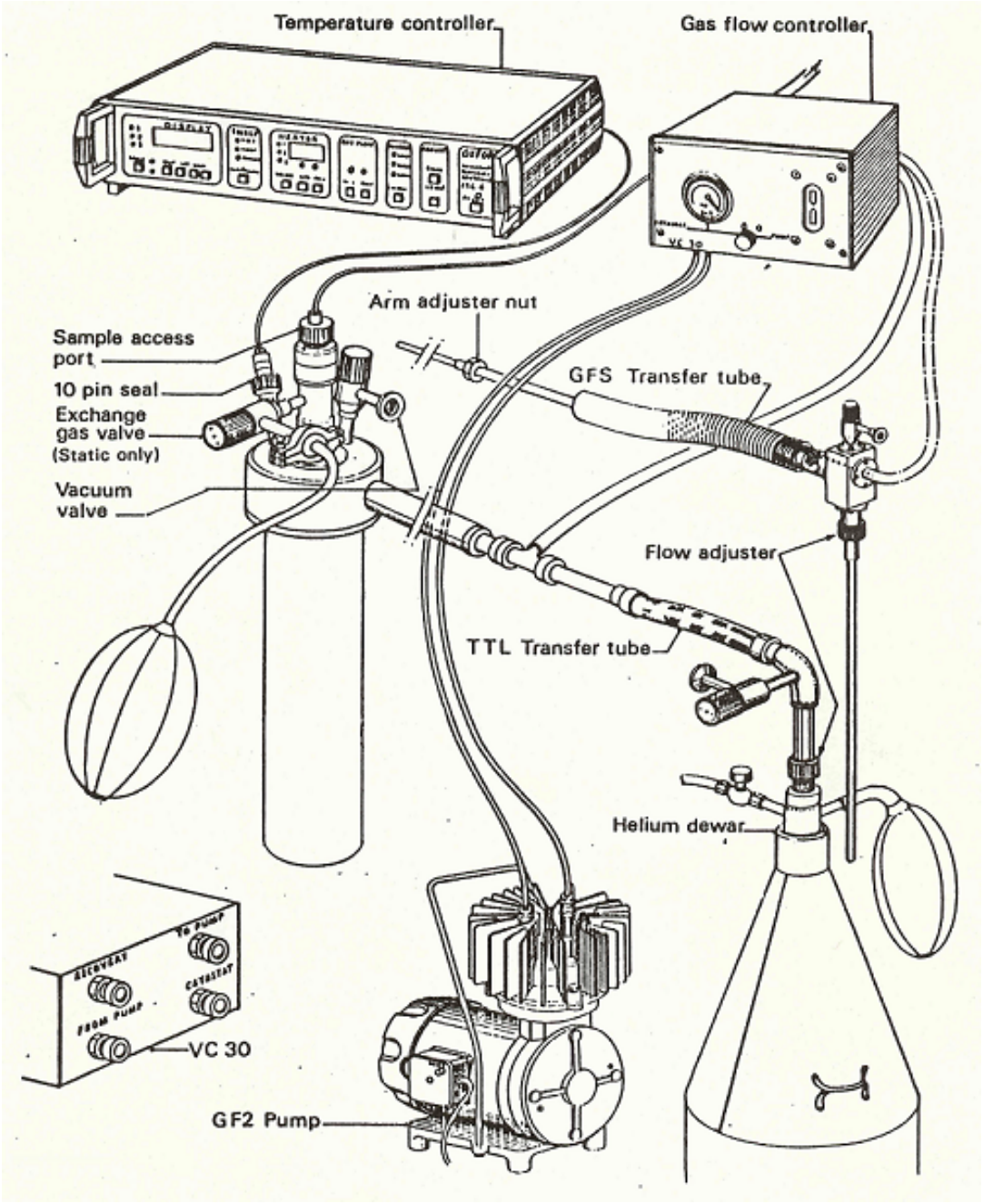

Figure 3.8: Schematic picture of the cryogenic apparatus components and their connection.

Chapter 4

Experimental Results and Discussion

In this chapter we describe the fabrication procedures and the characterization of the devices which constitutes the object of this thesis. In particular, in section 4.1 we describe the deposition of epitaxial LSMO film on STO substrate and the deposition of STO film (both amorphous and crystalline) on the LSMO film for the fabrication of LSMO/STO/Co spintronic devices. In sections 4.2 and 4.3 we discuss the fabrication and characterization of some capacitors in the MIS (metal/insulator/semiconductor) configuration with parallel-plate geometry, based on the epitaxial growth of STO (section 4.2) and NGO (section 4.3) thin films as dielectrics on Nb doped STO substrates. Indeed, the Nb impurity changes STO insulator into an n-type semiconductor, whose resistivity depends on the doping level.

4.1 LSMO/STO/Co Junctions

This section describes the work on LSMO/STO/Co junctions as inorganic counterparts of the Alq_3 based organic Magnetically Enhanced Memristors (MEM) [73]. Such a particular device is a memristor with ferromagnetic electrodes and combines electric and magnetic memories [32], [74]. The memristor is a kind of device having two stable resistive states (electrical bistability) and is thought to be a promising device for future memory and computing applications [75]. It is characterized by two non-volatile resistive states which have zero current at zero applied voltage. A typical memristive characteristic is shown in figure 4.1, from [76].
LSMO/Alq_3/AlO_x/Co devices are prototypical organic spin valves with two resistive states according to the relative magnetization orientation of the LSMO and Co electrodes - a property named magnetoresistance (MR) which we described in the first chapter. They also feature memristive behavior and, most relevant, an interrelationship exists

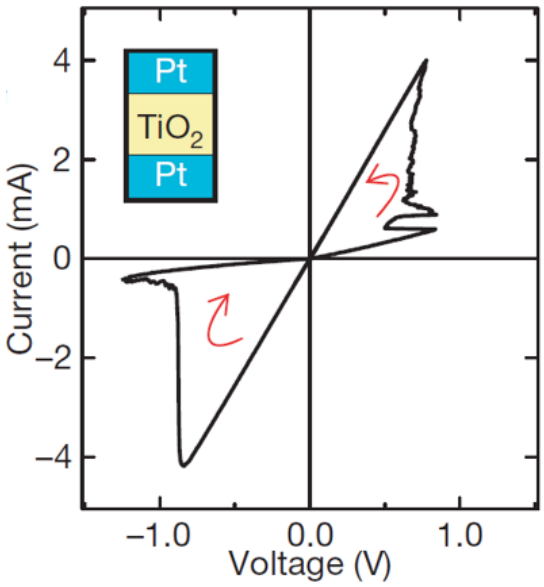

Figure 4.1: Typical I(V) characteristic of the memristor, with the two resistive states that cross at zero.

between resistive states from the memristor and the magnetoresistance signal from the bare spin valve behavior [32]. Especially the magnetoresistance percentage is modulated by the electrical bistability, as sketched in figure 4.2, from [73]. Here a sequence of I(V) curves is performed increasing the maximum negative voltage step by step. After each I(V), the magnetoresistance (R(H), where H is the in-plane magnetic field) is measured. The resistance of the device is lower when the LSMO and Co electrodes have antiparallel magnetization. This counterintuitive fact is very well established in literature and ascribed to the hybridization between the LSMO surface and the first molecular layer [77]. Such hybridization creates a sort of spin filtering layer and a new object, which is named *spinterface* [78]. It is noticeable that only in the lower resistance states (red color) the MR signal exists, while after a certain resistance value the MR is no longer detected (black color). By moving only on two resistive states, one (low resistance) with finite MR and one (high resistance) with no MR, we can build a universal logic gate with only one device [73].
We studied this behavior in fully inorganic devices, namely LSMO/STO/Co. LSMO and STO are deposited by Channel Spark while Co and Au pads were evaporated respectively by e-gun and thermal evaporation by Elisabetta Zuccatti. The device have a cross bar geometry defined by shadow masking. The resulting area is 1 mm x 200 μm. The advantages of a fully inorganic devices are expected to be the endurance and the resistance over stronger conditions such as radiations.

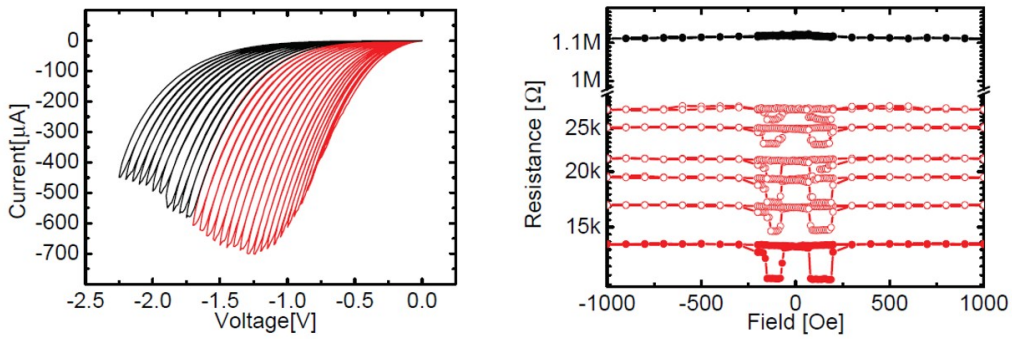

Figure 4.2: Negative branch of the I(V) characteristics of LSMO/Alq_3/AlO_x/Co devices (left) with the corresponding magnetoresistance (right). The red states have a non-zero magnetoresistance whose amount depends on the resistance itself.

4.1.1 LSMO Deposition and Characterization

LSMO is deposited by the Channel Spark Ablation (CSA) at an accelerating voltage of 9 KV and an oxygen pressure from 3.8 to $4.0{\cdot}10^{-2}$ mbar. The corresponding rate is about 0.12 /Å/pulse with a repetition rate of 3.5 Hz. The substrate temperature during the deposition is controlled by an optical pyrometer and can be estimated around 800°C. LSMO thin films were deposited on SrTiO3 (100) (STO) and on NdGaO3 (110) (NGO) substrates. The former is cubic with a lattice constant of 0.3905 nm while the latter is orthorhombic with lattice parameters of 0.543 nm, 0.55 nm and 0.771 nm. LSMO is rhombohedral with a pseudocubic lattice parameter of 0.387nm. The resulting mismatch is tensile for an amount of 0.89 % in the case of STO (100) and compressive for an amount of 0.39 % and 0.26 % along the two in-plane crystallographic orientations in the case of NGO (110).
The AFM image of a typical 9 nm LSMO film deposited on STO substrate is reported in figure 4.3(a) while its characteristic temperature behavior is shown in figure 4.3(b). A metal insulator transition (MIT) higher than 350 K and a curie temperature of 310 K are extracted, typical values for films of this thickness. The epitaxy is confirmed by XRD (figure 4.3(c), from Prof. Georg Schmidt, University of Halle), and TEM measurements (from Dr. Kerry O'Shea, University of Glasgow, shown in the next subsection). The XPS characterization was performed by Dr. Saulius Kaciulis, CNR - ISMN, Montelibretti Research Area (Rome). The stoichiometry appeared in good agreement with the nominal one, with a Sr enrichment at the surface. XPS measurements also ensured the absence of any contamination.

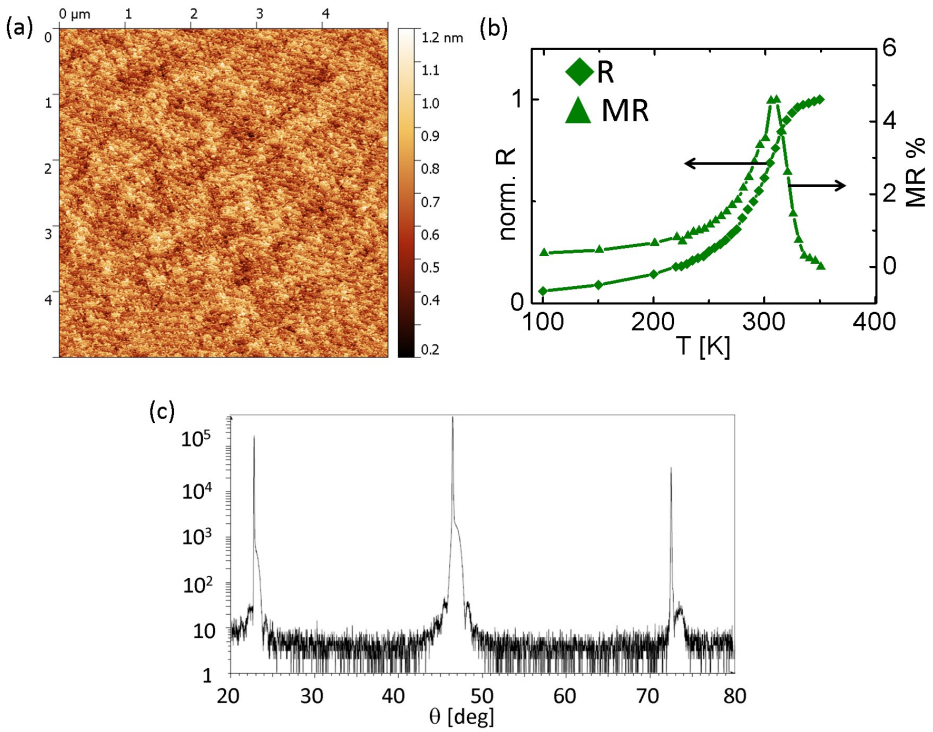

Figure 4.3: AFM image of a 9 nm thin film, rms is 0.2 nm (a) and corresponding R(T) and MR(T) according to the labels (b); XRD data (c).

4.1.2 STO on LSMO Growth Parameters

STO is deposited by CSA at an accelerating voltage of 13.5 kV and an oxygen pressure of $2.6 \cdot 10^{-2}$ mbar, resulting in a deposition rate of 0.2 Å/pulse. We tuned the STO crystallinity between epitaxial and amorphous by varying the substrate temperature from 650°C (epitaxial) to about 300°C (amorphous).
TEM characterization of the junction was performed by Dr. Kerry O'Shea from the University of Glasgow. Figure 4.4 summarize these results for two LSMO/STO/Co junctions deposited on NGO substrates. The left column contains the data for a junction

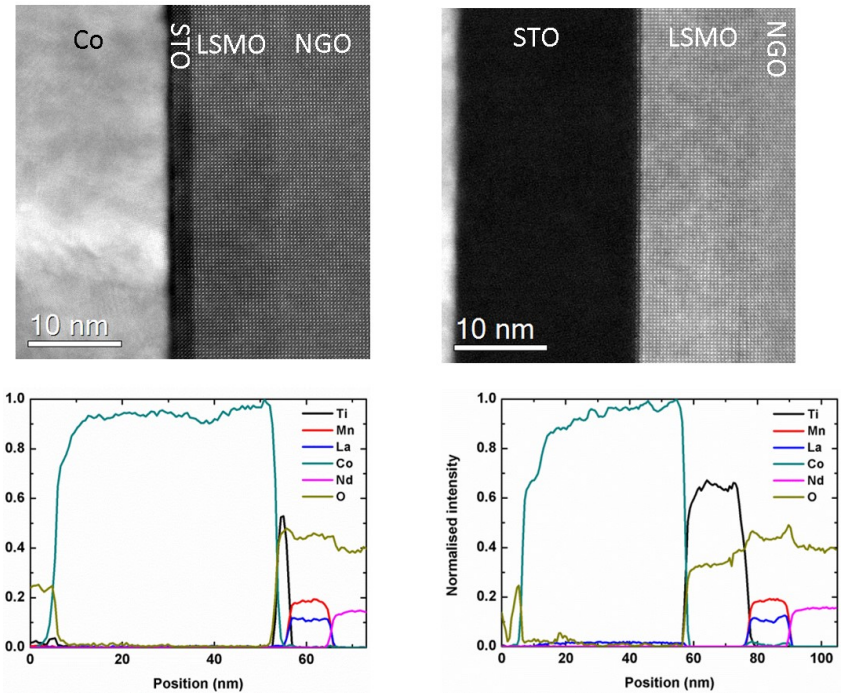

Figure 4.4: TEM analysis of LSMO/STO/Co junctions deposited on NGO substrates. The top raw shows cross sectional TEM while the bottom raw reports the corresponding EELS. The left column is about junctions with epitaxial STO while the right column is about junctions with amorphous STO.

with epitaxial STO while the right one shows the data for a junction with an amorphous STO layer.
The top row shows the TEM section while the bottom row the corresponding chemical analysis via electron energy loss spectroscopy (EELS). It is possible to notice that the epitaxial STO layer shows excellent epitaxy with the bottom LSMO layer and a perfect stoichiometry. The amorphous STO layer is effectively not ordered and the EELS that it is Ti rich - Sr deficient.

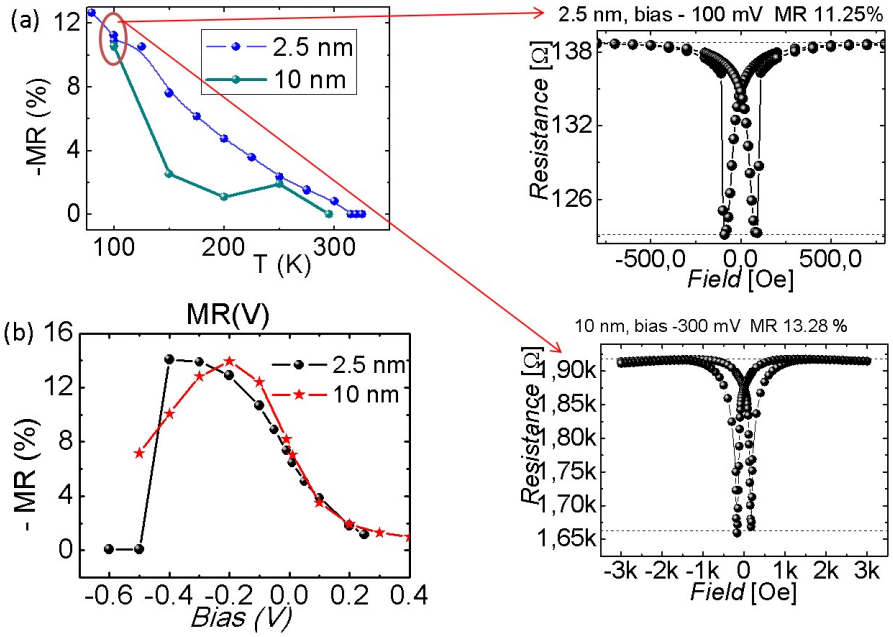

Figure 4.5: (a) MR(T) for junctions with epitaxial STO barrier of 2.5 and 10 nm, according to the legend. The arrows indicates R(H) measurements at 100 K. (b) MR dependence on the applied bias.

4.1.3 The LSMO/STO/Co Device

We now summarize the data from the device characterization. These measurements were performed by Dr. Marco Calbucci and by Dr. Lorenzo Vistoli. Figure 4.5 sketches the MR measurements for the junctions with 2.5 and 10 nm of epitaxial STO barrier. The bias applied during the MR measurements is referred to the Co electrode, which is always grounded.

In (a) we report the MR percentage versus temperature, with two magnetoresistive cycles measured at 100 K for the two STO thicknesses in the right column, enlightened by two arrows. One can notice the inversed magnetoresistance, i.e. the resistance is lower when LSMO and Co electrodes have antiparallel magnetization. This is a very well established fact in literature and is explained with the interaction between Co atoms and Ti ions at the STO/Co interface [18].

In (b) we describe the dependence of the MR percentage on the applied bias during the Mr measurements. The observed dependence is in clear agreement with the established literature data and originates from the Fermi level movement along the Density of States of the LSMO and Co electrodes under the applied bias [18].

The I(V) curves of the junctions with STO epitaxial barriers feature a typical nonlinear

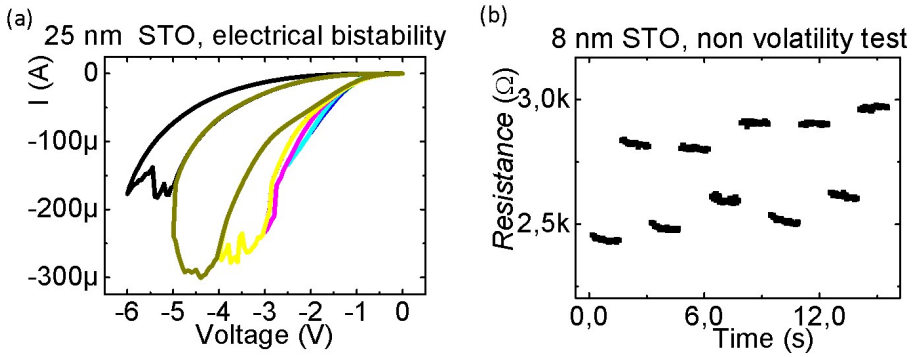

Figure 4.6: : (a) negative branch of several I(V) characteristics for a device with 25 nm of amorphous STO as barrier; each color corresponds to a resistance state. (b) non-volatility memory test of a device with 8 nm of amorphous STO barrier.

tunneling behavior and do not show any trace of bistability: epitaxial STO deposited in oxygen environment by CSA is a good candidate for magnetic tunnel junctions but for memristors. I(V)s are not shown. The resistivity of the junction is in the range 150 - 400 Ω cm.

The junctions with amorphous STO barrier have a clearly different behavior. First, they feature electrical bistability, i.e. they are memristors, as already found for devices with an amorphous STO layer sandwiched between two non-ferromagnetic electrodes [79]. Second, an interesting magnetoresistive behavior is present.

Figure 4.6 summarizes the main results on the MR data for a device with a 25 nm amorphous STO spacer, measured at 100 K. The pristine device have a very low MR, and even low resistance. Moreover the R(H) shape resembles the one of the LSMO electrode [80]. If we perform several consecutive I(V) curves in the positive branch, i.e. current is flowing from LSMO to Cobalt, electrons do the opposite, we observe a memristive behavior with each I(V) forward that follows the previous I(V) backward. After about 6.5 V, an abrupt jump is observed in the current and the final resistance is permanently increased. The flat line at 20 mA is due to the current compliance of the instrument. Such a sort of electroforming is actually the opposite of the standard one, where the resistance decreases after the forming [81]. Here the resistance increases and the MR changes radically, as the left panel shows. Probably this electroforming burns some conductive paths and the device have now typical MR percentage and coercive fields of LSMO and Co based spin valves with amorphous spacer memories [32].

Figure 4.7 shows the electrical behavior of the amorphous STO based devices after the *electroforming* reported in figure 4.6. Figure 4.7(a) reports a set of I(V) characteristics measured applying a consequently increasing maximum negative voltage; each color corresponds to a resistive state. One can observe that the forward direction of each I(V)

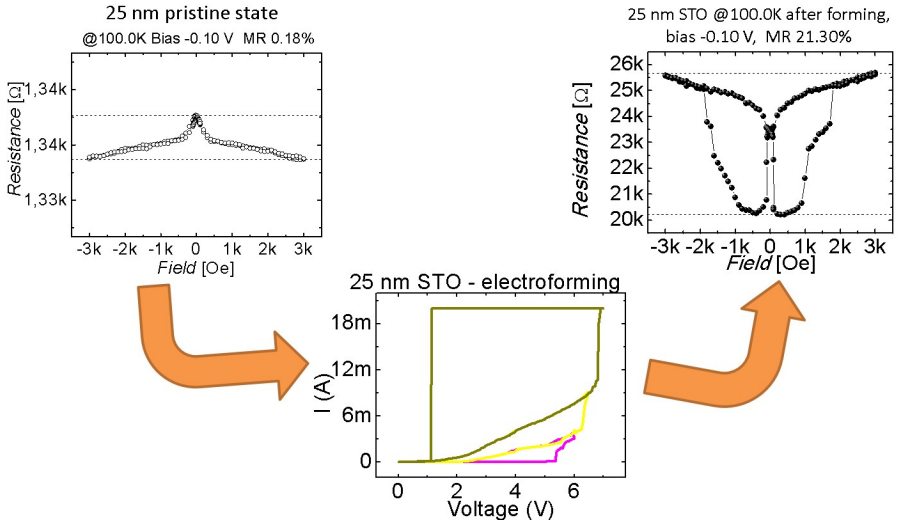

Figure 4.7: MR measurements of a device with 25 nm thick amorphous STO barrier in the pristine state (left) and after a forming process (right). The I(V) in the bottom of the figure summarize the forming process: a gradually increasing positive bias is applied until an abrupt jump in the conductivity.

always follows the backward direction of the previous one (from 0 to maximum negative than to 0 again). Also the negative differential resistance (NDR) is present, probably due to the low conductivity of STO, for which the injected charges cannot reach the counter electrode before further charges are injected, thus the injected charges create an internal electric field that inhibits further charge injection [82].
Figure X7b shows a brief test on the non-volatility of the states for a device with 8 nm of amorphous STO as barrier. Two states are clearly identified although their stability over time is still lower in respect to the organic ones.
Unlikely, a clear correlation between the resistance states and the MR was not found: it is not possible to control the MR percentage by means of the electric states.
In facts, these amorphous STO based junctions are really promising but require further optimization work.

4.2 STO Capacitors

4.2.1 STO on Nb:STO Growth

We used the channel spark method to homoepitaxially grown STO thin films of about 30 nm-thick on Nb doped STO substrates, for the fabrication of parallel-plate capacitors with high-κ dielectric. In this configuration the STO film plays the role of dielectric and

Figure 4.8: A view of the In pasted STO target before (on left) and after (on right) some depositions.

the Nb:STO substrate is the bottom electrode. An Au circular contact with a 2 mm diameter was successively deposited on the film as top electrode.
The most important aspects to achieve an high dielectric constant in STO are high crystalline purity, epitaxial growth and low density of oxygen vacancies. To explore the dependence of the film quality on the deposition temperature we had fabricate four devices with different dielectric layer growth temperature, in the range from 640 to 750°C.
The STO substrates were (100) oriented and they had a Nb doping concentration of 0.2 at%. Their dimensions were $5 \times 5 \times 0.5\,\mathrm{mm}^3$. Before to be placed into the chamber, each substrate has been cleaned using isopropanol vapors. The STO stoichiometric target was pasted to the copper target holder by means of indium, which provides both thermal and electrical contact. Moreover, the mechanical support was strength by an additional Al_2O_3 screw (see figure 4.8).
The suitable growth parameters depend not only on the concerned material, but also on the particular CSA system. In our case we had individuate the optimal conditions of $2.60 \cdot 10^{-2}$ mbar of oxygen pressure, an accelerating voltage of 13 kV and a frequency of the pulsed electron beam of 3 Hz. These conditions lead to a growth rate of about 2 nm/min, than, 30 nm-thick films has required 15 minutes depositions.
To investigate the film thickness, in addition to the Nb:STO substrate, also a Si substrate, which was partially covered by a Pt strip, has been placed into the chamber. At the end of each deposition we estimated the film thickness by measuring the step between the film and the clean side of the Si substrate.
We had grown four STO films at the substrate temperatures of 640, 700, 725 and 770°C of about 30 nm thickness. Two additional films of larger thickness (53 nm and 170 nm) has

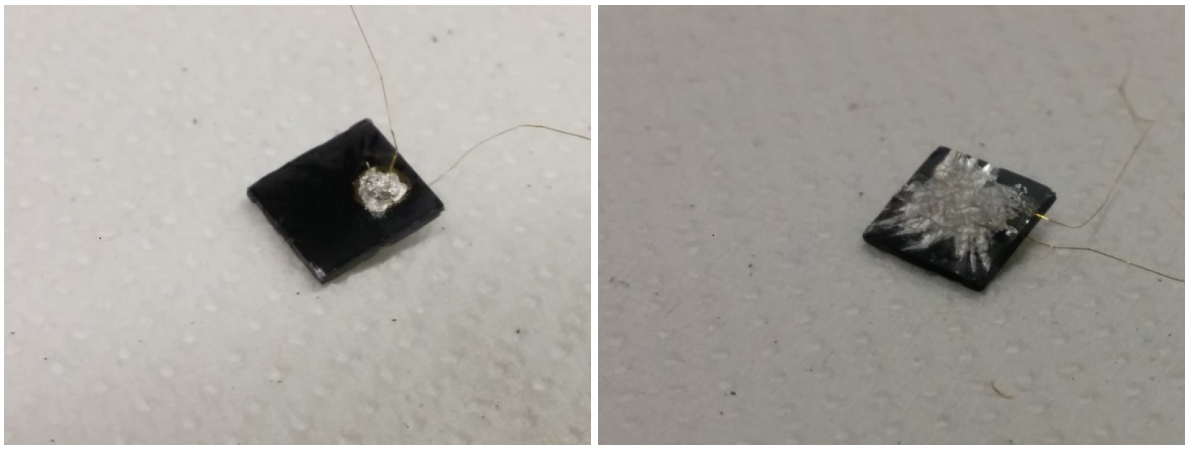

Figure 4.9: Top (left) and bottom (right) views af an Au/STO/Nb:STO sample.

been deposited at the temperature of 700°C and an oxygen pressure of $2.10 \cdot 10^{-2}$ mbar on STO substrates with a Nb concentration of 0.7 wt%. The temperature was controlled by a current flowing in the heater and it was monitored using a pyrometer, setting the emissivity at the value $\epsilon = 1$. To reduce the surface defects we didn't perform any kind of annealing after the deposition, but we rapidly cooled (quenching) the sample at the same O_2 pressure of the deposition. However, we fabricated an additional annealed sample (growth temperature of 700°C) to check the effects of an oxidative annealing on the STO dielectric constant. As suggested in [83], to remove the oxygen vacancies the sample was postannealed in air at 400°C for 24 h.
Then, an Au circular top electrode with a 2 mm diameter was deposited on the film and a small quantity of In was spread on the backside of the substrate which works as bottom electrode (figure 4.9, right). The indium contact is needed to obtain an ohmic junction with Nb:STO, which is an n-type semiconductor [84]. To be precise, the device contacts were obtained following two different procedures: on the films grown at 640 and 720°C the Au electode were deposited after the spreading of the In layer. In all other cases we adopted the opposite sequence. In order to perform the impedance measurements, both top and bottom electrodes were connected to the measuring apparatus with Au wires by means of a silver conductive paint (figure 4.9).

4.2.2 Electrical Characterization

For the determination of the samples capacitance, impedance measurements has been performed in the frequency range from 20 to 2 MHz with 0.01 V signal.
Figure 4.10 shows the room temperature behaviour of the impedance modulus and phase

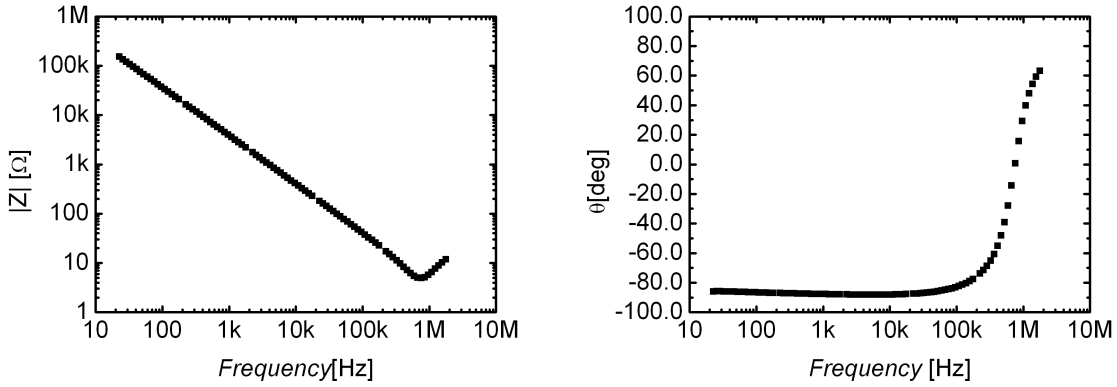

Figure 4.10: Left: Impedance modulus (left) and phase (right) as a function of frequency for an Au/STO/Nb:STO capacitor grown at 770°C, measured at 295 K.

for a device grown at 770°C. All the room temperature measurements have a similar behaviour, suggesting that the samples are characterized by high resistance (from 30 to 300 MΩ) and can be considered as purely capacitive devices. As we verified, the capacitance can be calculated using the approximation $C = 1/\omega|Z|$. At lower temperature, some devices exhibited a dramatic reduction in their resistance, down to 20 Ω; in these cases the contribution of the resistance to the overall impedance needs to be taken into consideration.
In the frequency range around 10^6 Hz the impedance modulus rapidly decreases and the phase becomes zero from below. This behaviour is due to uncompensated circuit elements. In a few word there should be some inductive component whose reactance perfectly compensate, at a certain frequency, the capacitance contribution, resulting in a resonance. Than, as the frequency increases, this inductance contribution to the impedance becomes larger and larger, and the phase bacomes positive.
Representing the device by the parallel of a capacitance C_L and a resistance R_L, the described behaviour can be reproduced introducing an RLC model of the cables in the configuration shown in figure 4.11. At low frequencies all this contributions are negligible

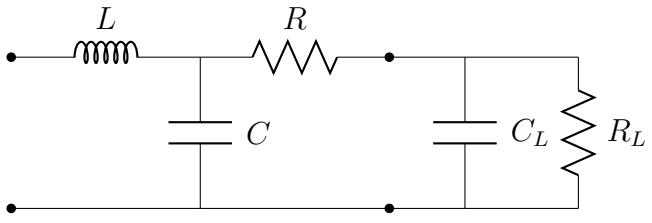

Figure 4.11: RLC model of the cables connecting the davice to the measuring apparatus.

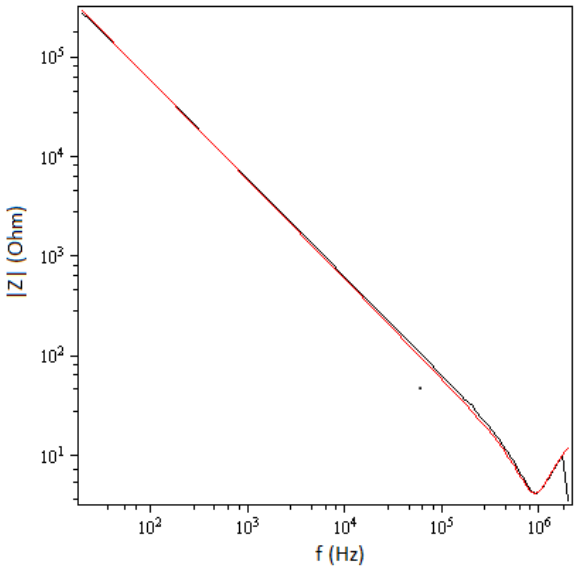

Figure 4.12: Fit of the proposed RLC model (red) and experimental data (black) for a $C_L = 26\,\mathrm{nF}$, $R_L = 0.5\,\mathrm{G\Omega}$, device.

and the response is dominated by the device capacitance. A simulation of this model applied to a device of capacitance $C_L = 26\,\mathrm{nF}$ and resistance $R_L = 0.5\,\mathrm{G\Omega}$, provides the following RLC values: $R = 4.5\,\Omega$, $L = 1.15\,\mu\mathrm{H}$ and $C = 1\,\mathrm{nF}$. The calculated impedance modulus as a function of frequency is shown in figure 4.12.
Figure 4.13 shows the I(V) curve for a capacitor with the STO dielectric film grown at 725°C. The brekdown occurence for the same device is reported in figure 4.14. As we can see the I(V) curves are not symmetric. We repeated some measurements contacting the backside of the substrate directly with silver paste: in this way the I(V) curves were symmetric and the capacitance values slightly increased. However all over this thesis we reported the data collected with the backside indium contact. The main features of the fabricated capacitors are resumed in table 4.1. The relative dielectric constant was calculated from the capacitance C using the formula $\epsilon = Ct/\epsilon_0 A$, where t is the film thickness and $A = 3.14\,\mathrm{mm}^2$ is the top electrode area. The large uncertainty on the dielectric constant is completely due to the error on the capacitors dimensions (film thickness and top electrode area).
The films grown at 700 and 770°C exhibits the highest dielectric constant and, at the same time, the lowest resistance. We ascribe this differences to the procedure used to contact the devices grown at 640 and 725°C (see section 4.2.1). In this cases the Au top electrode was deposited only after the spreading of the indium layer. This means that the film wasn't cover by the Au contact when the indium was spread. We think that this fact may have damaged the STO films, resulting in a reduction in the dielectric

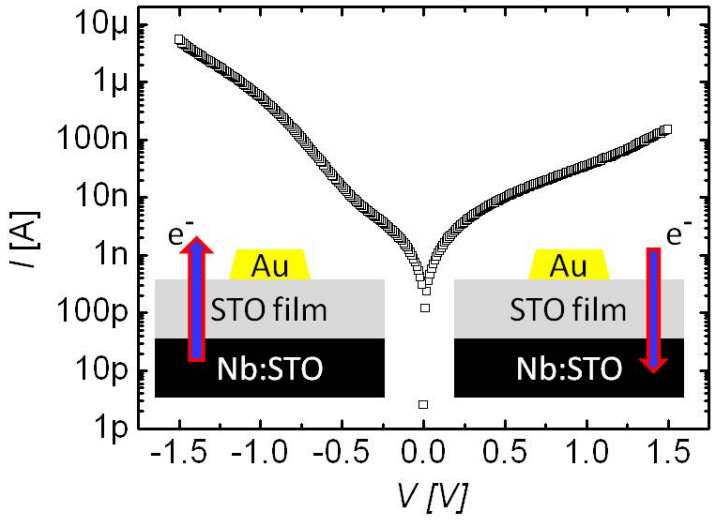

Figure 4.13: I(V) curve (absolute value) for an Au/STO/Nb:STO device (growth temperature of 725°C).

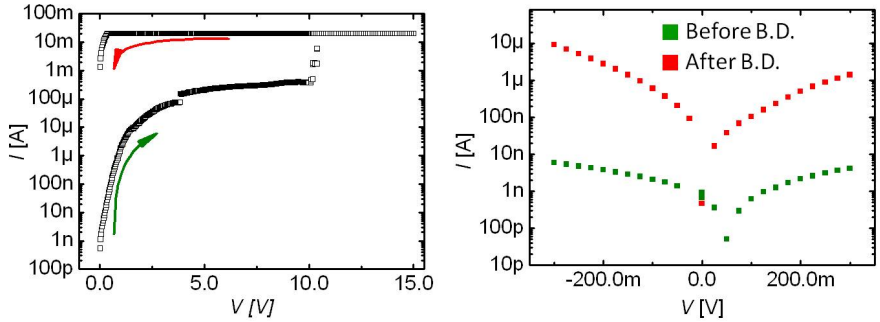

Figure 4.14: I(V) curves for an Au/STO/Nb:STO device (growth temperature of 725°C) before and after the application of a brekdown voltage.

Growth temperature (°C)	640	700	725	770	700 Annealed
Substrate doping (Nb)	0.2at%	0.2at%	0.2at%	0.2at%	0.7wt%
Thickness (nm)	30 ± 2	40 ± 2	30 ± 2	30 ± 2	32 ± 2
Resistance (MΩ)	300	20	200	30	10000
Capacitance (nF)	29	46	26	45	18
C per unit area (fF/μm^2)	9.2±0.9	14.6±1.4	8.3±0.8	14.3±1.4	5.7 ± 0.6
Permittivity ϵ_r	31±5	67±10	28±4	49±7	21 ± 3
Breakdown voltage (MV/cm)	2.7	6.3	3.5		1.1
Leakage curr. at 1 V (A/cm^2)	$1.9 \cdot 10^{-3}$	$6.5 \cdot 10^{-6}$	$1.7 \cdot 10^{-5}$		$2.8 \cdot 10^{-8}$

Table 4.1: Features of the Au/STO/Nb:STO capacitors at room temperature. The I(V) curves (figure 4.13) are not symmetric: the reported value of leakage current is the highest measured. It may be interesting the comparison whith the TaN/STO/TaN device ($t = 30$ nm, $A = 20 \times 20\,\mu$m^2) obtained in [85], which exhibits one of the highest capacitance density ever achieved: $C/A = 44$ fF/μm^2, leakage current $= 5 \cdot 10^{-7}$ A/cm^2 at 1 V.

properties. We notice that even if this samples show an high resistance (measured in the range from −100 mV and +100 mV), their leakage current at 1 V is higher than that of the sample grown at 700°C.
As regards the annealed sample, it shows the lowest dielectric constant of the whole set, and, at the same time, the highest resistance and the lowest leakage current. The latter two characteristics may be attribuited to a low concentration of oxygen vacancies, confirming the effectiveness of the performed annealing.
Since an increase in the STO dielectric properties at low temperature is expected, we performed the I-V and impedance measurements reducing T down to 77 K. However, any increase in the dielectric constant has been observed; if anything, the opposite. The temperature behaviour of the relative dielectric constants is shown in figure 4.15.
As the temperature is reduced below 250 K, the impedance for the samples grown at 700 and 770°C, which are those with the highest permittivity, has no longer a purely capacitive behaviour (see figure 4.16). This is related to an abrupt reduction in the resistance of the devices. For $T = 200$ K the resistance becomes 1.7 MΩ and for $T = 100$ K is less than 1 kΩ. The high resistance state was not restored by a subsequent increase in temperature. The resistance of this devices becomes larger again only after the reconstruction of the contacts between the Au wires and the electrodes. The causes of this behaviour are unknown.
By contrast, the resistance of the other devices, grown at 640 and 720°C increases as the the temperature decrease, from some MΩ at room temperature to many GΩ at 77 K, as we would expect from insulators.
We now consider the devices with the 53 and 170 nm-thick STO dielectric layer. Their

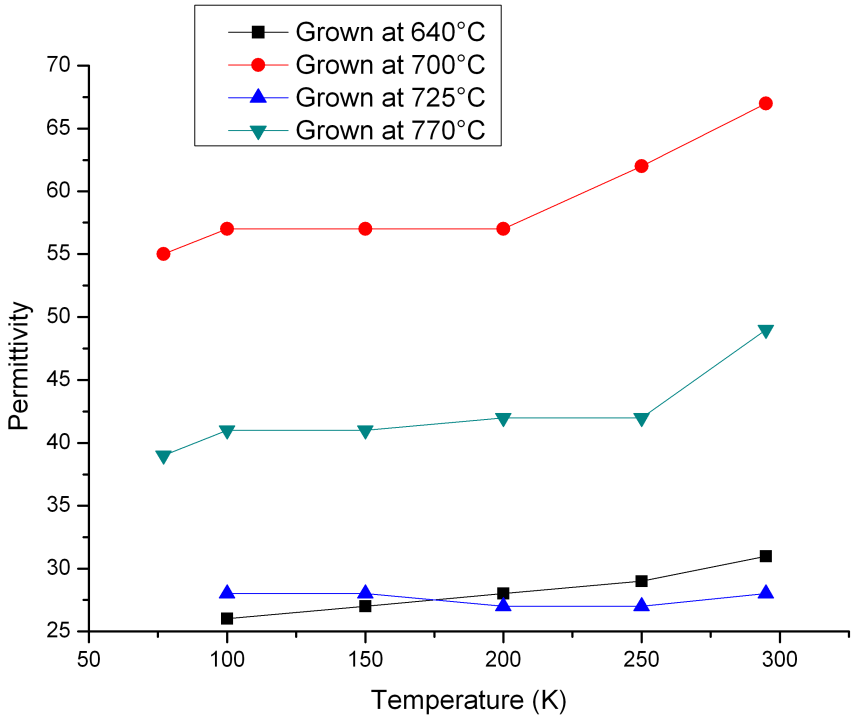

Figure 4.15: Temperature dependence of relative dielectric constant for STO films deposited at various temperatures. Al the values are affected by an error of about 15%, due to the uncertainty on the film thickness and on the top electrode area.

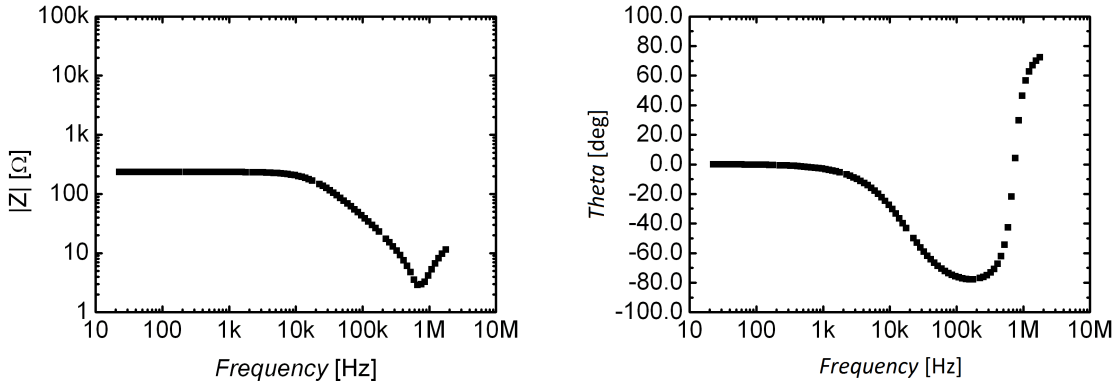

Figure 4.16: Impedance modulus (left) and phase (right) as a function of frequency for an Au/STO/Nb:STO capacitor grown at 770°C, measured at 150 K.

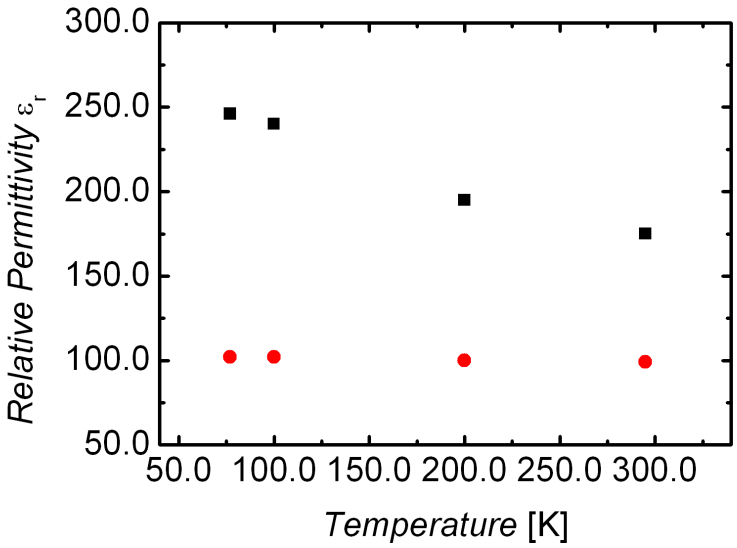

Figure 4.17: Relative permittivity as a function of temperature for 53 (red) and 170 nm-thick (blue) STO films.

capacitance of 52 and 28 nF, respectively, reflects very high values of dielectric constant, up to $\epsilon_r = 175$ at room temperature and $\epsilon_r = 250$ at 77 K for the film of 170 nm. Even if this thickess is not suitable for spintronics, its investigation provides precious informations that must be taken into account also for the growth of thinner films.
Figure 4.17 shows the dielectric constant ϵ_r as a function of temperature for both the devices. Even if the permittivity of the 53 nm-thick film of about 100 is larger than that of the previous set of films (figure 4.15), it appears almost independent on temperature. By contrast, the permittivity of the 170 nm-thick film results strongly temperature dependent: as the temperature decrease, it becomes larger and larger, as expected from strontium titanate [52]. Moreover, the so high observed value of permittivity is almost the same for the bulk STO crystal (see table 2.1, section 2.1). The combination of this things indicates that the extraordinary STO bulk properties tends to appear for film thickness exceeding a certain threshold. In our case, such a threshold-thickness seems to be larger than 50 nm.
It is known that the device capacitance can be reduced by a constant-valued stray capacitance C_i in series with the bulk film capacitance C_B. Such an interfacial capacitance may be localized at the metal/insulator interface [65], but can also be attribuited to the space-charge layer at the STO/Nb:STO interface [86]. Following this simple model the measured capacitance will be given by $1/C = 1/C_i + 1/C_B$. If the interfacial layer

completely belongs to the dielectric film[1], the effective thickness is reduced from t to $t - t_i$, where t_i is the interfacial capacitance thickness. Therefore we have:

$$\frac{1}{C} = \frac{1}{C_i} + \frac{1}{C_B} = \frac{t_i}{\epsilon_i \epsilon_0} + \frac{t - t_i}{\epsilon_B \epsilon_0}\,, \tag{4.1}$$

where ϵ_i is the interfacial relative permittivity.
If any interfacial capacitance occurs, it is expected to be thickness independent. In order to investigate the resulting effects, the authors of [65] measured the capacitance of some devices fabricate under the same conditions, but of different thickness (see section 2.1.3). Following the adopted model, if the inverse of the capacitance as a function of thickness is reported, the data for each temperature are expected to lie on straight line. The nonzero intercept, if present, can be attribuited to the interfacial capacitance. Once the interfacial capacitance is known, the real STO film dielectric constant can be recalculated[2].
However, the proposed model is based on the assumption that the dielectric connstant is unchanged for all the thicknesses, but we have just demonstrated that, in our case, the opposite is true. Anyway, we shows our results in 4.18, even though they are based on only two data points for each temperature. It must be emphasized the fact that these results can't be used to determine the potential interfacial capacitance. This fact is confirmed by the temperature dependence of the so calculated values of C_i.

4.3 NGO Capacitors

In this section we report on the fabrication and characterization of some parallel-plate capacitors with $NdGaO_3$ (NGO) dielectric layer grown on Nb doped STO.
The NGO films were deposited on Nb doped STO substrates with two different orientation. We used Nb:STO (110) and Nb:STO (100), since orthorhombic NGO ($a = 0.543\,\text{nm}$, $b = 0.550\,\text{nm}$ and $c = 0.771\,\text{nm}$) can be epitaxially grown on both the orientations, as shown in figure 4.19 and 4.20. Moreover, on STO (100) there are two competing phases and we cannot determine a priori which is the most stable; the ratio between them could depend on deposition temperature.

4.3.1 NGO on Nb:STO Growth - Set 1

For the fabrication of these Au/NGO/Nb:STO devices we tried to grow the NGO films using a different and more sophisticated CSA system. As shown in figures 4.21 and 4.22, this apparatus has a complete different configuration than that described in section

[1] This is not the case of tha STO/Nb:STO interface, in which any possible space charge layer will be localized into the doped substrate.

[2] ϵ_B can be determined if the film thickness t is large compared to the interfacial layer thickness.

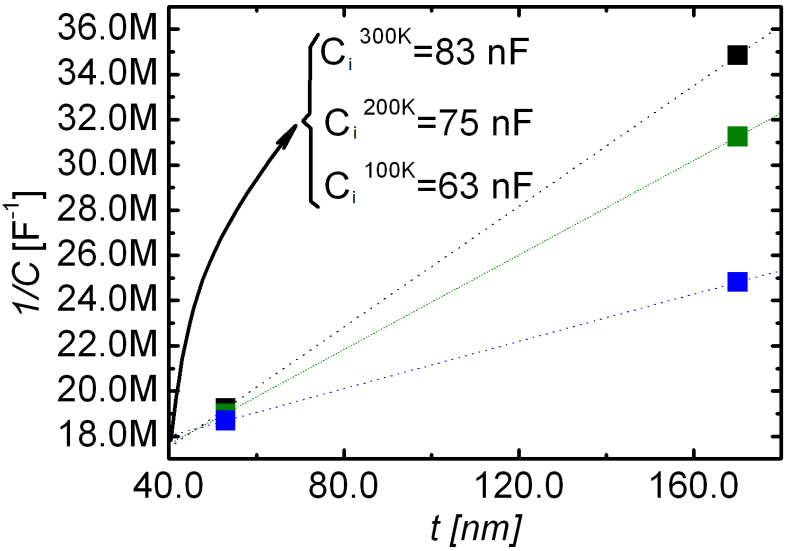

Figure 4.18: Inverse of the capacitance for Au/STO/NbSTO capacitors as a function of the STO film thickness, for three temperatures: 100 K (blue), 200 K (green) and 300 K (black). The values of C_i are calculated using equation 4.1.

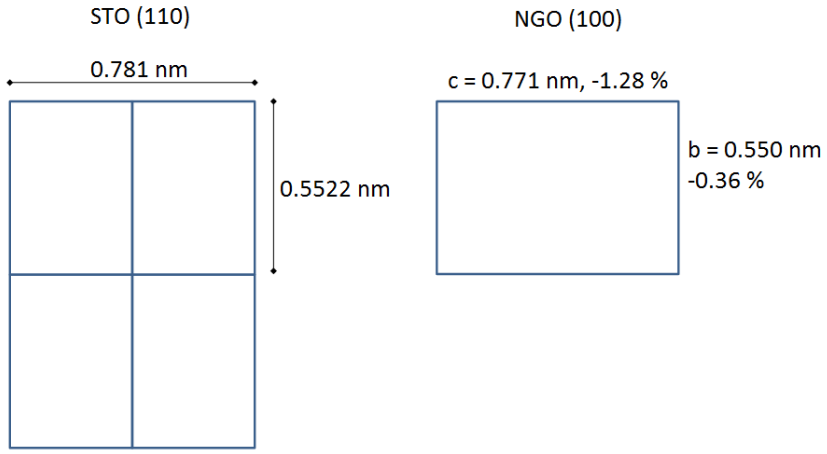

Figure 4.19: Lattice matching of NGO (100) on STO (110). Cubic STO has lattice parameter $a = 0.3905\,\text{nm}$, wherease the lattice constants of orthorhombic NGO are $a = 0.543\,\text{nm}$, $b = 0.550\,\text{nm}$ and $c = 0.771\,\text{nm}$, than it can be grown (100) exploiting the diagonal (0.5522 nm) end the double side length (0.781 nm) of the STO structure.

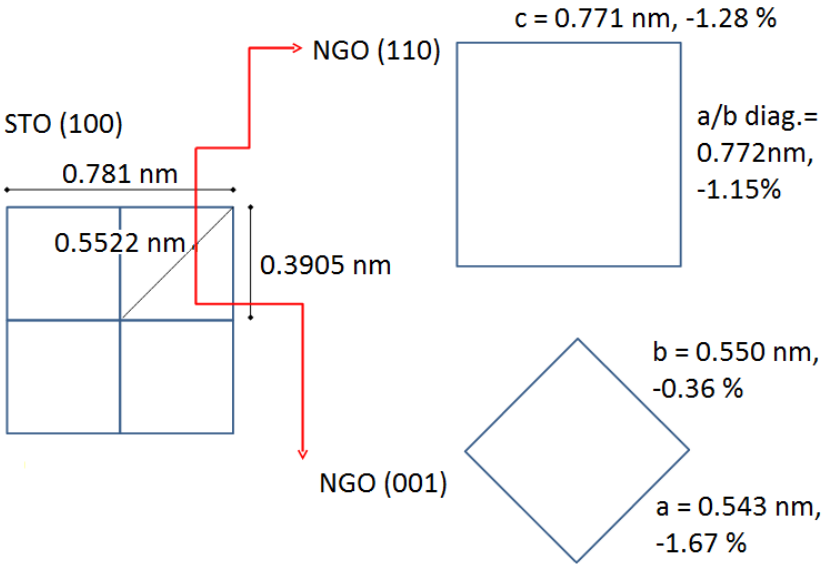

Figure 4.20: Two matching orientations of NGO on STO (100). NGO can be grown (110) exploiting twice the length of the STO lattice constant ($2 \times 0.3905 = 0.781\,\text{nm}$). Indeed, orthorhombic NGO has a lattice constant $c = 0.771\,\text{nm}$, wherease the diagonal formed by the a and b side is 0.772 nm. Also NGO (001) can be grown on STO (100), since the diagonal (0.5522 nm) of cubic STO match quite well with both a and b NGO side.

Peak	Binding energy (eV)	FWHM (eV)	Atomic %
Sr 3d	133.5	3.5	12.4
Ti 2p	457.5	3.8	9.6
C 1s	285.0	1.5	4.2
B 1s	191.2	1.1	7.5
O 1s	529.9	3.2	59.9
Ga $2p^3$	1117.9	3.6	1.9
Nd $3d^5$	982.4	3.9	8.4

Table 4.2: XPS quantification after sputtering for an NGO/Nb:STO(100) device grown at 760°C.

3.1. Mainly, the channel length is below 1 cm instead of 5 - 7 cm. This results in higher accelerating required voltages and in lower operating oxygen pressures.
Most difficulties had concerned the choice of the contact material for the heater power supply and its mechanical fixing. After many attempt we opted for using silver wires which connect the power supply wires to the heater. Also the nuts that fixing the Ag wires are made of Ag. We made this coice to avoid unwonted contamination and because of the rather high Ag melting point (> 900°C).
Another critical aspect is represented by the relative position of the gas inlet and the channel for the vacuum system. Than, it must be taken into account that a change in the gas inlet position will may affect the deposition conditions.
We used the described apparatus to produce a first set, which we call set 1, of thin NGO films at different substrate temperatures. For each temperature we performed the deposition on both STO:0.05 at%Nb (110) and STO:0.2 at%Nb (100).
All the depositions has been performed at a pressure of $9 \cdot 10^{-3}$ mbar, and at a frequency of 3 Hz for the duration of 15 minutes. Different films were grown in the substrate temperature range from 650°C to 790°C.
The XPS spectrum of a sample is shown in figure 4.23. Table 4.2 shows the atomic quantification for the same sample. In addition to the expected Nd, Ga, and O, also the Sr and Ti spectra, arising from the substrate, are present. Unfortunately, a boron contamination is evident.
XRD investigations confirm the presence of boron oxide in the sample. XRD characterization was performed by Prof. Georg Schmidt from the Halle University, Germany, with a Siemens / Bruker D5000 System. The XRD peaks of a film grown at similar temperature than that of figure 4.23 are shown in figure 4.24. This pattern indicates the possible presence of boron oxide, with a lattice parameter of about 4.3 Å, and the absence of an ordered NGO structure. Indeed, the lattice constant of STO and pseudocubic NGO are 3.905 Å and 3.861 Å, respectively. Than, the NGO peak should be

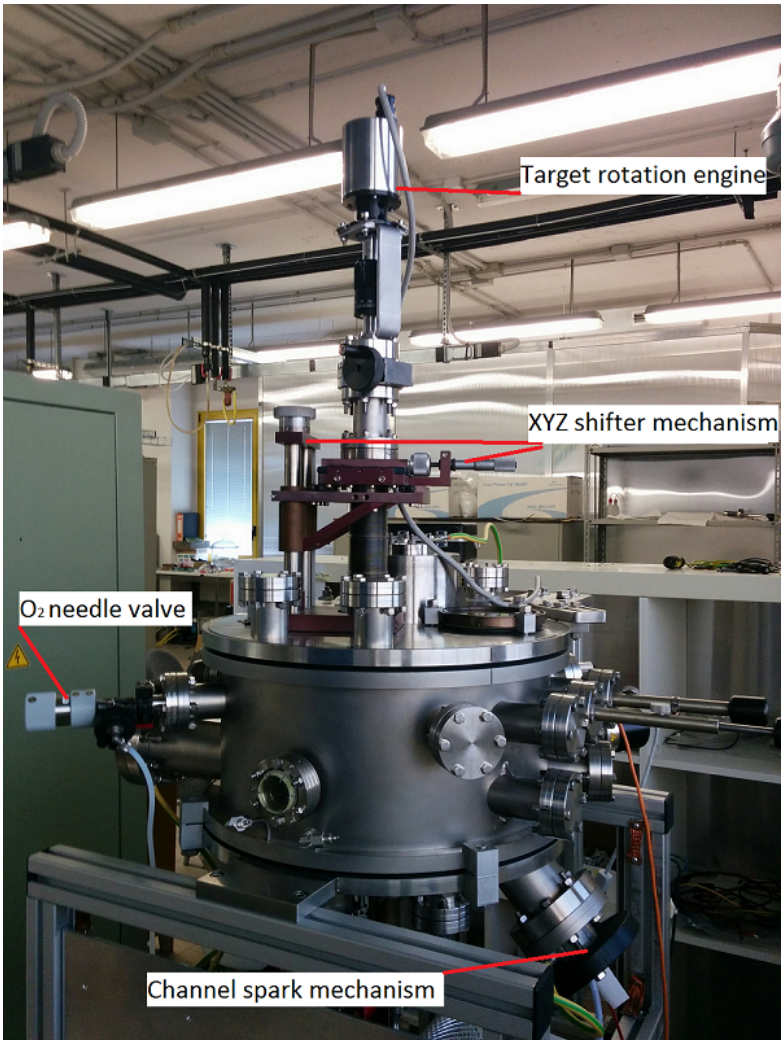

Figure 4.21: CSA system used for the fabrication of the first set of Au/NGO/Nb:STO capacitors.

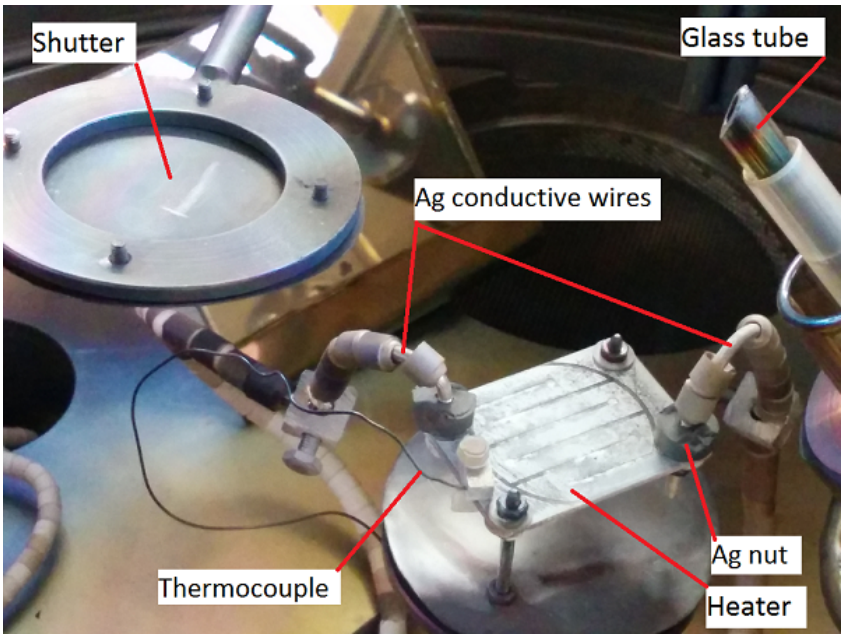

Figure 4.22: A detail of the CSA configuration and of the heater electrical connections.

arised at higher angles.

Boron contamination completely disappears when depositions are made at room temperature. Further investigations has revealed that the B contamination comes from the caramic heater: a single crystal quartz subjected to the heating cycle without deposition, was affected by the same boron contamination of the samples.
Moreover, at room temperature deposition a fluorine contamination appears. On our hypothesis, F contamination arisis from the glass tube or teflon centering ring and disappears at high temperature because of possible F re-evaporation.

4.3.2 NGO on Nb:STO Growth - Set 2

A second set of NGO films, which we will call set 2, has been fabricated by means of the usual CSA system described in section 3.1 and previously used also for the growth of the STO films. Three deposition temperatures has been investigated, 650, 700 and 750° C with the following conditions: $p = 1.56 \cdot 10^{-2}$ mbar, an accelerating voltage of 13 kV and a beam frequency of 1.5 Hz, resulting in a growth rate of about 1 nm/min. The grown films had a thickness of about 25 nm.
Three films, one for each temperature, were grown on STO:0.7 wt%Nb (100) and two films, deposited at 650 and 700°C, were grown on STO:0.05 at%Nb (110). At the end of the deposition the samples were quenched in O_2 atmosphere, keeping the same pressure

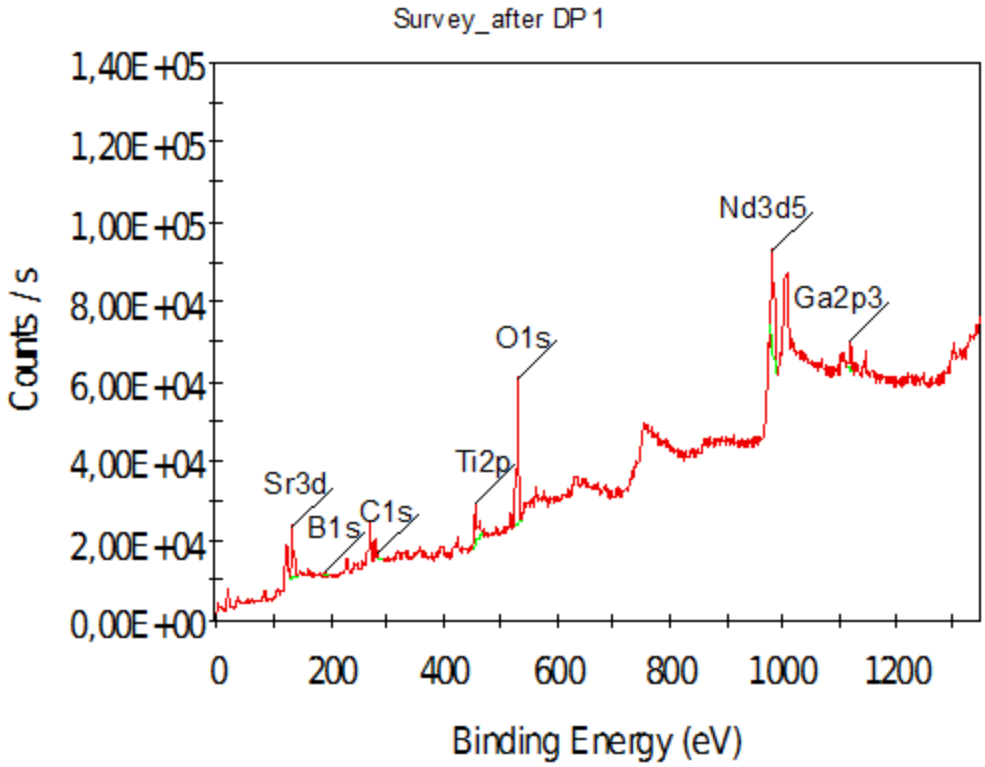

Figure 4.23: XPS spectrum for an NGO/Nb:STO (100) device grown at 760°C (set 1).

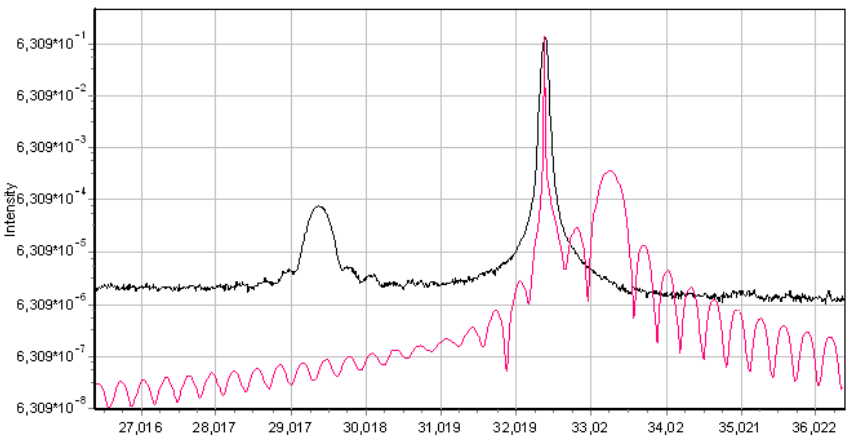

Figure 4.24: 110 XRD reflection for an NGO/Nb:STO sample. The sharp peak at about 32.357° degrees is associated to the STO substrate. The peak at a lower angle (29.359°) can be associated to the boron oxide B_2O_3.

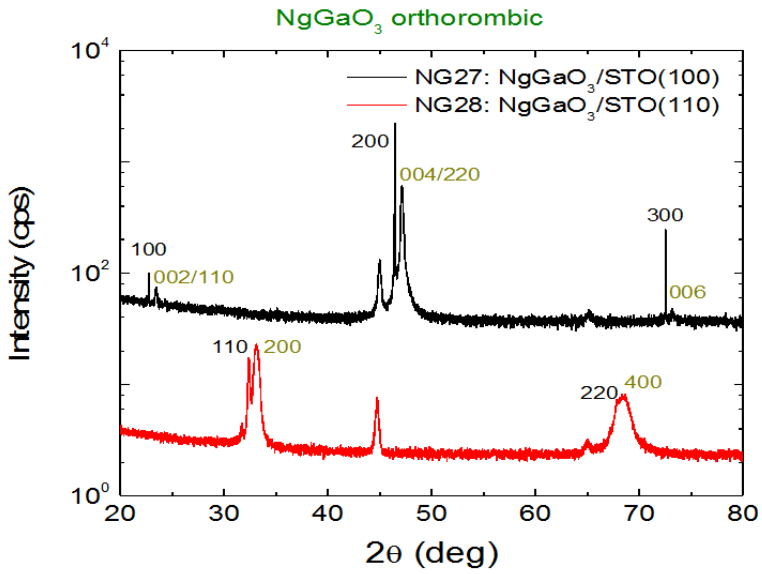

Figure 4.25: XRD reflection for NGO films grown on (100) and (110) substrates. The film orientation is written in dark yellow. On (110) substrate the film is, as expected, (100) oriented. As said before, there exist two matching orientation on (100) substrate. Unfortunately this measure can determine which orientation is present.

of the deposition.
Also in this case the top electrode consisted in a circular Au contact with a 2 mm diameter and a small quantity of In was spread on the bottom electrode in order to achieve an ohmic contact.
The XRD pattern for of two samples reported in figure 4.25 confirms the crystallinity and epitaxial growth of the NGO films on both (100) and (110) Nb:STO substrates. The XRD characterization was performed by Dr. Fabiola Liscio, CNR - IMM Bologna, with a Smartlab Rigaku system. Figure 4.26 shows a survey of the XPS data. Boron contamination is absent, but a contamination from fluorine and silicon appears. Such a contamination amounts at about the 10% molar, neverthess the XRD show that the film is epitaxial with the crystal structure of the NGO.
This means that, on the contrary of set 1, where the boron contamination prevented the epitaxy, suggesting that B is a true part of the film, here the Si and F contamination does not impede the epitaxial growth, suggesting that F and Si segregates and are not mixed with the NGO: we guess to have epitaxial NGO film plus Si anf F inclusions that do not disturb the epitaxy neither the dielectricity.
Since LSMO films do not have these contaminations, the pressure value and the voltage discharge can be likely used to eliminate the contamination. Such optimization should lead to even lower leakage current values, while the dielectric contsant is already com-

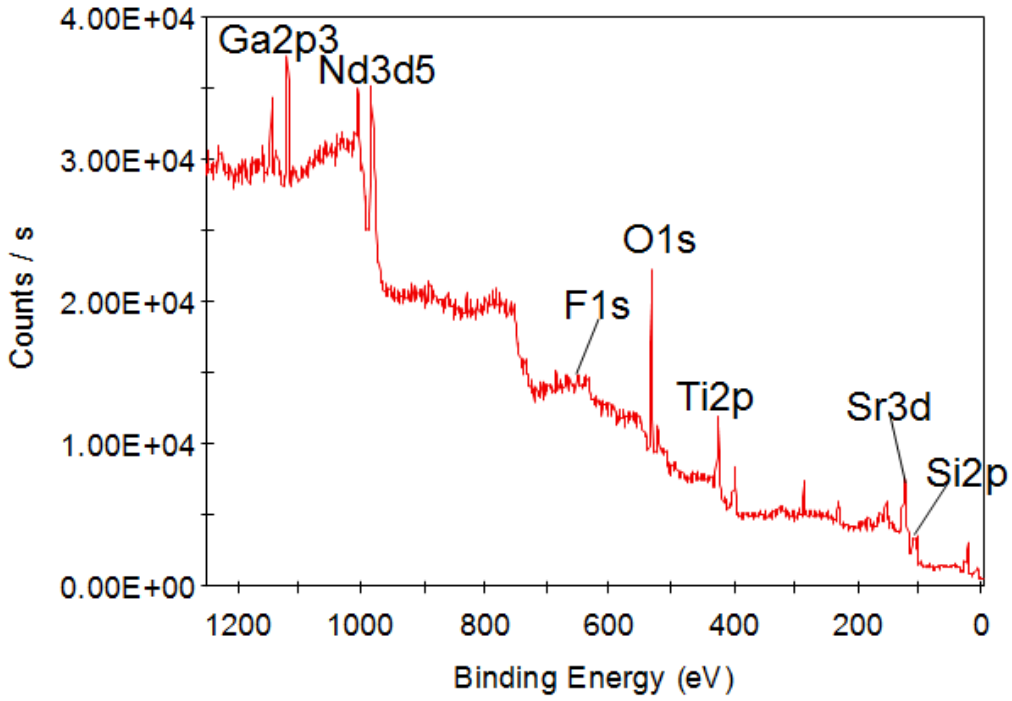

Figure 4.26: XPS spectrum for an NGO/Nb:STO (100) device grown at 760°C (set 1).

parable to the bulk one.

4.3.3 Electrical Characterization - Set 2

The impedance measurements on the set 2 of Au/NGO/Nb:STO has been performed in the frequency range from 20 Hz to 2 MHz with 0.01 V signal.
Figure 4.10 shows the room temperature behaviour of the impedance modulus and phase for a device grown on Nb:STO (100) at 650°C. The impedance behaviour of the other sample is very similar. Owing to the purely capacitive behaviour of the device we can determine its capacitance via the usual formula $C = 1/\omega|Z|$. The I(V) measurements for the films grown on (100) and (110) substrates are reported in figure 4.28. As happened for the STO capacitors, also these I(V) curves are not symmetric. On (100) the asymmetry results more pronounced.
The main features of the samples are reported in table 4.3. Figure 4.29 shows the behaviour of the dielectric constant as a function of the growth temperature. As we can see it is maximum for the films grown at 700°C and, for fixed growth temperature, it is larger in the case of films grown on the (100) oriented substrates. However, the axis

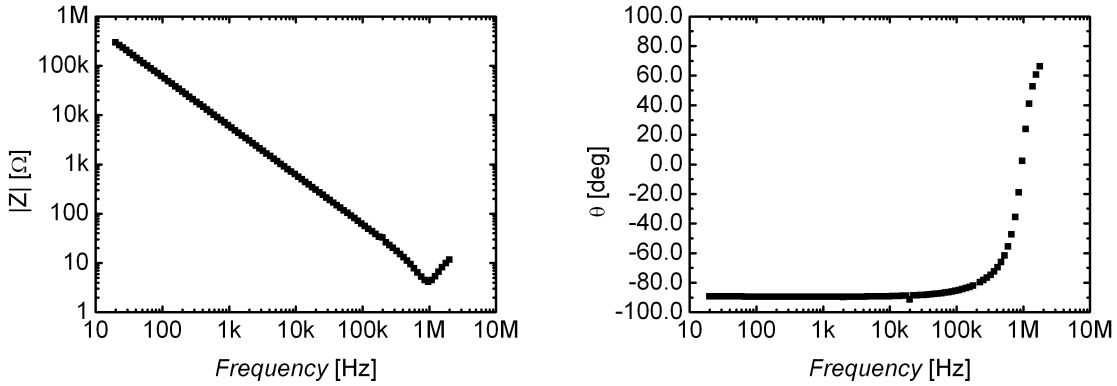

Figure 4.27: Impedance modulus (left) and phase (right) as a function of frequency for an Au/NGO/Nb:STO (100) capacitor grown at 650°C, measured at 295 K.

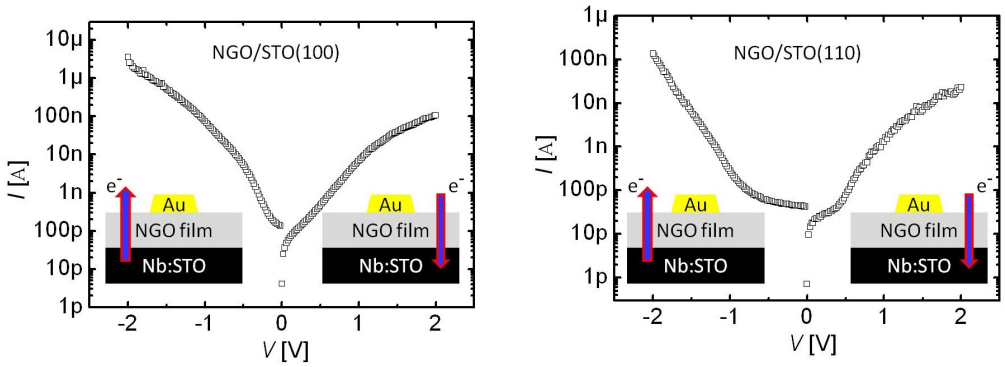

Figure 4.28: I(V) curves for Au/NGO/NB:STO capacitors with the NGO film epitaxially grown on (100) (left) and (110) Nb doped STO (right).

Growth temperature (°C)	650		700		750
Substrate orientation	(100)	(110)	(100)	(110)	(100)
Thickness (nm)	25 ± 2	28 ± 2	25 ± 2	25 ± 2	25 ± 2
Resistance (MΩ)	250	4000	0.14	0.34	1000
Capacitance (nF)	26	19	28	26	24
C per unit area (fF/μm^2)	8.3 ± 0.8	6.0 ± 0.6	8.9 ± 0.9	8.3 ± 0.8	7.6 ± 0.8
Permittivity ϵ_r	24 ± 4	19 ± 3	26 ± 4	25 ± 4	20 ± 3
Breakdown voltage (MV/cm)	1.2	3.1	0.8	0.8	4
Leakage curr. at 1 V (A/cm^2)	$3.5 \cdot 10^{-5}$	$4.7 \cdot 10^{-6}$	$2.0 \cdot 10^{-3}$	$8.9 \cdot 10^{-3}$	$2.3 \cdot 10^{-6}$

Table 4.3: Main characteristics of the Au/NGO/Nb:STO capacitors. The values of capacitance and relative permittivity are measured at room temperature. Since the I(V) curves are not symmetric, for each device only the highest value of leakage current is reported.

orientation is not the only difference between the two kind of used substrates, also the Nb concentration is not the same.
The calculated values of the NGO dielectric constant are very similar to the values reported in literature ($\epsilon_r \sim 22$ at room temperature [42]). In this case we haven't performed low temperature measurements, since any relevant change in NGO dielectrc properties is expected, only a sligth decrease has been observed in [42].

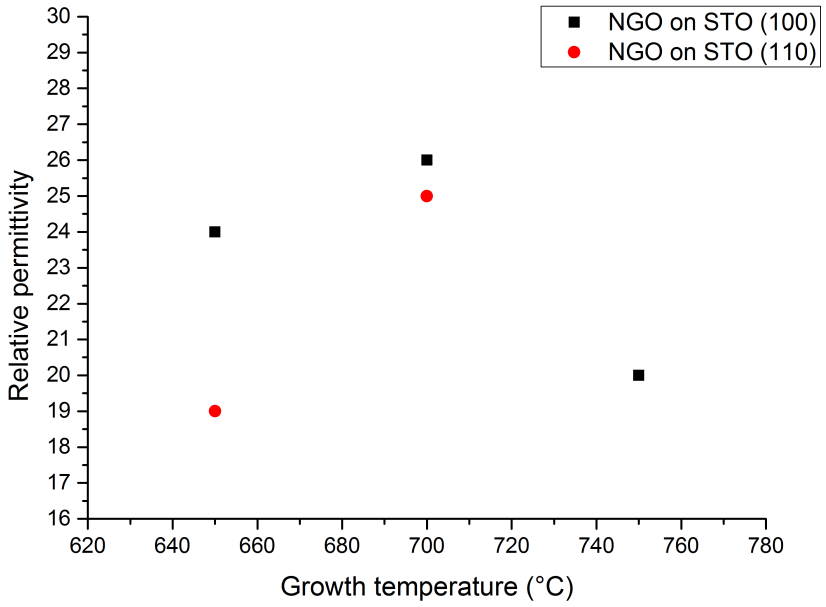

Figure 4.29: Relative permittivity versus NGO deposition temperature for Au/NGO/Nb:STO capacitors with (100) and (110) oriented Nb doped STO substrates. The permittivity is calculated with the usual formula $\epsilon_r = Ct/\epsilon_0 A$.

Conclusions

During this thesis epitaxial thin films of LSMO, STO, NGO and LSMO/STO bilayers have been deposited at the hosting laboratory, with a spintronics oriented approach. LSMO works as electrode and STO as spacer between LSMO and Co electrodes. STO and NGO epitaxial thin films deposited on conductive Nb doped STO substrates play a double role in potential spintronic devices: they act as high-κ gate insulators for MOSFET with spin polarized source and drain and at the same time are a matching substrate for the deposition of LSMO on top of them (bottom gate MOSFET geometry).
The deposition of LSMO epitaxial thin films by CSA were an already achieved result in the hosting laboratory while the capability to deposit epitaxial STO and NGO thin films is a result of this thesis. In addition to the film deposition, in the hosting laboratory we also performed the dielectric characterization (impedance spectroscopy).
LSMO/STO/Co junctions with epitaxial and amorphous STO barriers were fabricated with the purpose to study the feasibility of fully inorganic Magnetically Enhanced Memristor (MEM) with a cross-bar geometry, up to now demonstrated only in organic devices. The degree of crystalline order was controlled by means of the substrate temperature during the growth. TEM analysis demonstrated that the interface are clearly defined and confirmed both the epitaxy of the epitaxial STO barrier and the absence of crystal order in the amorphous ones. EELS measurements have shown that the epitaxial barrier are stoichiometric while the amorphous STO layers are Sr deficient. Both the barriers properly work as spacer layer but originate different properties. Junctions with an epitaxial STO barrier have shown a behavior typical for magnetic tunnel junctions, with the usual temperature dependence of the magnetoresistance percentage and absence of electric bistability. On the contrary the devices with the amorphous STO barrier were characterized by electric bistability and, after a proper electroforming, a very high magnetoresistance ratio. Nevertheless, the interrelationship between the resistive state and the magnetoresistance was not clearly confirmed. The main result is that the employment of not ordered oxide barrier is a promising route towards fully inorganic MEM.
Epitaxial high-κ STO and NGO thin films were deposited by CSA. TEM characterization demonstrated the epitaxy of the STO layers even when they are deposited on LSMO thin films. The epitaxial quality of the NGO thin films was confirmed by XRD measurements. In the hosting laboratory we performed the dielectric characterization of

the samples.
We compared the dielectric properties of the STO thin films with the best state-of-the-art case. The STO thin films ($\sim$ 30 nm) featured competitive leakage current values while the capacitance density and the dielectric constant values were low, especially the huge increase of ϵ_r by decreasing temperature, typical for STO single crystals, was not achieved. It was necessary to overcome a critical thickness, located between 50 and 150 nm, to achieve behavior of STO single crystal. For a 170 nm STO film we achieved $\epsilon_r = 175$ at room temperature and $\epsilon_r = 250$ at 100 K. The less performing behavior of thinner films can be ascribed to a general tendency of the STO to form oxygen vacancies or to crystalline defects that require a bigger amount of materials to reach bulk properties. However, it is a well-established result that STO thin films tend to have worse dielectric properties than single crystals. Further work is required to bring the best values to thinner films. Deposition rate, oxygen pressure during the film deposition and post-deposition annealing are the main parameters to investigate.
Epitaxial NGO thin films ($\sim$ 25 nm) with the same ϵ_r value as NGO single crystal ($\sim$ 20) are obtained. We achieve very competitive leakage current values, comparable to the ones of the best STO literature data, while the literature data about the dielectric properties of NGO thin films is almost absent. The capacitance per unit area is lower than the one in the STO case because of the lower ϵ_r value, which is however of the same value of the single crystal. The relative easiness in depositing NGO thin films with properties similar to the single crystal case is possibly due to the NGO chemical stability. It is known that NGO does not have a great tendency to form oxygen vacancies and is generally a less defective material than STO. Considering that $\epsilon_r \sim 20$ is anyway a very good value, it appears that NGO is a really promising and suitable material for high-κ applications.

Bibliography

[1] S.A. Wolf, D.D. Awschalom, R.A. Buhrman, J.M. Daughton, S. von Molnár, M.L. Roukes, A.Y. Chtchelkanova, D.M. Treger, *Spintronics: A Spin-Based Electronics Vision for the Future*, MAGNETISM AND MATERIALS, Vol. **294**, 1488 (2001).

[2] N.F. Mott, *The Electrical Conductivity of Transition Metal*, Proc. R. Soc. London, Ser. A, **153**, 699 (1936).

[3] T. Shinjo, *Nanomagnetism and Spintronics*, Elsevier ed., (2009).

[4] A. Fert and I.A. Campbell, *TWO-CURRENT CONDUCTION IN NICKEL*, Phys. Rev. Lett. **21**, 1190 (1968).

[5] A. Fert and I.A. Campbell, *TRANSPORT PROPERTIES OF FERROMAGNETIC TRANSITION METALS*, J. Phys. Colloques **32**, C1-46 (1971).

[6] A. Fert and I.A. Campbell, *Electrical resistivity of ferromagnetic nickel and iron based allois*, J. Phys. F:Met. Phys. **6**, 849 (1976).

[7] G. Binasch, P. Grünberg, F. Saurenbach and W. Zinn, *Enhanced magnetoresistance in layered magnetic structure with antiferromagnetic interlayer exchange*, Phis. Rev. B, **39**, 4828 (1988).

[8] M.N. Baibich, J.M. Broto, A. Fert, F. Nguyen van Dau, F. Petroff, P. Eitenne, G. Creuzet, A. Friederich and J. Chazelas, *Giant Magnetoresistance of (001)Fe/(001)Cr Magnetic Superlattice*, Phis. Rev. Lett. **61**, 2472 (1988).

[9] *The Discovery of Giant Magnetoresistance*, The Royal Swedish Academy of Sciences, Scientific Background on the Nobel Prize in Physics 2007, (2007).

[10] B. Dieny, V.S. Speriosu, S.S.P. Parkin, B.A. Gurney, D.R. Wilhoit and D. Mauri, *Giant magnetoresistive in soft ferromagnetic multilayers*, Phys. Rev. B **43**, 1297 (1991).

[11] C.Chappert, A. Fert and F.N. van Dau *The emergence of spintronics in data storage*, Nature Materials **6**, 813 (2007).

[12] A. Fert, *Nobel Lecture: Origin, development, and future of spintronics*, REVIEWS OF MODERN PHYSICS, Vol. **80**, 1517 (2008).

[13] T. Valet and A. Fert, *Theory of the perpendicular magnetoresistance in magnetic multilayers*, Phys. Rev. B **48**, 7099 (1993).

[14] M. Jullierè, *Tunneling between ferromagnetic films*, Phys. Lett. A **54**, 225 (1975).

[15] J.S. Moodera, L.R. Kinder, T.M. Wong and R. Meservey, *Large Magnetoresistance at Room Temperature in Ferromagnetic Thin Film Tunnel Junctions*, Phys. Rev. Lett. **74**, 3273 (1995).

[16] T. Miyazaki and N. Tezuka, *Giant magnetic tunneling effect in* $Fe/Al_2O_3/Fe$ *junction*, J. Magn. Magn. Mater. **139**, 231 (1995).

[17] T. Miyazaki and N. Tezuka, *Spin polarized tunneling in ferromagnet/insulator/ferromagnet junctions*, J. Magn. Magn. Mater. **151**, 403 (1995).

[18] J.M. De Teresa, A. Barthélémy, A. Fert, J.P. Contour, R. Lyonnet, F. Montagne, P. Seneor and A. Vaurès, *Inverse Tunnel Magnetoresistance in* $Co/SrTiO_3/La_{0.7}Sr_{0.3}MnO_3$*: New Ideas on Spin Polarized Tunneling*, Phys. Rev. Lett. **82**, 4288 (1999).

[19] X.G. Zhang and W.H. Butler, *Large magnetoresistance in bcc Co/MgO/Co and FeCo/MgO/FeCo tunneling junctions*, Phys. Rev. B **70**, 172407 (2004).

[20] W.H. Butler, X.G. Zhang, S Vutukuri, M. Chshiev and T.C. Schulthess, *Theory of Tunneling Magnetoresistance for Epitaxial Systems*, IEEE TRANSACTIONS ON MAGNETICS **41**, 2645 (2005).

[21] S.S.P. Parkin *et al.*, *Giant tunnelling magnetoresistance at room temperature with MgO (100) tunnel barriers*, Nature Materials **3**, 862 (2004).

[22] S. Yuasa, T. Nagahama, A. Fukushima, Y. Suzuki and K. Ando, *Giant room-temperature magnetoresistance in single-crystal Fe/MgO/Fe magnetic tunnel junctions*, Nature Materials **3**, 868 (2004).

[23] J.C. Slonczewski, *Current-driven excitation of magnetic multilayers*, J. Magn. Magn. Mater. **159**, L1-7 (1996).

[24] L. Berger, *Emission of spin waves by a magnetic multilayer traversed by a current*, Phys. Rev. B **54**, 9353 (1996).

[25] J. Katine, F. Albert, R. Buhrman, E. Myers and D. Ralph, emphCurrent-driven magnetization reversal and spin-wave excitations in Co/Cu/Co pillars, Phys. Rev. Lett. **84**, 3149 (2000).

[26] A.V. Khvalkovskiy *et. al*, *Basic principles of STT-MRAM cell operation in memory arrays*, J. Phys. D: Appl. Phys. **46**, 074001 (2013).

[27] P.S. Dash, S. Sandeep, R.S. Patel, M.P. de Jong and R. Jansen, *Electrical creation of spin polarization in silicon at room temperature*, Nature 462, 491 (2009).

[28] L.E. Hueso *et al.*, *Transformation of spin information into large electrical signals using carbon nanotubes*, Nature **445**, 410 (2007).

[29] L.O. Chua, *Memristor - The Missing Circuit Element*, IEE TRANSACTIONS ON CIRCUIT THEORY **18**, 507 (1971).

[30] R.S. Williams, *How We Found the Missing Memristor*, Memristors and Memristive Systems, Ronald Tetzlaff Editor, Springer (2014).

[31] H. Jang, O.A. Kirillov, O.D. Jurchescu and C.A. Richter, emphSpin transport in memristive devices, Appl. Phys. Lett. **100**, 043510 (2012).

[32] M. Prezioso, A. Riminucci, I. Bergenti, P. Graziosi, D. Brunel and V.A. Dediu, *Electrically Programmable Magnetoresistance in Multifunctional Organic-Based Spin Valve Devices*, Adv. Mater. **23**, 1371 (2011).

[33] M.A. Peña, J.L.G. Fierro, *Chemical Structures and Performance of Perovskite Oxides*, Chem. Rev. **101**, 1981-2017 (2001).

[34] A.S. Bhalla, R. Guo, R. Roy, *The provskite structure - a review of its role in ceramic science and technology*, Mat. Res. Innovat **4** (2000).

[35] V.M. Goldschmidt, Skr. Nor. Viedenk.-Akad., Kl. Part I. Mater.-Naturvidensk. Kl, no. 8 (1926).

[36] A.M. Haghiri-Gosnet, P.J. Renard, *CMR Manganites: physics, thin films and devices*, J. Phys. D: Appl. **36**, R127-R150 (2003).

[37] J.B. Goodenought, *RARE EARTH - MANGANESE PEROVSKITES*, Handbook on the Physics and Chemistry of Rare Earths, vol. **33**, chapter 214 (2003).

[38] R. Zurmühlen et al., *Dielectric spectroscopy of* $Ba(B'_{1/2}B''_{1/2})O_3$ *complex perovskite ceramics: Correlation between ionic parameters and microwave dielectric properties. I. Infrared reflectivity study (*$10^{12} - 10^{14}$ *Hz)* J. Appl. Phys. **77**, 5341 (1995).

[39] R. Zurmühlen et al., *Dielectric spectroscopy of* $Ba(B'_{1/2}B''_{1/2})O_3$ *complex perovskite ceramics: Correlation between ionic parameters and microwave dielectric properties. II. Studies below the phonon eigenfrequencies (*$10^2 - 10^{12}$ *Hz)* J. Appl. Phys. **77**, 5351 (1995).

[40] G.D. Wilk, R.M. Wallace ane J.M. Anthony, *High-k gate dielectrics: Current status and materials properties considerations*, J. Appl. Phys. **89**, 5243 (2001).

[41] R. Laibowitz, J. Lian *Method to produce low leakage high k materials in thin film form*, http://www.google.com/patents/WO2004057657A1?cl=en (2004).

[42] J. Krupka, R.G. Geyer, M. Kuhn and J.H. Hinken, *Dielectric Properties of Single Crystals of Al_2O_3, $LaAlO_3$, $NdGaO_3$, $SrTiO_3$, and MgO at Cryogenic Temperatures*, IEE TRANSACTIONS ON MICROWAVE THEORY AND TECHNIQUES **42**, 1886 (1994).

[43] S. Pradhan, G.S. Roy, *Study The Crystal Structure and Phase Transition of $BaTiO_3$ - A Perovskite*, Reserarcher. 2013;**5**(3): 63-67.

[44] Y. Su, G.J. Weng, *A self-consistent polycrystal model for the spontaneous polarization of ferroelectric ceramics*, Proc. R. Soc. A (2006) **462**, 1763-1789.

[45] D. Fu, M. Itoh, *Role of Ca off-centering in tuning ferroelectric phase transitions in $Ba(Zr,Ti)O_3$ system*, Ferroelectric Materials - Synthesis and Characterization, Chapter 5, Aime Pelaiz Barranco ed. (2015).

[46] D. Fu, M. Itoh, S. Koshihara, T. Kosugi and S. Tsuneyuki, *Anomalous Phase diagram of Ferroelectric (Ba, Ca)TiO_3 Single Crystals with Giant Electromechanical Response*, Phys. Rev. Lett. **100**, 227601 (2008).

[47] D. Fu, Y. Kamai, N. Sakamoto, N. Wakiya, H. Suzuki and M. Itoh, *Phase diagram and piezoelectric response of $(Ba_{1-x}Ca_x)(Zr_{0.1}Ti_{0.9})O_3$ solid solution*, J. Phys. Cond. Matter., vol. **25**, n. 42, p. 425901 (2013).

[48] R.C. Kell and N.J. , *Structural transitions in barium titanate-zirconate transducer materials*, Acta Acustica united with Acustica. 1956; **6**: 235.

[49] A. Outzourit, J.U. Trefny, T. Kito, B. Yarar, A. Naziripour and A.M. Hermann, *Fabrication and characterization of $Ba_{1-x}Sr_xTiO_3$ tunable thin film capacitors*, Thin Solid Films, **259**, 218-224 (1995).

[50] R. Loetzsch, A. Lübcke, I. Uschmann, E. Förster, V. Groβe, M. Thuerk, T. Koetting, F. Schmidl and P. Seidel, *The cubic to tetragonal phase transition in $SrTiO_3$ single crystals near its surface under internal and external strains*, Appl. Phys. Lett. **96**, 071901 (2010).

[51] A. Bussmann-Holder , A. R. Bishop and A. Simon (2010) *$SrTiO_3$: From Quantum Paraelectric to Superconducting*, Ferroelectrics, 400:1, 19-26, DOI: 10.1080/00150193.2010.505528 .

[52] K.A. Müller and H. Burkard, *$SrTiO_3$: An intrinsec quantum paraelectric below $4\,K$*, Phys. Rev. B **19**, 3593 (1978).

[53] K.A. Müller, W. Berlinger and E. Tosatti, *Indication for a novel phase in the quantum paraelectric regime of $SrTiO_3$*, Z. Phys B - Condensed Matter *mathbf*84, 277-283 (1991).

[54] W.J. Burke and R.J. Pressley, *STRESS INDUCED FERROELECTRICITY IN $SrTiO_3$*, Solid State Communications, Vol. **9**, pp. 191-195 (1971).

[55] S. Hyun and K. Char, *Effects of strain on the dielectric properties of tunable dielectric $SrTiO_3$ thin films*, Appl. Phys. Lett. **79**, 254 (2001).

[56] T.M. Shaw, Z. Suo, M. Huang, E. Linger, R.B. Laibowitz and J.D. Baniecki, *The effects of stress on the dielectric properties of barium strontium titanate thin films*, Appl. Phys. Lett. **75**, 2129 (1999).

[57] N.A. Pertsev, A.K. Tagantsev and N. Setter, *Phase transitions and strain-induced ferroelectricity in $SrTiO_3$ epitaxial thin fimls*, Phys. Rev. B **87**, R825 (2000).

[58] T. Schimizu, *THE EFFECT OF STRAIN ON THE PERMITTIVITY OF $SrTiO_3$ FROM FIRST-PRINCIPLE STUDY*, Solid State Communications, Vol. **102**, No. 7, pp. 523-527 (1997.)

[59] J.H. Haeni et al., *Room-temperature ferroelectricity in strained $SrTiO_3$*, Nature, Vol. **430**, 758 (2004).

[60] P. Padmini, T.R. Taylor, M.J. Lefevre, A.S. Nagra, R.A. York and J. Speck, *Realization of high tunability barium strontium titanate thin films by rf magneton sputtering*, Appl. Phys. Lett. **75**, 3186 (1999).

[61] B. Jaffe, W.R. Cook Jr. and H. Jaffe, *PIEZOELECTRIC CERAMICS*, ACADEMIC PRESS LONDON and NEW YORK (1971).

[62] B. H. Park and Q. Jia, *Enhanced Dielec tric Properties of (Ba,Sr)TiO_3 Thin Films Applicable to Tunable Microwave Devices*, Jpn. J. Appl. Phys. Vol. **41** pp. 7222-7225 (2002).

[63] K. Abe and S. Komatsu, *Epitaxial Growth and dielectric Properties of ($Ba_{0.24}Sr_{0.76}$)TiO_3 Thin Film*, J. Appl. Phys. Vol. **33**, pp. 5297-5300 (1994). 5

[64] K. Abe and S. Komatsu, *Ferroelectric properties in epitaxially grown $Ba_xSr_{1-x}\,TiO_3$ thin films*, J. Appl. Phys. **77**, 6461 (1995).

[65] C. Basceri, S.K. Streiffer, A.I. Kingon and R. Waser, *The dielectric response as a function of temperature and film thickness of fiber-textured (Ba,Sr)TiO_3 thin films grown by chemical vapor deposition*, J. Appl. Phys. **82**, 2497 (1997).

[66] A-M Haghiri-Gosnet and PJ-P Renard, *CMR manganites: physics, thin films and devices*. J. Phys. D: Appl. Phys. **36**, R127-R150 (2003).

[67] R. Mahesh, R. Mahendiran, A.K. Raychandhury and C.N.R. Rao, *Effect of particle size on the giant magnetoresistance of* $La_{0.7}Ca_{0.3}MnO_3$, Appl. Phys. Lett. 68, 3555 (1996).

[68] A. Gupta *et. al.*, *Grain-boundary effects on themagnetoresistance properties of perowskite manganite films*, Phys. Rev. B **54**, R15 629 (1996).

[69] P. Graziosi, M. Prezioso, A. Gambardella, C. Kitts, R.K. Rakshit, A. Riminucci, I. Bergenti, F. Borgatti, C. Pernechele, M. Solzi, D. Pullini, D. Busquets-Mataix and V.A. Dediu, *Condition for the growth of smooth* $La_{0.7}Sr_{0.3}MnO_3$ *thin films by pulsed electron beam ablation*, Thin solid films **534**, 83 (2013).

[70] G. Müller and C. Schultheiss, *Deposition by means of Pulsed Electron Beam Ablation*, High-Power Particle Beams, 1994 10th International Conference on (Volume:2), 833 (1994).

[71] J.F. Watts and J. Wolstenholme, *An Introduction to Surface Analysis by XPS and AES*, Wiley (2003).

[72] J. Als-Nielsen and D. MacMorrow *Elements of Modern X-ray Physics*, Wiley, second edition (2011).

[73] M. Prezioso et al., Adv. Mat. **25**, 534 (2013) and patent V. Dediu et al. EP2764514A2.

[74] H. J. Jang et al., Appl. Phys. Lett. **100**, 043510 (2012).

[75] J. J. Yang, D. B. Strukov and D. R. Stewart, Nature Nanotech. **8**, 13 (2013).

[76] D. B. Strukov et al., Nature **453**, 80 (2008).

[77] C. Barraud et al., Nat. Phys. **6**, 615 (2010).

[78] S. Sanvito, Nat. Phys. 6, **562** (2010).

[79] Nili et al., Adv. Funct. Mater. **24**, 6741 (2014).

[80] A. Riminucci et al. Appl. Phys. Lett. **96**, 112505 (2010).

[81] J. J. Yang, D. B. Strukov and D. R. Stewart, Nature Nanotech. **8**, 13 (2013).

[82] L. D. Bozano et al., Appl. Phys. Lett. **84**, 607 (2004).

[83] T. Ohnishi, K. Shibuya, T. Yamamoto and M. Lippmaa, *Defects and transport in complex oxide thin films*, J. Appl. Phys. **103**, 103703 (2008).

[84] H. Tanaka, J. Zhang and T. Kawai, Phys. Rev. Lett. **88**, 027204 (2002).

[85] K.C. Chiang et al., *Very High Density ($44\,fF/\mu m^2$) $SrTiO_3$ MIM Capacitors for RF Applications*, Journal of The Electrochemical Society, **144**, H214-H216 (2007).

[86] K. Morito, T. Suzuki, S. Sekiguchi, H. Okushi and M. Fujimoto, *Electrical Characterization of $SrTiO_3$ Thin Films Grown on Nb-Doped $SrTiO_3$ Single Crystals*, Jpn. J. Appl. Phys. Vol. **39**, 166 (2000).